

NATIONAL CENTRE FOR NUCLEAR RESEARCH

DOCTORAL THESIS

Gravitational dipole and quadrupole radiation from pulsars

Author:
Paritosh VERMA

Supervisor:
Prof. Dr. Hab. Andrzej
KRÓLAK

*A thesis submitted in fulfillment of the requirements
for the degree of Doctor of Philosophy*

in the



August 24, 2022

Declaration of Authorship

I, Paritosh VERMA, declare that this thesis titled, “Gravitational dipole and quadrupole radiation from pulsars” and the work presented in it are my own. I confirm that:

- This work was done wholly or mainly while in candidature for a research degree at the National Centre for Nuclear Research.
- Where any part of this thesis has previously been submitted for a degree or any other qualification at the National Centre for Nuclear Research or any other institution, this has been clearly stated.
- Where I have consulted the published work of others, this is always clearly attributed.
- Where I have quoted from the work of others, the source is always given. With the exception of such quotations, this thesis is entirely my own work.
- I have acknowledged all main sources of help.
- Where the thesis is based on work done by myself jointly with others, I have made clear exactly what was done by others and what I have contributed myself.

Signed:

Date:

NATIONAL CENTRE FOR NUCLEAR RESEARCH

Abstract

Faculty of Physics
Department of Fundamental Research

Doctor of Philosophy

Gravitational dipole and quadrupole radiation from pulsars

by Paritosh VERMA

Abstract in English

This thesis presents dipole and quadrupole gravitational radiation from pulsars. Einstein's general theory of relativity (GR) predicts only two tensor polarization states dominated by the time-varying quadrupole moment. But a generic metric theory of gravity can also possess scalar and vector polarization states. This thesis focuses on Brans-Dicke (BD) theory, which attempts to modify GR by varying gravitational constant G and has three polarization states. First, we acquire polarization states in BD theory by linearizing the field equations and applying gauge conditions. Then, we employ these formulae to derive the response of a laser interferometric detector to the GW signal from a spinning neutron star in BD theory. Next, we obtain a statistic (\mathcal{D} -statistic) established on the maximum likelihood principle to determine the signal in BD theory in the detector's noise. This statistic generalizes the well-known \mathcal{F} -statistic used in the case of GR. Eventually, we perform Monte Carlo simulations in Gaussian noise to test the detectability of the signal and the precision of estimation of its parameters. Our theoretical framework is executed to probe for the scalar and tensor continuous waves in the LIGO-Virgo O2 and O3 data. We comb for continuous GWs from 23 pulsars at once and twice the spin frequencies both in BD theory and GR. No signal is found in the data, but we could impose better constraints on amplitudes.

Chapter 1 consists of some of the sections from the paper *Królak, A and Verma, P. Recent Observations of Gravitational Waves by LIGO and Virgo Detectors, Universe 2021, 7(5), 137*. Chapters 2, 3 and 4 are based on the paper *Verma, P. Probing Gravitational Waves from Pulsars in Brans-Dicke Theory, Universe 2021, 7(7), 235*. Chapter 5 summarizes the result and theory behind the LIGO-Virgo-KAGRA paper *Searches for Gravitational Waves from Known Pulsars at Two Harmonics in the Second and Third LIGO-Virgo Observing Runs, ApJ 2022, 935, 1*. Appendix A of this thesis discusses the decomposition of the moment of inertia in symmetric trace-free (STF) tensors and spherical harmonics, which is the basis for subsection 3.1.1 of chapter 3. Appendix B summarizes the formulae of the well-known χ^2 distribution. Appendix C is about estimating parameters if a signal is detected and shows the calculation of Fisher and Covariance matrices for a monochromatic wave. It also contains the proof of the fact that $2 \times \mathcal{F}$ -statistic is a χ^2 distribution. Finally, appendix D presents the computation of the total power emitted by the scalar wave in BD theory and tensor wave in general relativity and it uses the paper *Verma, P. A swinging rod in Brans-Dicke Theory, Annalen der Physik, andp.202100600*. These formulae of power are then used to calculate the spin-down limits, one of the essential quantities for data analysis.

NATIONAL CENTRE FOR NUCLEAR RESEARCH

Abstract

Faculty of Physics
Department of Fundamental Research

Doctor of Philosophy

Gravitational dipole and quadrupole radiation from pulsars

by Paritosh VERMA

Abstract in polish

Praca ta przedstawia dipolowe i kwadrupolowe promieniowanie grawitacyjne z pulsarów. Ogólna teoria względności Einsteina (OTW) przewiduje tylko dwa stany polaryzacji, które są zdominowane przez zmienny w czasie moment kwadrupolowy. Ale ogólna metryczna teoria grawitacji może również posiadać stany polaryzacji skalarnej i wektorowej. Praca ta koncentruje się głównie na teorii Bransa-Dickego (BD), która próbuje zmodyfikować OTW poprzez zmianę stałej grawitacyjnej G i ma trzy stany polaryzacji. Otrzymujemy stany polaryzacji w teorii BD poprzez linearyzację równań pola i zastosowanie warunków cechowania. Stosujemy te wzory, aby uzyskać odpowiedź laserowego detektora interferometrycznego na sygnał fali grawitacyjnej z rotującej gwiazdy neutronowej w teorii Bransa-Dickego. Otrzymujemy statystykę (\mathcal{D} -statistic) opartą na zasadzie maksymalnego prawdopodobieństwa identyfikacji sygnału w szumie detektora. Ta statystyka uogólnia dobrze znaną statystykę \mathcal{F} używaną w przypadku ogólnej teorii względności Einsteina. Przeprowadzamy symulacje Monte Carlo w szumie gaussowskim w celu przetestowania wykrywalności sygnału i dokładności oszacowania jego parametrów. Zastosowaliśmy nasz teoretyczny model do poszukiwania skalarne i tensorowe promieniowania grawitacyjnego w danych detektorów LIGO i Virgo z kampani obserwacyjnych O2 i O3. Poszukiwaliśmy fal grawitacyjnych z 23 znanych pulsarów o częstościach równych jednokrotnej i dwukrotnej częstości obrotu pulsara. Nie wykryliśmy żadnego sygnału fali grawitacyjnej. Mogliśmy jednak nałożyć nowe ograniczenia na amplitudy tych fal.

Rozdział 1 składa się z części artykułu [Universe 2021, 7\(5\), 137](#). Rozdziały 2, 3 i 4 są oparte na pracy [Universe 2021, 7\(7\), 235](#). Rozdział 5 podsumowuje wyniki i teorię zawartą w artykule [ApJ 2022, 935, 1](#). Dodatek A do tej pracy omawia rozkład momentu bezwładności na symetryczne tensory bezśladowe (STF) i harmoniki sferyczne, który jest podstawą podrozdziału 3.1.1. Dodatek B przedstawia definicję i parametry rozkładu χ^2 . Dodatek C dotyczy szacowania parametrów w przypadku wykrycia sygnału i przedstawia obliczenia macierzy Fishera i macierzy kowariancji dla fali monochromatycznej. Zawiera również dowód na to, że statystyka $2 \times \mathcal{F}$ ma rozkładem χ^2 . Wreszcie, dodatek D przedstawia obliczenia całkowitej mocy emitowanej przez falę skalarną w teorii BD oraz falę tensorową w ogólnej teorii względności na podstawie artykułu [andp.202100600](#). Te wzory mocy są następnie wykorzystywane do obliczania ograniczeń na promieniowanie grawitacyjne z rotujących gwiazd neutronowych.

Acknowledgements

I am highly indebted to my PhD supervisor, Prof. Królak, for offering me a PhD position at such a highly reputed organization. I was always passionate about working on a theoretically inclined project in gravity, and he made my dreams come true. I took a substantial break from studying physics and spent some time in an economics program before starting my doctoral studies. As a result, I was out of touch with many physics concepts. But his valuable guidance and a strong mentorship with patience enabled me to retrieve momentum and accomplish my research projects. It has been a tremendous honour to be a PhD student of Prof. Królak and a graduate of NCBJ.

I cordially thank Prof. Mrówczyński, Prof. Spaliński and Prof. Pollo for their leadership and always helping with bureaucracy quickly despite being very occupied. I also express my gratitude to Pani Dobrowolska and Pani Dembowska, who always assisted with a smiling face. Because of them, I could focus only on physics without worrying about paperwork.

During my PhD studies, I got a precious opportunity to participate in the LIGO-Virgo-Kagra (LVK) collaboration and work with outstanding scientists worldwide. On the other hand, the Polish NCN grant allowed me to travel around the globe and interact with renowned researchers. I am grateful to them because they helped me evolve as an open-minded person and improved my professional skills.

Being highly influenced by Prof. John Nash, I wanted to develop a deep foundation in analytic number theory or combinatorics by entering into the B.Math program at ISI, India, after my high school, but somehow I ended up in an electronics engineering B.Tech program. Due to a lack of interest in machines, I had hard times with laboratory experiments, and my GPA started declining. Just before touching the event horizon of career collapse, Prof. Bernard and Prof. Mookerjea rescued me by offering undergrad internships in astronomy. It was still not close to what I wanted to do but far more mesmerizing (at least for me) than what I was studying. Without their initial help, I could not have considered pursuing a PhD in physics. During the MS astrophysics program, I was captivated by the lectures of Prof. Fafone and Prof. Tavani. Thankfully, they recognized my affection for equations and helped me move forward in theoretical physics from astronomy. After moving to the USA, the lectures of Prof. Hsu, Prof. Wang and Prof. Khanna introduced me to the beauty of physics which I had been combing for a long time. Especially after following the electrodynamics and relativity lectures by Prof. Khanna, I was sure about continuing my PhD in gravity. Finally, when I arrived in Poland, the course by Prof. Małkiewicz on Quantum physics provided a unique dimension to my knowledge. These lectures allowed me to digest the philosophy of quantum physics rather than just solving the equations and eventually made me think about quantum gravity. On the other hand, outstanding courses on gravitational waves and neutron stars by Prof. Bejger and Prof. Haskell widened my vision and assisted me in writing my research articles and thesis. Besides them, Prof. Diaferio, Prof. Ferrara, Prof. Bozza, Dr. Lemson, Dr. Nava and Dr. Atre contributed enormously to building my career, which I can never forget. Working with these professors at distinct points in spacetime has allowed me to admire the non-homogeneity and non-isotropy of the universe at the terrestrial scale. I warmly thank all my mentors for enhancing my skills and personality. My intellectual development could not be possible without them.

After entering an engineering school, when I began renouncing my enthusiasm for academics, my schoolmates Mr Kachawaha (senior batch), Mr Goyal and Mr

Tambe , engineering graduates from IIT Bombay, indirectly inspired me and guided me toward a research career. Getting my initial research internships could be difficult without their guidance. On the other hand, Late Mr D Silva, scientific officer G in DAE, India, played a crucial role in developing my affection for numbers and equations during elementary school. I could not have travelled so far without the initial seeds he sowed. Some hindrances introduced time dilation in my career trajectory, but they could not contract the motivation of a PhD in some analytical field. I could conceive this firm determination because of my karate master Mr Thomas who prepared us to fight until the last breath. This journey would not have been so adventurous without my three schoolmates, Mr Chundawat, Mr Singh and Mr Srivastava. They made every single trip to India marvellous and indelible. I convey my gratitude to my brothers and my wife's family for always being supportive in my journey. I have no words to thank my parents, as wherever I am today, it is because of their love and unconditional sacrifices. This journey could not have even commenced without their blessings. I have made a few perilous and haphazardly decisions in my career, but my wife always supported me. Without her fortitude, optimism and sacrifices with a smiling face, it was almost impossible to end this chapter of my life. I thank them all from the core of my heart.

I am grateful to NCBJ for providing us with an exquisite apartment near a forest where birds of various species visit us daily in our birdhouse on the balcony. It helped me in my spiritual growth (especially during COVID) to conclude my calculations with the chirping of my friends. Finally, I am highly obliged to the nation where I have spent the maximum time after my motherland. Despite having one of the most challenging languages, Poland has presented one of the best pearls of memories and experiences for the necklace of my life. I salute this ravishing country for intensifying the field of my name and wisdom.

Ultimately, I want to thank the scientific council of NCBJ and reviewers for devoting their time to reading my thesis.

Contents

Declaration of Authorship	iii
Abstract	v
Abstract	vii
Acknowledgements	ix
1 An Introduction to Gravitational Waves	1
1.1 Introduction	1
1.2 Gravitational field zones	3
1.3 Gravitational wave sources	3
1.3.1 Binary system	5
1.3.2 Supernovae	7
1.3.3 Spinning Neutron Stars	9
1.3.4 Cosmological gravitational waves from the big bang	11
1.4 Gravitational Wave detectors	13
1.4.1 Current Detectors	13
1.4.2 Future Detectors	16
2 Gravitational Waves Polarizations in Brans-Dicke theory	19
2.1 Introduction	19
2.2 Experimental tests of Brans-Dicke theory	20
2.2.1 Post-Newtonian and Parameterized post-Newtonian formalism	20
2.2.2 Experimental tests of BD theory in the weak-field limit	21
2.2.3 Experimental tests of BD theory in strong-field limit	22
2.2.4 Search for nontensorial gravitational waves	23
2.3 Polarizations	23
3 Neutron Stars in Brans-Dicke Theory	35
3.1 Rotating Neutron Star	35
3.1.1 Multipole moments	35
3.1.2 Gravitational wave signal from a rotating neutron star	36
3.1.3 Response of the interferometric detector to a gravitational-wave signal form a rotating neutron star	39
3.2 Detection statistic and parameter estimation	44
3.2.1 Data analysis method	48
4 Monte Carlo Simulations	51
4.0.1 Monte Carlo simulations	51

5	Analysis of LIGO-Virgo-Kagra data	59
5.1	Introduction	59
5.2	Data	59
5.3	Definitions	59
5.4	Search Methods	60
5.5	Data Analysis Methods	61
5.6	Theoretical models for GW emission	61
5.6.1	Dual Harmonic	61
5.6.2	Single Harmonic	63
5.6.3	Dipole radiation	64
5.7	Results	65
5.8	Summary	67
A	STF tensors and Spherical harmonics	71
A.1	Multipole expansion	71
A.1.1	Spherical-harmonic decomposition	71
A.1.2	Symmetric tracefree tensors	72
A.1.3	The relation between spherical harmonics decomposition and STF tensors	73
A.2	Mountain on a neutron star	74
	Calculation using spherical-harmonic decomposition	74
	Calculation using STF tensors	75
A.2.1	Verifying the relation between spherical harmonics decomposition and STF tensors	75
B	The χ^2 distribution	77
C	Signal detection and parameter estimation	79
C.1	Signal detection and parameter estimation in Gaussian noise	79
C.2	The case of a monochromatic signal in white noise	81
C.3	The Fisher Matrix	84
C.3.1	The case of known angular frequency	84
C.3.2	The case of unknown frequency ω_0	85
C.3.3	The unknown parameters are A_0 , ϕ and ω_0	86
C.4	Statistical properties of the \mathcal{F} -statistic and maximum likelihood estimators	87
C.4.1	Statistical properties of the maximum likelihood estimators	87
C.4.2	Statistical distribution of the \mathcal{F} -statistic	89
D	Power emitted and spin-down limits	95

To My Grandparents

Chapter 1

An Introduction to Gravitational Waves

1.1 Introduction

In 1916, Albert Einstein published his General Theory of Relativity (GR) [1] which describes how the presence of a mass affects spacetime. To understand it pictorially, we can think of spacetime as a fabric that bends whenever an object is placed on it. This assumption is analogous to putting a ball in the centre of a taut sheet. The curve is steeper near the ball and weakens as we move away from the source.

According to GR, gravity is not a force but a consequence of spacetime curvature. Thus, a light object attracted by a heavier one follows the shortest possible path, known as a geodesic, in this curved region. Any non-uniform changing mass distribution produces ripples in this spacetime fabric which propagate away from the source at the speed of light. It means that a variation in the gravitational tidal field of an object takes time to be felt at vast distances. This information cannot propagate spontaneously or at any speed greater than that of light. These freely propagating ripples are known as Gravitational Waves (GWs), and they carry away energy and momentum from the system. Any theory of gravity described in four or more dimensions will give rise to GWs if it respects the special theory of relativity.

It is helpful to visualize GWs by considering an example of water waves. If we drop a stone in a calm lake, it will produce waves in the water that have both transverse and longitudinal components. The transverse waves are present only on the surface because they require elasticity. In the case of GWs, we have only transverse polarizations because the longitudinal components vanish due to gauge conditions, as discussed in the next chapter. In other words, the static gravitational fields have both transverse and longitudinal components, which fall off as $\frac{1}{r^3}$, where r is the distance between source and observer. But, on the other hand, the radiative part is only transverse, and they fall off as $\frac{1}{r}$. So, only transverse polarizations survive at a vast distance in the wave zone. One example of the static longitudinal gravitational field is the tides in oceans caused by the moon. We know that the speed of transverse waves increases with the elasticity in the medium. Therefore, since GWs travel with the fastest speed, we consider the spacetime fabric the stiffest possible medium.

Although GWs travel with the speed of light, they are pretty distinct from electromagnetic (EMWs). GWs are generated by the bulk motion of large masses and possess wavelengths much longer than the dimensions of the source. Thus, they carry information about the overall activities and vibrations of objects. On the other hand, EMWs are usually produced by slight movements of charge pairs within objects and have wavelengths much smaller than the source's dimension. Hence, they exhibit the aggregate properties of microscopic charges at the surfaces of objects.

GWs or EMWs can be produced only by accelerating masses or charges. But a uniformly moving charge in plasma can generate EMWs, but this is not true for GWs. Unlike EMWs, GWs do not get hindered significantly by interstellar medium, dust or plasma in the universe, and hence they provide us information from the core of the source emitting them. The coupling of GWs with matter is given by Newton's gravitational constant G which numerical value is $6.67 \times 10^{-11} N m^2 kg^{-2}$. On the other hand, EMWs couple to a free charge with the strength $\frac{1}{4\pi\epsilon_0}$ whose numerical value is $8.98 \times 10^9 N m^2 C^{-2}$ (ϵ_0 is the permittivity of free space). Comparing these two coupling constants narrates why GWs travel with almost no hindrance in the universe, whereas EMWs go through various absorption and scattering processes.

For some time Einstein himself denied the existence of gravitational waves in full non-linear theory. The first proper theoretical treatment was given by Trautman and Robinson [2, 3].

A generic metric theory of gravity can possess up to six polarization states of gravitational waves [4]; two tensor states, two vector states and two scalar states as shown in Figure 1.1. The tensorial states could be conceived as spin-2 particles, vector polarizations as spin-1 particles, and scalar polarizations as spin-0 particles in the field theory language. In the case of EMWs, the polarizations represent the direction of oscillating electric fields. But in the case of GWs, polarizations represent deformations in the transverse plane that turn circles made up of test masses into ellipses. The two tensor polarizations are transverse to the wave, and they differ from each other by 45 degrees. So it means that if we rotate one polarization by 45 degrees, we get to the second polarization. And a rotation of 180 degrees gets back to the same state. The two vector polarizations (similar to vertical and horizontal in the EMWs) differ by 90 degrees which means that a rotation of 360 degrees takes us to the same polarization. A circle can represent scalar polarization. The tensor and vector polarizations preserve the area of the circle when transformed into an ellipse but this is not the case for scalar polarizations.

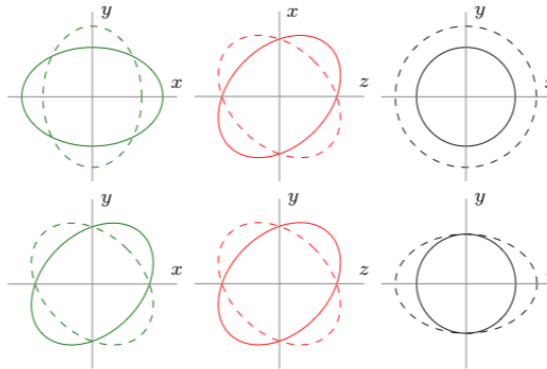


FIGURE 1.1: Effect of different polarizations on a ring of test particles. In all the situations, GW travels in the z -direction. Plus and cross tensor polarizations (black); vector- x (x) and vector- y (y) modes in red; breathing (b) and longitudinal (l) scalar modes (black).

The difference in polarization can also be understood in the language of particle physics. Let ϕ be the minimum angle by which one polarization should be rotated to get the same state. The ϕ_p is given by

$$\phi_p = \frac{2\pi}{S_p} \quad (1.1)$$

where S_p is the spin of the particle. For scalar polarization, $S_p = 0$, for vector polarization, $S_p = 1$ and $S_p = 2$ corresponds to the tensor polarization.

In electrodynamics, the radiation is dominated by the time-varying dipole moment, and monopole radiation is prohibited due to charge conservation. In other words, the first $\frac{1}{r}$ contribution in the radiative field comes from the dipole moment. According to GR, there is no monopole radiation due to the mass conservation and no dipole radiation due to the conservation of linear momentum. The radiation is dominated by the time-varying quadrupole moment, which is the first contribution in the radiative $\frac{1}{r}$ field. But a generic metric theory of gravity also predicts mass monopole and dipole radiation. One such example is Brans-Dicke [5] theory which is the main focus of this thesis.

1.2 Gravitational field zones

Einstein's field equations consist of ten non-linear partial differential equations, making it hard to find the exact solutions to these equations in a general case. So, we divide the spacetime into different regimes according to the strength of tidal fields and then apply the method most suitable to that region.

Consider a source of dimensions L that is emitting GWs. We represent this source by the blue colour in Figure 1.2. We divide the spacetime into four different regions. The first region (1) represents the strong gravity region which requires solving coupled partial differential equations using numerical relativity. In the second region (2), where $r \geq 10L$, one can consider tidal gravitational fields relatively weaker and linearized theory in flat spacetime can be used. The third region (3), where $r \geq \frac{\lambda}{2\pi}$, is the local wave zone (λ is the wavelength of the GW). In this region, one can ignore other sources generating GWs, and the wave under consideration propagates freely. The various calculations in the subsequent chapters of thesis make sense only in the local wave zone. The region beyond the local wave zone is known as the distant wave zone (4), which corresponds to the universe on a large scale. In this region, one requires to consider the effects of gravitational lensing.

1.3 Gravitational wave sources

In principle, any accelerating mass should be able to produce GWs. But due to the feeble strength of these waves, we sought violently astronomical events to detect them. Unfortunately, the GWs generated by earthy mechanical systems or waving hands are too weak to be seen by any current detectors or detectors in the near future.

The most promising candidates for ground-based GW interferometers are the binary systems consisting of black holes (BHs) and neutron stars (NSs). The first detected GW signal [6] originated from the merger of a binary black hole (BBH) system. Binary systems consisting of two stars radiate GWs and as a result of radiation reaction the distance between the components of the binary decreases. This results in a oscillating signal whose amplitude and frequency increases with time and which is called a *chirp*. The two stars eventually merge to form a single object.

A supernova explosion is also a credible source for the emission of GWs. During the lifecycle of a star, the radiation resulting from the nuclear fusion in the interior balances the inward gravitational force. A massive star dies catastrophically when it runs out of its nuclear fuel, and its core undergoes a gravitational collapse, forming possibly an NS or a BH, while the outer layers are blown apart, creating a supernova. An asymmetric collapse causes the time-varying quadrupole moment, which leads

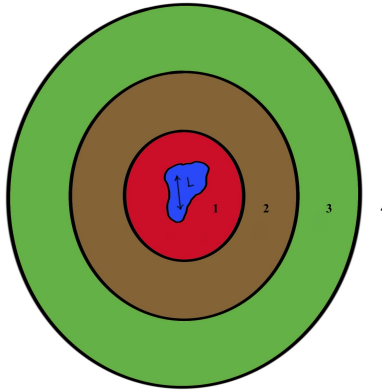


FIGURE 1.2: Different zones of gravitational fields are produced by a source of dimensions L . Zone 1 (red) is the strong gravity zone; region 2 (brown) is the weak field near zone, and region 3 (green) is the local wave zone. The entire universe beyond, region 4, is the distant wave zone.

to the emission of GWs in the form of a burst. The waveform of the burst radiation is not well understood yet, and it is still a topic of research.

Another source of GW is the mountain on the crust of a rotating NS. This mountain can be as high as a few cm, induces deformation in the star, and produces a time-varying mass quadrupole moment. This deviation from the symmetry is responsible for almost a pure sinusoid GW signal with the frequency proportional to the star's spin frequency in the source frame. This signal from an isolated NS is weaker than that originated from the binary merger, but its long-lasting nature may lead to detection with future detectors. A continuous GW from an NS will shed light on the exotic nuclear physics in the star's core and impose a constraint on the equation of state. Despite the absence of any continuous GW, there is a spin-down limit for Crab, Vela, and several other pulsars limiting the loss of pulsars rotational kinetic energy due to the emission of GWs to a small fraction.

Finally, we discuss the stochastic GWs resulting from various physical processes that are inherently stochastic or due to the interference of different coherent signals that are too weak to be resolved individually. For example, the inflation phase of accelerated expansion in the early universe at an approximately constant Hubble rate produces stochastic GWs with quantum mechanical origin. Besides inflation, several phase transitions in the early cosmos, oscillatory motion of cosmic defects such as cosmic strings may contribute to such signals.

The future of GW astronomy is bright because they have the potential to surprise us by exploring entirely new objects and phenomena. In the following subsections, we shall briefly discuss the physics of these sources.

1.3.1 Binary system

For most of the evolution of the binary systems, we can treat both the companions as point sources, and much of their dynamics can be described by quadrupole formula equations.

The evolution of the orbit of the binary system during the inspiral phase is shown in Figure 1.3, and the variation in frequency and amplitude of GW signal is shown in Figure 1.4.

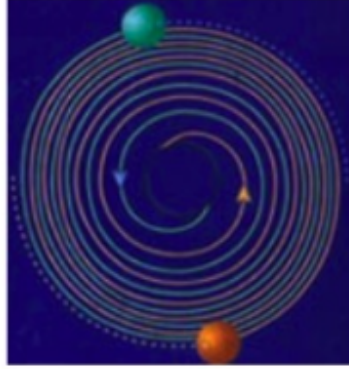


FIGURE 1.3: Orbit of two point like masses in inspiral phase.

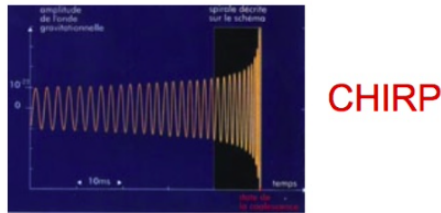


FIGURE 1.4: Schematic diagram showing the final stage of inspiral phase.

There are some crucial parameters needed to understand the physics of a binary system. These parameters are chirp mass \mathcal{M} , total mass M , mass ratio q , effective inspiral spin parameter χ_{eff} , effective precession spin parameter χ_P , dimensionless tidal deformability parameter $\tilde{\Lambda}$. The more massive object in the binary system is called the primary component and its mass is taken to be m_1 whereas, the mass of the lighter or secondary object is denoted by m_2 . The total mass M and the mass ratio q are defined as

$$M = m_1 + m_2, \quad q = \frac{m_2}{m_1}. \quad (1.2)$$

The mass ratio q measures asymmetry in the system with a range $(0, 1]$ where a value closer to 0 implies an asymmetric configuration.

There is a combination of individual masses known as chirp mass defined to be

$$\mathcal{M} = \frac{(m_1 m_2)^{3/5}}{(m_1 + m_2)^{1/5}}. \quad (1.3)$$

The significance of the chirp mass is that in the quadrupole approximation, it determines both the amplitude and the phase modulation of the GW signal from a binary system, and it is generally better constrained than the individual masses of the binary.

The objects in the binary system may also possess individual spins. These spins are encoded in the waveform and the knowledge about individual components bears vital information regarding the evolution of the binary system. The effective inspi-ral spin parameter χ_{eff} contains information about the spin components that are perpendicular to the orbital plane. On the other hand, if there is a significant projection of the spin in the orbital plane, the orbit will precess and this precession is parametrized by effective precession spin parameter χ_P . The analytical expressions for χ_{eff} is

$$\chi_{eff} = \frac{1}{M} \left(\frac{\vec{S}_1}{m_1} + \frac{\vec{S}_2}{m_2} \right) \cdot \frac{\vec{L}}{|\vec{L}|} \quad (1.4)$$

where \vec{S}_1 and \vec{S}_2 are the spins of the primary and secondary components respectively and \vec{L} is the Newtonian orbital angular momentum. The expression for χ_P is given by

$$\chi_P = \max \left\{ \frac{|\vec{S}_{1\perp}|}{m_1^2}, \kappa \frac{|\vec{S}_{2\perp}|}{m_2^2} \right\} \quad (1.5)$$

where $\vec{S}_{i\perp} = \vec{S}_i - (\vec{S}_i \cdot \vec{L}) \frac{\vec{L}}{|\vec{L}|^2}$ and $\kappa = q \frac{(4q+3)}{4+3q}$

An important effect that can be helpful to differentiate between a BH and NS is the tidal deformation in an object. The external field created by the primary object induces a quadrupole deformation in its companion object. This deformation is measured in terms of tidal deformability (λ) and in the lowest order approximation, it is given by

$$\lambda = \frac{2}{3} k_2 R^5 \quad (1.6)$$

where k_2 represents Love number which is dependent on the mass m and the equation of state and R is the radius of the deformed object. It is convenient to introduce a dimensionless tidal deformability parameter Λ defined as

$$\Lambda = G\lambda \left(\frac{Gm}{c^2} \right)^{-5} \quad (1.7)$$

For a binary system, the dominant tidal contribution to the waveform is expressed in terms of the effective dimensionless tidal deformability parameter $\tilde{\Lambda}$ defined as

$$\tilde{\Lambda} = \frac{16}{13} \frac{[(m_1 + 12m_2)m_1^4 \Lambda_1 + (m_2 + 12m_1)m_2^4 \Lambda_2]}{(m_1 + m_2)^5} \quad (1.8)$$

where Λ_i are dimensionless tidal deformability parameters for individual components. Non-spinning BHs have $\Lambda_i = 0$, and the waveform templates use the convention that this is valid for all BHs.

If the initial separation between the two bodies is a_0 , then the system will coalesce after the time t_{coal} given by

$$t_{\text{coal}} = \frac{5}{256} \frac{c^5}{G^3} \frac{a_0^4}{\mu M^4} \quad (1.9)$$

where μ is the reduced mass defined as $\mu \equiv \frac{m_1 m_2}{M}$. The characteristic amplitude of the emitted waves (for a system on a circular orbit) at a distance r from the source is

$$h(r) = \frac{1}{r} \frac{G^{5/3}}{c^4} M^{2/3} \mu \omega^{2/3} \quad (1.10)$$

where ω is the orbital frequency.

These binary systems are considered standard candles because the radiated waveform is well known and allows the determination of cosmological parameters. Availability of the waveform is crucial not only for data analysis issues but also for a different measurement of the Hubble constant. The complete evolution of a binary system and the merging of two companion stars can be represented by the Figure 1.5.

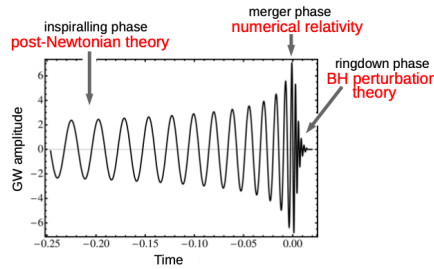


FIGURE 1.5: Pictorial representation for the evolution of binary system.

The inspiral phase can be well approximated with the Post-Newtonian theory. There is a significant increase in the signal's frequency and amplitude, and one needs numerical relativity to model it. The merger involves general relativistic nonlinearities, relativistic hydrodynamics, large magnetic fields, tidal disruption, etc., dictated by unknown physics at nuclear densities. In the ring down phase, the final compact object formed from the coalescence or the collapse oscillates in its quasi-normal modes and emits GW whose frequencies and decay times depend on the nature of the final object: the signal is a superposition of damped sinusoids studied with perturbative methods.

1.3.2 Supernovae

The broad class of stellar collapse possesses a relatively wide variety of astrophysical objects, which might be roughly classified into two distinct categories on the basis of the dynamics of their formation. According to the currently accepted model, Supernovae of type I arise from the gravitational collapse of a white dwarf (WD) in a binary system. The WD accretes matter from the companion until it exceeds the Chandrasekhar mass limit of 1.44 solar masses, undergoing a gravitational collapse. Following the collapse, the star's central core reaches a temperature adequate to initiate the combustion of heavy elements like Carbon, and the energy released in the reaction induces an explosion. In most cases, the explosion destroys the star. On the other hand, Supernovae of type II originate from the gravitational collapse of a massive aged star, leading to a neutron star's formation. The emission of GWs from

a Supernova explosion happens in the phase of gravitational collapse of the star, and the amount of the emitted radiation strongly relies on the degree of asymmetry of the collapse. A perfectly spherically symmetric collapse would not induce GWs, whereas a highly asymmetric collapse might generate an intense emission of waves Figure 1.6.

The efficiency of emitted radiation is defined as the fraction of rest mass energy converted into gravitational waves. The possibility of strong radiation arises only when the event is a gravitational collapse with a formation of an NS or BH. Even in this case, the efficiency is a bit contentious.

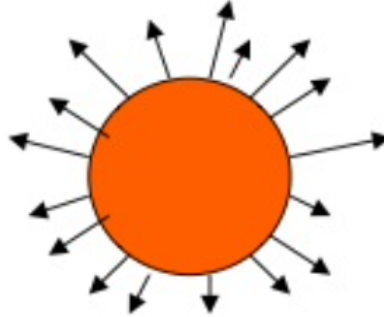


FIGURE 1.6: A pictorial representation of supernovae collapse.

There are two different approaches to studying wave emission. The first one follows the path of analyzing the gravitational collapse of a system in two or three dimensions, considering all the possible physics like magneto hydrodynamics, neutrino physics, and general relativity, in an attempt to get the time dependence of the quadrupole moment and hence the efficiency to convert rest mass-energy into GW energy.

In another approach, it is assumed that the collapse has already occurred, and the study follows the time evolution of a newly formed hot and rapidly rotating NS. Then, any non-axial symmetric phenomenon will transform rotational kinetic energy into GWs. Also, convective motions, vibrational modes of oscillation of the star, and non-axisymmetric emission of neutrinos can get converted into GW emission.

However, all the models used are not complete because of a lack of knowledge about the equation of state, viscosity and the difficulty in constructing a full 3-D numerical general relativistic hydrodynamical code that must also include magnetic and neutrino phenomena. This shows that theory itself is not enough to provide the efficiency of GW generation. But this is one typical characteristic in almost all the models that GWs efficiency depends on the progenitor star's angular momentum.

While the Supernovae rate in our Galaxy and the local group of galaxies (i.e. up to distances of the order of 300 kpc) is relatively low and probably less than one event per two decades (the last observed event was the famous Supernova 1987a), there might be one Supernova occurring about every two years between 3 and 5 Mpc from Earth [7]. A typical Supernova explosion event should generate GWs in the $10^2 - 10^3$ Hz frequency band, with a characteristic amplitude h_c that depends on the total amount of energy released under the form of GWs is given by

$$h \approx 2.7 \times 10^{-20} \left(\frac{\Delta E_{GW}}{M_{\odot} c^2} \right)^{\frac{1}{2}} \left(\frac{1 \text{ kHz}}{f} \right)^{\frac{1}{2}} \left(\frac{10 \text{ Mpc}}{r} \right) \quad (1.11)$$

where ΔE_{GW} is the energy lost in GWs, M_{\odot} is the solar mass, r is the distance and c is the speed of light.

The GW signals expected from different class of supernova are shown in Figure 1.7. The chance to detect gravitational burst is strongly dependent on the rate of the burst events. However, due to the Milky Way's isolation and the large distances required to substantially increase the target population's size, the amplitude distribution of bursts is highly non-uniform. Therefore, extreme events from our Galaxy are almost certainly rare, and to increase the event rate substantially, one needs to be able to detect events in the Virgo Cluster. Thus, to have a chance of catching several events per year, the sensitivity must be able to see characteristic amplitudes of less than 10^{-21} .

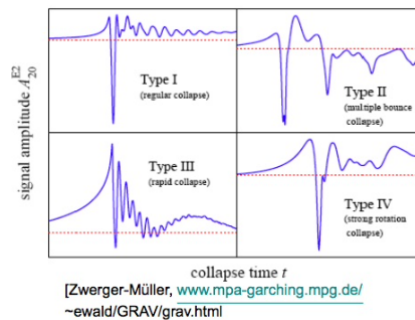


FIGURE 1.7: Calculated GW signals from different class of supernova.

1.3.3 Spinning Neutron Stars

When the mass distribution of a rotating neutron star is non-axisymmetric along the rotation axis, it emits GWs. This asymmetry in the mass distribution along the rotation axis can be due to the strong magnetic fields that distort the star, its history, which created the star in a deformed state, or accretion of matter from a companion object.

The emission of gravitational radiation can be studied under different categories.

1. If an NS has a mountain due to accretion, the rotation about its axis will result in the emission of waves. The mountain scenario is shown in the Figure 1.8.

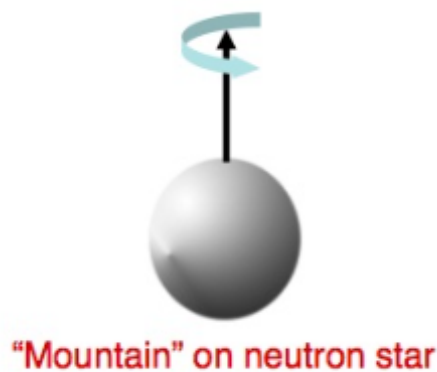


FIGURE 1.8: Mountain on spinning neutron star.

2. GWs can also be produced when the angular momentum of the NS precesses with the star's symmetry axis, as shown in the Figure 1.9. The maximum emission will occur when both the axis becomes orthogonal. It is because stars are not a perfect sphere and such a rigid body goes under a free precession. This motion is called wobbling that may arise due to the accretion from the companion body.

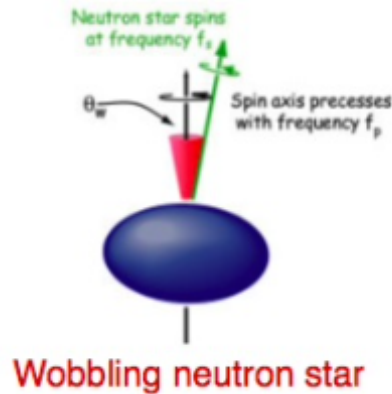


FIGURE 1.9: A wobbling neutron star.

3. An NS can also produce gravitational waves due to r-mode instability. These r-modes, also known as Rossby waves, have great significance in millisecond NS physics because they can generate GWs that carry away angular momentum, causing the star to spin down. The r-modes are shown in Figure 1.10.

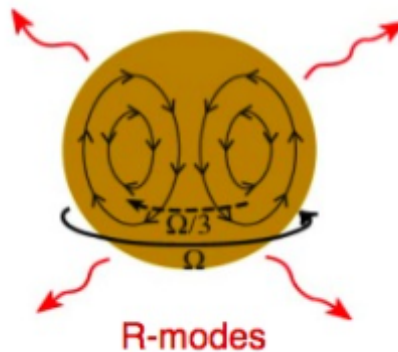


FIGURE 1.10: r-mode oscillations.

4. The final category is the emission of GWs through pulsar due to accretion. The accretion of material from surrounding causes changes in quadrupole moment, and if this accretion is continuous, there will always be gravitational radiation. Galaxy's low mass x-ray binaries have a spinning frequency around 300-700 Hz. Accretion of the material induces an increase in angular momentum of the star, while on the other hand, GWs carry this momentum away. The variation in quadrupole moment is due to the change in the structure of the NS crust, which results from the temperature gradient produced from the matter falling on the NS. This scenario is shown in Figure 1.11.



FIGURE 1.11: An accreting pulsar.

GW emission from NSs is a dawn of hope to understand the physics behind such a compact object. Presently our knowledge is limited on these stars. There are various open questions like; what makes pulsars pulse or glitch, superconductivity, solid core, the origin of the magnetic field of orders 10^{19} T or the matter which constitute them. It is believed that the Milky Way contains about a billions of neutron stars, more than 3000 (mostly pulsars) have been detected so far using EM observations. Figure 1.12 pictorially represents the possible interior structure of a NS.

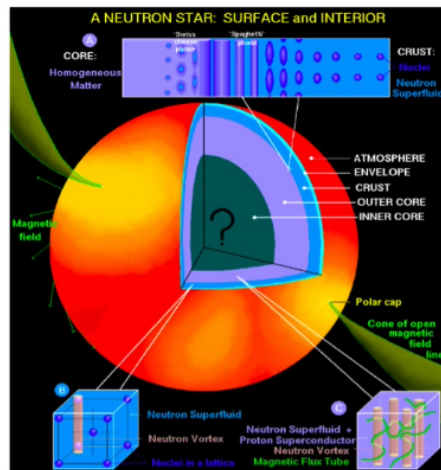


FIGURE 1.12: Interior structure of a neutron star.

A combined observation of GWs and EMWs can solve the puzzles of the interior of NSs like temperature, viscosity, high magnetic fields. This thesis presents GWs from an NS which contains a mountain. We shall study detailed analysis in the subsequent chapters.

1.3.4 Cosmological gravitational waves from the big bang

Cosmological GWs may be analogous to cosmic microwave background (CMB) radiation. For example, the origin of CMB comes from the epoch of the surface of the last scattering, when neutron gas first formed in the universe at a redshift of $z \sim 10^3$. So, CMB tells us about the universe when it was 10^5 years old. There should also be a similar background of neutrinos at a redshift of $z \sim 10^{10}$, which corresponds to 0.1 s after the Big Bang. GWs are weakly coupled to the matter, so the epoch of their release is $z \sim 10^{30}$ which corresponds to Planck time, 10^{-43} s and hence, they offer an excellent opportunity to view the universe at the time of its creation. But still, there are ambiguities in the signal amplitude of these waves. For example, some models suggest enhanced background resulting from the amplification of the GW signal due to cosmological inflation or phase transitions in the early

universe. But in the absence of amplification of background amplitude, we need to consider a thermal background that was in equilibrium at the extremely high energies of the Planck era. This background radiation is expected to be redshifted like any other radiation. Today this radiation would lie in the microwave regime with an amplitude of $h \sim 10^{-35}$, which is beyond the possibility of detection with current instruments. Figure 1.13 shows a pictorial view of the origin of cosmological GWs and the universe's evolution.

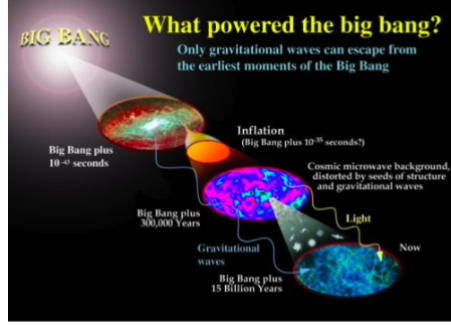


FIGURE 1.13: Origin of cosmological gravitational waves.

The intensity of the gravitational wave background is usually characterized by dimensionless quantity $\Omega_{GW}(f)$,

$$\Omega_{GW}(f) = \frac{1}{\rho_c} \frac{d\rho_{GW}}{d(\log f)} \quad (1.12)$$

where ρ_{GW} is the energy density of the stochastic background of gravitational waves, f is the frequency and ρ_c is the present value of the critical energy density for closing the Universe given by

$$\rho_c \equiv \frac{3H_0^2}{8\pi G} \quad (1.13)$$

The Hubble parameter H_0 is usually written as $H_0 = h_0 \times 100 \frac{km}{s-Mpc}$, where h_0 parametrizes the existing experimental uncertainty. We characterize stochastic GW background with the quantity $h_0^2 \Omega_{GW}(f)$ which represents the energy density per unit logarithmic interval of frequency [8].

Significant uncertainties influence the estimates for the background intensity. The most stringent limits on $h_0^2 \Omega_{GW}(f)$ come from the Big Bang nucleosynthesis model and observations

$$\int_{f=0}^{f=\infty} h_0^2 \Omega_{GW}(f) (d \log f) < 5.6 \times 10^{-6} (N_\nu - 3) \quad (1.14)$$

where N_ν is the effective number of neutrino species at the time of nucleosynthesis. The CMB anisotropies measured by the COBE experiment yields

$$h_0^2 \Omega_{GW}(f) < 7 \times 10^{-11} \left(\frac{H_0}{f} \right)^2, \quad 3 \times 10^{-18} \text{Hz} < f < 10^{-16} \text{Hz} \quad (1.15)$$

Even though violent astronomical events release enormous energy, we need very sensitive GW detectors to catch these signals. In the next section, we shall discuss the detectors briefly.

1.4 Gravitational Wave detectors

GW strain is generally minimal owing to a very weak coupling of gravity with the matter as compared to other forces. For instance, the peak GW strain during the first detection event was as small as 10^{-21} . Thus, it isn't easy to detect the GWs, and hence, it took elaborate efforts over many decades to devise an experimental setup sensitive enough to observe weak GW signals directly.

1.4.1 Current Detectors

In this section, we shall briefly discuss detectors which made the observations of GWs possible. Currently, four laser interferometric detectors are operational with the desired sensitivity. Two of them are USA based detectors, known as Laser Interferometer Gravitational-Wave Observatory (LIGO), and they are located in Hanford, Washington and Livingston, Louisiana. A third detector, known as Virgo, is situated in Cascina (near Pisa) whereas, a fourth one, known as KAGRA, is located at the Kamioka mine in Japan. It is worth mentioning that LIGO and Virgo are ground-based observatories whereas KAGRA is constructed underground. There is one more detector located in Hannover, Germany and it is called GEO600. The sensitivity of this detector is too low to detect a signal because of shorter arm lengths. Nevertheless, it is used as an R & D detector with exceptional importance in testing various technologies before implementing them in LIGO or Virgo.

The quest for GW detectors began in 1957 when Felix Pirani proposed the physical existence of gravitational radiation at the Chapel Hill conference [9]. Joe Weber, who listened to the talk of Pirani, came up with the idea of resonant bar detectors to observe GWs. Weber's detector was a massive aluminium cylinder vibrating in its longitudinal modes and it can be considered as two test masses connected to a spring. The principle behind these detectors is coupling between GW and test masses and the electromagnetic field is used as the motion transducer.

The first laser interferometers were proposed by Gertsenshtein and Pustovoit in 1962 [10]. and first built by Forward at Hughes Research Laboratories [11]. Later on, Rainer Weiss studied the noise and performance of such detectors in 1972 [12] and the continuous efforts of various scientists and engineers in different continents led to the first agreement between Massachusetts Institute of Technology (MIT) and California Institute of Technology (Caltech) for LIGO detectors in 1984. On the other hand due to the pioneering efforts of Allain Brillet in France and Adalberto Giazotto in Italy in mid 1980s the Virgo project was defined in 1989. Virgo was approved by the French National Centre for Scientific Research (CNRS), France in 1993 and then by the National Institute for Nuclear Physics (INFN), Italy in 1994.

GW interferometers are motivated by the Michelson interferometers where light travelling in two arms adds up to cause an interference pattern at the output (photodetector). In GR, GWs have only two tensor polarization states (h_+ and h_\times) which are obtained by imposing various gauge conditions known as Transverse-Traceless (TT) gauge. The physical significance of the word transverse is that the deformations in the arms are orthogonal to the direction of propagation of the wave, whereas, traceless means that if a wave passes in the z-direction, then one arm of the detector stretches in the y-direction and the other arm shrinks in the x-direction and vice versa in such a way that the volume is not changed. The interaction of the laser interferometer with the GWs can be understood in terms of the geodesic equation and the equation of the geodesic deviation. These instruments perform near the dark fringe, which corresponds to the complete destructive interference at the output without

any GW signal. The current GW interferometers are designed to detect GWs in the frequency range $\sim [10,1000]$ Hz with a strain amplitude (h) of the order 10^{-21} . The formula below gives the expression for strain amplitude

$$h = \frac{2\Delta L}{L} \quad (1.16)$$

where L is the length of the arm and ΔL is the change in the arm induced by a passing GW. This change in length of the arms is decoded in terms of fringes at the photodetector. The formula of strain suggests that a very long arm helps in the detection but, this is challenging for practical and economic constraints. On the other hand, if the arm is very long, GW amplitude changes with time during the round trip of light in the arms. A time average of this change will in turn scale down the sensitivity of the detector. By taking these arguments into account, the arm length for LIGO has been chosen to be 4 km and that of Virgo and KAGRA is 3 km. Although a very long arm is not feasible, one can still make the light storage time higher without extending the interferometer using a Fabry-Perot (FP) cavity. The FP cavity is a resonant cavity where the stored resonating electromagnetic field enables us to increase the effective length of the interferometer and make the apparatus more sensitive. For LIGO, this results in the bouncing of light 300 times by making the effective length of the interferometer to be 1200 km. This increased effective length reduces one important noise - the photon shot noise described below but not other sources of noise like the thermal noise.

The most phenomenal aspect of the GW interferometers is their sensitivity which allows them to detect very feeble signals. But the hypersensitivity of these detectors also turns out to be their drawback because they are susceptible to various noise sources. A GW signal is buried under the resultant of various noises which imposes a great challenge to extract this signal. The noise sources dominating at the low frequency are seismic noise and thermal noise from the suspension wires. In the mid-frequency range, noise is dictated by the thermal noise of the mirrors, whereas at high frequency, the shot noise has higher influence. In the subsequent paragraphs, we shall discuss these noise sources briefly.

The sources of seismic noise are the continuous movement of the earth's crust in a wide frequency range, bad weather or a heavy vehicle passing nearby. To reduce this noise, the Virgo detector suspends the mirror with a chain of oscillators which attenuate vibrations in all the six degrees of freedom, whereas, the LIGO detector uses a 4-stage pendulum called a 'quad'. The KAGRA detector has been constructed underground to minimize the seismic noise as well as gravity gradient noise. Another source of noise at the low frequency is the thermal noise from wires due to the random motion of molecules. To overcome this issue, the LIGO and Virgo use monolithic fused silica wires to suspend the mirrors.

In the mid-frequency range the most important are the Brownian noise and the thermoelastic noise due to irreversible thermodynamic processes triggered by thermal conductivity. These noises are reduced by introducing large and heavy (40 kg) mirrors both in LIGO and Virgo as well as low loss coating (TiO₂ dopants) which reduces mechanical dissipation. The noise can be further cut down by cooling the mirrors to a low temperature and using a larger beam size on the mirror. To this end the KAGRA detector uses cryogenic mirrors.

In the high-frequency range, the noise is related to the measuring of optical

power at the photodetector. The measuring of optical power is equivalent to counting the number of photons arriving during a measurement interval and the probability distribution of photons is given by the Poisson law. There is a displacement noise at the output due to the fluctuations in the number of photons which is known as shot noise. The shot noise can be reduced by increasing the power arriving at the output. Also, fringes in the photodetector become sharper with an increase in the number of photons. As photons carry momentum, an increase in the power exerts more mechanical pressure fluctuations on the mirrors and this is known as radiation pressure noise. This situation is conceptually similar to the Heisenberg microscope. It is remarkable to witness how a quantum effect due to the uncertainty principle can be crucial in the measurement of the position of a macroscopic body, like the mirror of an interferometer, which typically weighs 40 kg. To minimize the combination of shot noise and radiation pressure noise, the detectors should work at optimal power P_{opt}

$$P_{opt} = \pi c \lambda m f^2 \quad (1.17)$$

where c is the speed of light, λ is the wavelength of the laser, m is the mass of the mirror and f is the frequency of the GW.

The input power of LIGO is 40 W and that of Virgo is 18 W but the formula for optimal power suggests the need of a higher power of about 360 MW for the desired sensitivity. This power crisis problem is also ironed out with the help of the FP cavity. In the LIGO detector, the power is increased to 750 kW by making 300 roundtrips in the FP cavity. whereas, the power enhancement in the Virgo is 650 kW by making 280 roundtrips. Besides using the FP cavity, the power is also recycled by placing a partial transmitting mirror between the laser and beam splitter. On the other hand, the signal is also recycled by installing a partially reflective mirror between the beam splitter and photodetector. As we have recycled both the power and the signal, the interferometer is called the Dual recycled Fabry-Perot Michelson interferometer. Figure 1.14 shows a simplified optical configuration and Figure 1.15 displays an aerial view of the Virgo detector which is located in Cascina, Italy.

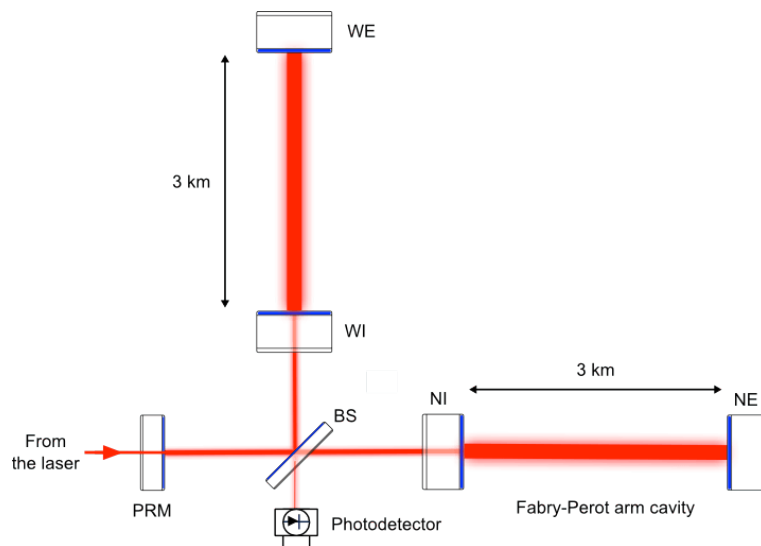


FIGURE 1.14: Optical system of Virgo detector (Credits: The Virgo Collaboration)

With the three detectors we can determine the location of the source of gravitational waves from a coalescing binary system. The locus of time delay in two



FIGURE 1.15: Aerial view of Virgo (Credits: The Virgo Collaboration)

detectors forms an annulus. If we include the third detector, the annuli intersect at two different points, one of which is the location of the source while the other point is the mirror image of the source. One can resolve this ambiguity using additional information about sky location contained in the amplitudes of the responses of the detectors to the gravitational wave signal (see [13] for details). The presence of four or more detectors improves considerably the sky localization [14].

1.4.2 Future Detectors

The accomplishment of current detectors has inspired scientists and funding agencies to explore the cosmos by investing in future detectors with enhanced performance. We shall consider future projects in this section.

The current LIGO instruments are planned for an upgrade to LIGO A+ by 2025. One of the major improvements is the introduction of frequency-dependent light squeezing to reduce shot noise at low frequency and radiation pressure noise at high frequency. Other changes involve the replacement of mirrors that have low thermal noise in the coating and low scattered light. The Virgo detector is also going through similar changes and it is called AdV+. These improvements are expected to increase the sensitivity by a factor of 2 and hence the reachable volume in space increases by a factor of 8. With this sensitivity, we can detect 17-300 BBH/month and 1-13 BNS/month which would help in population studies and imposing constraints on the Hubble parameter. Besides LIGO A+ and AdV+, a third LIGO detector is also going to be operational in the Hingoli district, Maharashtra, India in the late 2020s. LIGO India is jointly funded by the National Science Foundation (NSF), USA, the Department of Atomic Energy (DAE) and the Department of Science and Technology (DST), Government of India. The addition of a fifth detector will help in the sky localization and increase the fraction of time that all the instruments are operating.

There are also plans for building very sophisticated third-generation detectors in 2030s by implementing advanced technologies. The European project, Einstein Telescope (ET) [15], is planned to be an underground detector with 10 km arms. It consists of two detectors, one at low frequency for BHBH merger and the other at a higher frequency for NSNS signals. This entire setup has a triangular shape which allows us to extract the polarization of the signal just by using one observatory. The US Cosmic Explorer (CE) [16] is an L-shaped ground-based detector with 40 km arms. Both ET and CE are expected to have 10 times higher sensitivity which means that they can record 1000 times more events as compared to current detectors.

The ground-based detectors are sensitive to stellar-mass objects in the range from around one solar mass to around hundred solar masses because the frequency emitted by them lies between 5 Hz to a few kHz. But various objects in the universe emit at lower frequency and this suggests the need for a detector in space. The Laser Interferometer Space Antenna (LISA) is a space-based detector funded by European Space Agency (ESA) with a substantial contribution from the National Aeronautics and Space Administration (NASA) and it is planned to be launched in 2034 [17]. It is a triangular-shaped detector with 2.5 million km arms and sensitive to the frequency range from around 100 mHz to around 0.1 Hz. This instrument is designed to witness the events like white dwarf binaries, the inspiral of a compact object into a massive black hole in the centre of a galaxy or massive distant black hole binaries with a long coalescence period. LISA may also be able to detect mHz stochastic GW background which could be produced by processes occurring at the TeV scale in the early Universe. With this detector, there is a hope to test the no-hair property of BHs as well as imposing constraints on dark matter candidates and modified theories of gravity.

There is also a quest for searching low-frequency GW by using a network (array) of pulsars. Pulsars are very accurate clocks with a great homogeneity in pulse profile, and little variation in frequency. A passing GW can induce a phase shift in the pulse profile and using the data from different pulsars allows us to make an indirect observation of GW. The International Pulsar Timing Array (IPTA) [18] uses pulsars to detect lower frequency GW from slowly moving supermassive black holes at the centres of galaxies. The IPTA consists of the European Pulsar Timing Array (EPTA), NANOGrav from the US and Canada and Parkes Pulsar Timing Array (PPTA) which is an Australian collaboration.

Chapter 2

Gravitational Waves Polarizations in Brans-Dicke theory

2.1 Introduction

Isaac Newton believed that inertial forces such as centrifugal forces must arise from the acceleration with respect to "absolute space." On the other hand, Ernst Mach argued that inertial forces are more likely caused by acceleration with respect to the mass of the celestial bodies, and this idea is known as Mach's principle. This principle made a substantial contribution to the development of a new scalar-tensor theory of gravitation which is known as Brans-Dicke (BD) theory proposed by Carl Brans and Robert Dicke [5]. The foundations of BD theory are built on the previous work of Pascual Jordan [19] as well as Markus Fierz [20], and sometimes this theory is also referred to as Jordan-Fierz-Brans-Dicke theory.

In the last 100 years, GR has successfully passed various experimental tests proving itself to be the most promising theory of gravity. But then a natural question arises, why is there a quest to find an alternative theory of gravity? There are plenty of reasons that justify this question, and one of them is related to understanding the accelerated expansion of the universe. It is more reasonable to substitute GR by an alternative theory of gravity instead of introducing the concept of dark energy in Einstein's field equations to expound this expansion. This is because dark energy does not fit the standard model, and also its nature is not perceived by the laws of modern physics [21]. But while exploring new models of gravity, one must discern that any new theory must obey some constraints imposed by field theory. GR is also a field theory and the following rules determine the credibility of any new theory of gravity:

1. There should exist vibrational modes which are freely excitable in the absence of any source. They are also called degrees of freedom (DOF). So, a theory is classified by the number of vibrational modes and the spin of these modes.
2. The next characteristic is the propagation of these modes in an empty space. If the mode is massless, we have Coulomb potential, which results in the long-range force. On the other hand, a massive mode generates Yukawa potential, which is responsible for short-range force.
3. Finally, one needs to consider the interaction of these modes with themselves as well as other fields.

We can verify the efficacy of these requirements in the BD theory. This theory has three DOF. The first two of them are same as in GR. They are known as tensor polarization or spin-2 massless graviton. The third polarization is known as

scalar polarization or spin-0 graviton. All three polarizations are massless because gravity is a long-range force and gravitational waves travel with the speed of light. The interaction of modes can be understood by considering the Einstein equivalence principle (EEP). The BD theory satisfies the EEP, and hence it is a metric theory of gravity. And in metric theories of gravity, only the metric (g) interacts with the matter. So, the scalar field mediates in such a way that it generates a gravitational field along with the matter. Once the gravitational field is set up, it produces a metric which in turn acts back on the matter as described by EEP, but the scalar field cannot respond to the matter directly [22]. For example, let us consider the Schwarzschild metric generated by a compact object. The other astronomical objects in the universe (planets, galaxies, etc.) will source this scalar field and hence deviate the resultant metric from the Schwarzschild metric. In this theory, Newton's constant of gravitation G is not constant anymore, but G is determined by the totality of the matter in the universe through an auxiliary field equation. This theory still has general coordinate invariance, but it has an additional degree of freedom $\phi(x)$ that determines the strength of gravity. In the presence of the scalar field, Einstein's equation modifies to

$$G_{\mu\nu} = f(\phi) \left[T_{\mu\nu}^{(matter)} + T_{\mu\nu}^{(\phi)} \right] \quad (2.1)$$

where $f(\phi)$ is a coupling constant analogous to the Newton's constant in the GR, and it depends on ϕ , which in turn depends on position (x). $T_{\mu\nu}^{(matter)}$ is the energy-momentum tensor produced by the matter, and $T_{\mu\nu}^{(\phi)}$ is energy-momentum tensor produced by the scalar field ϕ .

Although BD theory satisfies the EEP, it does not meet the strong equivalence principle (SEP). This is true because the value of coupling constant depends on ϕ , which itself depends on the position. On the other hand, a form of velocity dependence in local physics can also enter indirectly if the value of the scalar field changes with time. Then the rate of variation of the coupling constant could depend on the velocity of the frame. It is worth noting that GR is the only theory which satisfies SEP otherwise all metric theories violates this principle at some level [22]. Also for the sake of complete introduction of the BD theory, we should mention that it is a purely dynamical theory which means coupled partial differential equations govern its structure and evolution [22].

2.2 Experimental tests of Brans-Dicke theory

2.2.1 Post-Newtonian and Parameterized post-Newtonian formalism

To understand the experimental tests of the BD theory in the weak-field limit, we need to digress a little bit and get an idea of the post-Newtonian (PN) expansion and parameterized post-Newtonian (PPN) framework. In the PN expansion, we expand the metric in the powers of $\frac{v}{c}$. This approach is valid in the weak-field limit and slow-motion approximation ($v \ll c$). When the speed of gravity approaches infinity, we get back to the Newtonian potential. In the PPN formalism, we add parameters (coefficients) in front of the potentials obtained by PN expansion and add a few new potentials with their own parameters. This allows us to obtain a framework that encompasses a broad spectrum of alternative theories, and that can be used to calculate a wide range of testable phenomena. The only aspect that changes from one theory of gravity to the other is the numerical value of the various coefficients that appear in front of the potentials [22], [23].

There are ten independent parameters which appear in the PPN formalism which are named as $\gamma, \beta, \zeta, \alpha_1, \alpha_2, \alpha_3, \zeta_1, \zeta_2, \zeta_3$ and ζ_4 . A heuristic interpretation of these parameters is given below:

- γ : It measures spatial curvature produced by unit rest mass.
- β : It measures non-linearity in gravity.
- ζ : It is non-zero in any theory of gravity that predicts preferred-location effects such as a galaxy-induced anisotropy in the local gravitational constant.
- $\alpha_1, \alpha_2, \alpha_3$: They measure whether or not the theory predicts post-Newtonian preferred-frame effects.
- $\zeta_1, \zeta_2, \zeta_3, \zeta_4$: They determine whether the linear momentum and angular momentum are conserved or not.

The value of γ is 1 in GR and $\frac{1+\omega_{BD}}{2+\omega_{BD}}$ in BD where ω_{BD} is a parameter in BD theory defined below in the next subsection. The parameter β is unity in both theories. Also, parameters α_i and ζ_i vanish in GR as well as BD, and hence both theories are conservative with no preferred-frame effects. To test the BD theory, we need to measure the value of γ with the help of experiments. Once γ is obtained, we can infer the value of BD parameter ω_{BD} . For a detailed analysis on PN and PPN formalism, refer to [22], [23], [24].

2.2.2 Experimental tests of BD theory in the weak-field limit

The weak-field limit parameter ϵ is given by

$$\epsilon = \frac{GM}{Rc^2} \quad (2.2)$$

where G is the Newtonian gravitational constant, M is the characteristic mass scale of the phenomenon, R is the characteristic distance scale, and c is the speed of light.

In the weak-field limit $\epsilon \ll 1$. This is the case when we study a phenomenon in the Solar system where $\epsilon < 10^{-5}$.

Measurement of γ : In the BD theory, the value of the parameter ω_{BD} is constant. As ω_{BD} tends to infinity, γ tends to unity, and the BD theory is no different from GR. Also, a higher value of ω_{BD} diminishes the effect of the scalar field. Below we shall discuss the bounds obtained on the value of γ from different experimental tests. These methods are:

1. **The deflection of light:** The development of very-long-baseline radio interferometry (VLBI) helped scientists to measure the deflection of light with better accuracy. Early measurements took advantage of a series of the heavenly coincidences where groups of strong quasistellar radio sources pass very close to the Sun. A 1995 VLBI measurement using 3C273 and 3C279 yielded $\gamma - 1 = (-8 \pm 34) \times 10^{-4}$ [25]. A 2009 measurement using the Very Long Baseline Array (VLBA) targeting the same two quasars plus two other nearby radio sources yielded $\gamma - 1 = (-2 \pm 3) \times 10^{-4}$ [26]. In recent years, transcontinental and intercontinental VLBI observations of quasars and radio galaxies have been made primarily to monitor the Earth's rotation. A 2004 analysis of almost 2 million VLBI observations of 541 radio sources, made by 87 VLBI sites yielded $\gamma - 1 = (-1.7 \pm 4.5) \times 10^{-4}$ [27]. Analyses that incorporated data through 2010 yielded $\gamma - 1 = (-0.8 \pm 1.2) \times 10^{-4}$ [28, 29, 22].

2. **The time delay of light:** A radar signal sent across the solar system past the Sun to a planet or satellite and returned to the Earth suffers an additional non-Newtonian delay in its round-trip travel time. A significant improvement in the value of γ was reported in 2003 from Doppler tracking of Cassini spacecraft while it was on its way to Saturn, with a result $\gamma - 1 = (2.1 \pm 2.3) \times 10^{-5}$ [30]. Using this result, one obtains that massless scalar-tensor theories must have $\omega_{\text{BD}} > 40000$ to be compatible with this constraint [22].

Constancy of G: We have seen that G is not constant in BD theory. So, measuring the quantity $\frac{\dot{G}}{G}$ can provide a deviation from GR. The best limits on a current $\frac{\dot{G}}{G}$ come from improvements in the ephemeris of Mars using range and Doppler data from the Mars Global Surveyor (1998-2006), Mars Odyssey (2002-2008), and Mars Reconnaissance Orbiter (2006-2008), together with improved data and modeling of the effects of the asteroid belt. The limits on $\frac{\dot{G}}{G}$ thus obtained are $(0.1 \pm 1.6) \times 10^{-13} \text{yr}^{-1}$ [31, 32, 22]. There are also some constraints imposed using the recent GW observations of binary neutron stars. The events GW170817 and GW190425 yields $-7 \times 10^{-9} \text{yr}^{-1} \lesssim \frac{\dot{G}}{G} \lesssim 5 \times 10^{-8} \text{yr}^{-1}$ and $-4 \times 10^{-9} \text{yr}^{-1} \lesssim \frac{\dot{G}}{G} \lesssim 2 \times 10^{-8} \text{yr}^{-1}$ respectively [33]. There are also upper bounds on the variation of G obtained from pulsating white dwarfs. For example, the upper bound using the white dwarf G117-B15A is $\frac{\dot{G}}{G} \approx -1.8 \times 10^{-10} \text{yr}^{-1}$, whereas the bound obtained from R548 is $\frac{\dot{G}}{G} \approx -1.3 \times 10^{-10} \text{yr}^{-1}$ [34].

Nordtvedt effect: Nordtvedt showed that many metric theories of gravity predict that massive bodies violate the weak equivalence principle, that is, fall with different accelerations depending on their gravitational self-energy [35]. This violation of the equivalence principle by massive bodies is known as the "Nordtvedt effect" and measured by the parameter η_N . In GR, η_N is zero, and a non-zero value of η_N gives the deviation from GR. Various experiments have been carried out to measure this effect but the one conducted by Eöt-Wash group is the most enhanced test. In this experiment, WEP was examined for laboratory bodies whose chemical compositions mimic that of the Earth and Moon, and they obtained the result $|\eta_N| = (4.4 \pm 4.5) \times 10^{-4}$ [22].

2.2.3 Experimental tests of BD theory in strong-field limit

The value of $\epsilon \approx 1$ defines the strong-field regime. It corresponds to a region in the vicinity of a neutron star or black hole. To test the theories of gravitation in a strong gravity regime, one can consider a binary system. It is known that the orbit of inspiralling binary will decay because of the emission of gravitational radiation. In GR, there is only quadrupolar emission, but scalar-tensor theories also predict dipolar emission. One can test the dipole radiation by observing the rate of change of the orbital period. Before we consider known binary systems, it is worth mentioning two propositions:

- In a binary system with identical objects, dipole emission is suppressed. For example, a system having two neutron stars will result in weak dipole radiation, if there is any [22].
- Roger Penrose proposed that black holes in BD theory are identical to their GR counterparts. Motivated by this remark, Thorne and Dykla showed that during gravitational collapse to form a black hole, the BD scalar field is radiated away, in accord with Price's theorem, leaving only its constant asymptotic value, and a GR black hole [36, 22].

Although Hulse-Taylor binary (PSR 1913+16) confirmed the existence of gravitational radiation in GR, it could not provide a reliable test for dipole radiation because of the mass ratio of the system.

However, the discovery of binary pulsar systems with a white dwarf companion, such as J1738+0333, J1141-6545 and J0348+0432 has made it possible to perform robust tests of the existence of dipole radiation. This is because such systems are necessarily asymmetrical. Already, significant bounds have been placed on dipole radiation using J1738+0333 and J1141-6545 [37, 38]. Also, constraints have been put on the dipole radiation using the event GW170817 [39].

2.2.4 Search for nontensorial gravitational waves

Another approach to test the BD theory in the strong-field regime is to search for gravitational radiation from isolated rotating neutron stars [40]. One can search for scalar, vector or tensor polarizations in LIGO, Virgo, and KAGRA gravitational detector data [41] [42] [43]. In [44], the first search has been carried in LIGO detector data from its first observational run for around 200 known pulsars without relying on any particular alternative theory of gravity. This investigation could not discover any GW signal, but it imposed upper limits for scalar, vector and tensor amplitudes [4].

2.3 Polarizations

The action S in the BD theory is written in the Jordan-Fierz frame

$$S = S_g[g_{\mu\nu}, \varphi] + S_m[\psi_m, g_{\mu\nu}] \quad (2.3)$$

$$S_g \equiv \frac{1}{16\pi} \int d^4x \sqrt{-g} \left[\varphi R - \frac{\omega_{BD}}{\varphi} \nabla^\mu \varphi \nabla_\mu \varphi \right] \quad (2.4)$$

$$S_m \equiv \int d^4x \sqrt{-g} \mathcal{L}_m[\psi_m, g_{\mu\nu}] \quad (2.5)$$

where

$g_{\mu\nu}$ is the metric tensor, φ is the scalar field, ω_{BD} is a parameter which measures how strongly φ couples to the matter content, ψ_m are the matter fields and \mathcal{L}_m is the Lagrangian of matter fields. The scalar field is not just added to the gravitational tensor field, but arises through the nonminimal coupling term. P. Jordan was trying to embed four-dimensional curved space in five-dimensional flat spacetime. He proved that a constraint in formulating projective geometry could be a four-dimensional scalar field, which allows one to describe a spacetime-dependent gravitational "constant," as initially proposed by P. A. M. Dirac [45].

The field equations are obtained by varying the action S with respect to the metric tensor $g^{\mu\nu}$ and the scalar field φ . This gives

$$R_{\mu\nu} - \frac{1}{2} R g_{\mu\nu} = \frac{8\pi}{\varphi} T_{\mu\nu} + \frac{\omega_{BD}}{\varphi^2} \left[\partial_\mu \varphi \partial_\nu \varphi - \frac{1}{2} g_{\mu\nu} g^{\alpha\beta} \partial_\alpha \varphi \partial_\beta \varphi \right] + \frac{1}{\varphi} \left[\nabla_\mu \partial_\nu \varphi - g_{\mu\nu} g^{\alpha\beta} \nabla_\alpha \partial_\beta \varphi \right] \quad (2.6)$$

$$R - \frac{\omega_{BD}}{\varphi^2} g^{\mu\nu} \partial_\mu \varphi \partial_\nu \varphi + 2 \frac{\omega_{BD}}{\varphi} g^{\mu\nu} \nabla_\mu \partial_\nu \varphi = 0 \quad (2.7)$$

where $R_{\mu\nu}$ is the Ricci tensor, R is the Ricci scalar and $T_{\mu\nu}$ is defined as

$$T_{\mu\nu} \equiv -\frac{2}{\sqrt{-g}} \frac{\delta S_m}{\delta g^{\mu\nu}} \quad (2.8)$$

Our goal is to solve Eq. (2.6) and Eq. (2.7) simultaneously and eliminate the curvature terms. To do so, we multiply Eq. (2.6) by $g^{\mu\nu}$ and subtract it from Eq. (2.7). The multiplication of Eq. (2.6) with $g^{\mu\nu}$ and using the conditions that $g^{\mu\nu}g_{\mu\nu} = 4$, $g^{\mu\nu}R_{\mu\nu} = R$ and $g^{\mu\nu}T_{\mu\nu} = T$, gives

$$-R = \frac{8\pi}{\varphi} T - \frac{\omega_{BD}}{\varphi^2} \partial_\mu \varphi \partial^\mu \varphi - \frac{3}{\varphi} \nabla_\mu \partial^\mu \varphi \quad (2.9)$$

By solving Eq. (2.9) and Eq. (2.7) simultaneously, we get

$$\frac{(3 + 2\omega_{BD})}{\varphi} \nabla_\mu \partial^\mu \varphi = \frac{8\pi}{\varphi} T \quad (2.10)$$

To study the local wave zone solution, we linearize the equations by considering

$$g_{\mu\nu}(x) = \eta_{\mu\nu} + h_{\mu\nu}(x) \quad (2.11)$$

$$\varphi(x) = \varphi_0 + \delta\varphi(x) = \varphi_0 \left[1 + \frac{\delta\varphi}{\varphi_0} \right] \quad (2.12)$$

where

$$\varphi_0 \equiv \frac{4 + 2\omega_{BD}}{(3 + 2\omega_{BD}) G} \quad (2.13)$$

In the above equations, $\eta_{\mu\nu}$ is the metric of flat spacetime, $h_{\mu\nu}$ is a small perturbation in the Minkowski spacetime with $|h_{\mu\nu}| \ll 1$ and $|\delta\varphi| \ll \varphi_0$. In the limiting case when ω_{BD} tends to infinity, we are into the regime of general relativity i.e. $\varphi_0 = G^{-1}$. We also make use of the fact that covariant derivative becomes an ordinary derivative ($\nabla_\mu \approx \partial_\mu$) in the process of linearization.

The expressions for Affine connection, Riemann curvature tensor, Ricci tensor and Ricci scalar in terms of a generic metric $g_{\mu\nu}$ are

$$\Gamma_{\alpha\beta}^{\mu} = \frac{1}{2}g^{\mu\nu} [\partial_{\alpha}g_{\beta\nu} + \partial_{\beta}g_{\nu\alpha} - \partial_{\nu}g_{\alpha\beta}] \quad (2.14)$$

$$R_{\mu\nu\rho\sigma} = g_{\rho\lambda} [\partial_{\mu}\Gamma_{\nu\sigma}^{\lambda} - \partial_{\nu}\Gamma_{\mu\sigma}^{\lambda} + \Gamma_{\mu\eta}^{\lambda}\Gamma_{\nu\sigma}^{\eta} - \Gamma_{\nu\eta}^{\lambda}\Gamma_{\mu\sigma}^{\eta}] \quad (2.15)$$

$$R_{\mu\nu} = g^{\rho\sigma}R_{\rho\mu\sigma\nu} \quad (2.16)$$

$$R = g^{\mu\nu}R_{\mu\nu} \quad (2.17)$$

The corresponding linearized expressions in terms of a small perturbation $h_{\mu\nu}$ are

$$\Gamma_{\alpha\beta}^{\mu} = \frac{1}{2} [\partial_{\alpha}h^{\mu}_{\beta} + \partial_{\beta}h^{\mu}_{\alpha} - \eta^{\mu\rho}\partial_{\rho}h_{\alpha\beta}] + \mathcal{O}(h^2) \quad (2.18)$$

$$R_{\mu\nu\rho\sigma} = \frac{1}{2} [\partial_{\rho}\partial_{\nu}h_{\mu\sigma} + \partial_{\sigma}\partial_{\mu}h_{\nu\rho} - \partial_{\sigma}\partial_{\nu}h_{\mu\rho} - \partial_{\rho}\partial_{\mu}h_{\nu\sigma}] + \mathcal{O}(h^2) \quad (2.19)$$

$$R_{\mu\nu} = \frac{1}{2} [\partial_{\tau}\partial_{\mu}h^{\tau}_{\nu} + \partial_{\nu}\partial_{\tau}h^{\tau}_{\mu} - \square h_{\mu\nu} - \partial_{\mu}\partial_{\nu}h] + \mathcal{O}(h^2) \quad (2.20)$$

$$R = \partial_{\mu}\partial_{\nu}h^{\mu\nu} - \square h + \mathcal{O}(h^2) \quad (2.21)$$

By linearizing Eq. (2.6) in the vacuum ($T_{\mu\nu} = 0$), we get

$$R_{\mu\nu} - \frac{1}{2}\eta_{\mu\nu}R = \omega[\partial_{\mu}\Phi\partial_{\nu}\Phi - \frac{1}{2}\eta_{\mu\nu}\partial^{\alpha}\Phi\partial_{\alpha}\Phi] + [-\partial_{\mu}\partial_{\nu}\Phi + \eta_{\mu\nu}\partial^{\alpha}\partial_{\alpha}\Phi] \quad (2.22)$$

where $\Phi \equiv -\frac{\delta\varphi(x)}{\varphi_0}$.

We can ignore the terms in the first square brackets on the right-hand side of Eq. (2.22) because they are of the second order in Φ . Hence, Eq. (2.22) can be written as

$$R_{\mu\nu} - \frac{1}{2}\eta_{\mu\nu}R = -\partial_{\mu}\partial_{\nu}\Phi + \eta_{\mu\nu}\square\Phi \quad (2.23)$$

where $\square \equiv \partial^{\alpha}\partial_{\alpha}$ is the d'Alembert operator. Similarly, we can linearize Eq. (2.10) in the vacuum and get

$$\frac{(3 + 2\omega_{bd})}{\varphi}\nabla_{\mu}\partial^{\mu}\varphi \approx \frac{3 + 2\omega_{bd}}{1 + \frac{\delta\varphi}{\varphi_0}}\partial_{\mu}\partial^{\mu}\frac{\varphi_0 + \delta\varphi}{\varphi_0} = 0 \quad (2.24)$$

or,

$$\square\Phi = 0 \quad (2.25)$$

In Eq. (2.24), $\partial^{\mu}[\varphi_0 + \delta\varphi] = \partial^{\mu}[\delta\varphi]$ because φ_0 is constant for a fixed ω_{bd} .

We can now impose various gauge conditions to extract the number of independent components and simplify the field equations. We start with infinitesimal coordinate transformations known as gauge transformations. They are of the form

$$x'^{\mu} = x^{\mu} + \xi^{\mu} \quad (2.26)$$

such that $|\partial_{\nu}\xi^{\mu}| \ll 1$.

In this new primed coordinate system, $g_{\mu\nu}$ is transformed as

$$g'_{\mu\nu} = \eta_{\mu\nu} + h'_{\mu\nu} \quad (2.27)$$

where $h'_{\mu\nu}$ is defined as

$$h'_{\mu\nu} \equiv h_{\mu\nu} - \partial_{\mu}\xi_{\nu} - \partial_{\nu}\xi_{\mu} \quad (2.28)$$

The scalar field remains the same in new coordinate because scalars are invariant under coordinate transformations.

$$\Phi(x) \rightarrow \Phi'(x) = \Phi(x) \quad (2.29)$$

Under this gauge transformation, the Riemann tensor is invariant. In order to derive wave equation, we define

$$\bar{h}_{\mu\nu} \equiv h_{\mu\nu} - \frac{1}{2}\eta_{\mu\nu}h + \eta_{\mu\nu}\Phi \quad (2.30)$$

$$\bar{h} \equiv \eta^{\mu\nu}\bar{h}_{\mu\nu} \quad (2.31)$$

$$h \equiv \eta^{\mu\nu}h_{\mu\nu} \quad (2.32)$$

Multiplying the Eq. (2.30) by $\eta^{\mu\nu}$ on both sides and using the fact that $\eta^{\mu\nu}\eta_{\mu\nu} = 4$, we get

$$\bar{h} = h - \frac{1}{2}4h + 4\Phi \quad (2.33)$$

$$\bar{h} = -h + 4\Phi \quad (2.34)$$

We use the relation in Eq. (2.34) to express $h_{\mu\nu}$ in terms of $\bar{h}_{\mu\nu}$. This allows us to write the Eq. (2.23) in terms of $\bar{h}_{\mu\nu}$.

$$h_{\mu\nu} = \bar{h}_{\mu\nu} + \frac{1}{2}\eta_{\mu\nu}h - \eta_{\mu\nu}\Phi \quad (2.35)$$

$$h_{\mu\nu} = \bar{h}_{\mu\nu} + \frac{1}{2}\eta_{\mu\nu}[-\bar{h} + 4\Phi] - \eta_{\mu\nu}\Phi \quad (2.36)$$

$$h_{\mu\nu} = \bar{h}_{\mu\nu} - \frac{1}{2}\eta_{\mu\nu}\bar{h} + \eta_{\mu\nu}\Phi \quad (2.37)$$

To expand Eq. (2.23) in terms of $\bar{h}_{\mu\nu}$, we need to express Ricci tensor and Ricci scalar in terms of $h_{\mu\nu}$ which can be further written down in terms of $\bar{h}_{\mu\nu}$ using the Eq. (2.37). This can be done as

$$R_{\mu\nu} = \frac{1}{2} [\partial_{\mu}\partial_{\alpha}h_{\nu}^{\alpha} + \partial^{\alpha}\partial_{\nu}h_{\mu\alpha} - \square h_{\mu\nu} - \partial_{\mu}\partial_{\nu}h] \quad (2.38)$$

$$R = \partial^{\nu}\partial^{\rho}h_{\rho\nu} - \square h \quad (2.39)$$

Using Eq. (2.37), Eq. (2.38) and Eq. (2.39), Eq. (2.23) can be written as

$$\begin{aligned} \frac{1}{2}\partial_\mu\partial^\rho\bar{h}_{\rho\nu} + \frac{1}{2}\partial_\nu\partial^\alpha\bar{h}_{\mu\alpha} - \partial_\mu\partial_\nu\Phi - \frac{1}{2}\square\bar{h}_{\mu\nu} + \frac{1}{2}\eta_{\mu\nu}\square\left(\frac{\bar{h}}{2} - \Phi\right) - \eta_{\mu\nu}\partial^\alpha\partial^\beta\bar{h}_{\alpha\beta} - \frac{1}{2}\eta_{\mu\nu}\square\left(\frac{\bar{h}}{2} - 3\Phi\right) \\ = -\partial_\mu\partial_\nu + \eta_{\mu\nu}\square\Phi \end{aligned}$$

After some algebraic manipulations, we rewrite the above equation in a simpler form as

$$\square\bar{h}_{\mu\nu} - \partial_\mu\partial^\alpha\bar{h}_{\alpha\nu} - \partial_\nu\partial^\alpha\bar{h}_{\alpha\mu} + \eta_{\mu\nu}\partial^\alpha\partial^\beta\bar{h}_{\alpha\beta} = 0 \quad (2.40)$$

The next step is to express Eq. (2.40) in the primed coordinate system. To do so, we need to find the expression for h' to find \bar{h}'

$$h'_{\mu\nu} = h_{\mu\nu} - \partial_\mu\zeta_\nu - \partial_\nu\zeta_\mu \quad (2.41)$$

Multiplying both sides by $\eta^{\mu\nu}$, we get

$$h' = h - 2\partial^\alpha\zeta_\alpha \quad (2.42)$$

Using the fact that $\Phi' = \Phi$, $\bar{h}'_{\mu\nu}$ can be written as

$$\bar{h}'_{\mu\nu} = h'_{\mu\nu} - \frac{1}{2}\eta_{\mu\nu}h' + \eta_{\mu\nu}\Phi' \quad (2.43)$$

$$\bar{h}'_{\mu\nu} = (h_{\mu\nu} - \frac{1}{2}\eta_{\mu\nu}h + \eta_{\mu\nu}\Phi) - (\partial_\mu\zeta_\nu + \partial_\nu\zeta_\mu) + \eta_{\mu\nu}\partial^\alpha\zeta_\alpha \quad (2.44)$$

$$\bar{h}'_{\mu\nu} = \bar{h}_{\mu\nu} - (\partial_\mu\zeta_\nu + \partial_\nu\zeta_\mu) + \eta_{\mu\nu}\partial^\alpha\zeta_\alpha \quad (2.45)$$

By multiplying both sides of Eq. (2.45) by $\eta^{\mu\nu}$ and using the fact that $\eta^{\mu\nu}\eta_{\mu\nu} = 4$, we get

$$\bar{h}' = \bar{h} + 2\partial^\alpha\zeta_\alpha \quad (2.46)$$

In terms of $\bar{h}'_{\mu\nu}$, Eq. (2.40) can be written as

$$\square\bar{h}'_{\mu\nu} - \partial_\mu(\partial^\alpha\bar{h}'_{\alpha\nu}) + \partial_\nu(\partial^\alpha\bar{h}'_{\alpha\mu}) + \eta_{\mu\nu}\partial^\beta(\partial^\alpha\bar{h}'_{\alpha\beta}) = 0 \quad (2.47)$$

We impose an extra condition on ζ^μ to simplify the Eq. (2.47). To do so, consider the term $\partial^\mu\bar{h}'_{\mu\nu}$

$$\partial^\mu\bar{h}'_{\mu\nu} = \partial^\mu\bar{h}_{\mu\nu} - \partial^\mu(\partial_\mu\zeta_\nu + \partial_\nu\zeta_\mu) + \partial^\mu\eta_{\mu\nu}\partial^\alpha\zeta_\alpha \quad (2.48)$$

$$\partial^\mu\bar{h}'_{\mu\nu} = \partial^\mu\bar{h}_{\mu\nu} - \square\zeta_\nu \quad (2.49)$$

If we choose ζ^μ such that $\square\zeta_\nu = \partial^\mu\bar{h}_{\mu\nu}$, it will make $\partial^\mu\bar{h}'_{\mu\nu} = 0$ and then Eq. (2.47) can be written as

$$\square\bar{h}'_{\mu\nu} = 0 \quad (2.50)$$

The condition above is called the Lorentz gauge. Next we apply d'Alembert operator on both sides of the Eq. (2.45) and impose the rule that derivatives commute. This gives

$$\square \bar{h}'_{\mu\nu} = \square \bar{h}_{\mu\nu} - \partial_\mu \square \zeta_\nu + \partial_\nu \square \zeta_\mu + \eta_{\mu\nu} \partial^\alpha \square \zeta_\alpha \quad (2.51)$$

We can still choose $\square \zeta_\mu = 0$ and preserve the Lorentz gauge. This condition together with Eq. (2.50) tells us

$$\square \bar{h}'_{\mu\nu}(x) = \square \bar{h}_{\mu\nu}(x) = 0 \quad (2.52)$$

and $\square \bar{h}_{\mu\nu}(x) = 0$ can be expanded as

$$-\frac{1}{c^2} \frac{\partial^2 \bar{h}_{\mu\nu}}{\partial t^2} + \frac{\partial^2 \bar{h}_{\mu\nu}}{\partial x^2} + \frac{\partial^2 \bar{h}_{\mu\nu}}{\partial y^2} + \frac{\partial^2 \bar{h}_{\mu\nu}}{\partial z^2} = 0 \quad (2.53)$$

We also impose an additional freedom ($\partial_\mu \zeta^\mu = -\frac{1}{2} \bar{h} + \Phi$) in the choice of the Lorentz gauge on Eq. (2.46) and obtain

$$\bar{h} = 2\Phi \quad (2.54)$$

In Eqs. (2.53) and (2.54), we have omitted the prime (') and moved back to the unprimed frame. The Eq. (2.53) is a wave equation and its solution can be written in the form

$$\bar{h}_{\mu\nu} = A_{\mu\nu}(\vec{k}) e^{ik^\alpha x_\alpha} \quad (2.55)$$

Similarly, the solution of $\square \Phi = 0$ has the form

$$\Phi(x) = b(\vec{k}) e^{ik^\alpha x_\alpha} \quad (2.56)$$

where $A_{\mu\nu}$ and b are constant amplitudes.

The condition $\square \bar{h}_{\mu\nu} = 0$ gives

$$-k_\beta k^\beta A_{\mu\nu} e^{ik^\alpha x_\alpha} = 0 \quad (2.57)$$

which implies

$$k_\beta k^\beta = 0 \quad (2.58)$$

$$\eta^{\alpha\beta} k_\alpha k_\beta = 0 \quad (2.59)$$

In the similar way, the condition $\partial^\mu \bar{h}_{\mu\nu} = 0$ gives

$$k^\mu A_{\mu\nu} = 0 \quad (2.60)$$

The Eq. (2.60) is the transversality condition for the gravitational waves. It tells that the whole plane wave solution is perpendicular to k^μ

Using the fact the $\bar{h} = 2\Phi$ in Eq. (2.37), we get

$$h_{\mu\nu} = \bar{h}_{\mu\nu} \quad (2.61)$$

and this implies that $h_{\mu\nu}$ is also a plane transverse wave. This can be concluded from Eq. (2.55) and Eq. (2.60).

We can understand the wave behaviour by studying the term $e^{ik^\alpha x_\alpha}$. It can be further written as $e^{ik^\alpha x_\alpha} = \cos(k^\alpha x_\alpha) + i \sin(k^\alpha x_\alpha)$. The argument of sine and cosine functions can be expanded as

$$k_\alpha x^\alpha = k_0 x^0 + \sum_{i=1}^3 k^i x^i \quad (2.62)$$

$$x^0 = -ct \quad (2.63)$$

$$k_\alpha x^\alpha = -ck^0 t + \vec{k} \cdot \vec{x} \quad (2.64)$$

where $\vec{k} = (k^1, k^2, k^3)$ and $\vec{x} = (x^1, x^2, x^3)$. Let $ck^0 = \omega$, then

$$k_\alpha x^\alpha = -\omega t + \vec{k} \cdot \vec{x} \quad (2.65)$$

$$\bar{h}_{\mu\nu} = A_{\mu\nu} [\cos(\omega t - \vec{k} \cdot \vec{x}) - i \sin(\omega t - \vec{k} \cdot \vec{x})] \quad (2.66)$$

where ω is the angular frequency of the wave. The vector \vec{k} points in the direction of the wave propagation. The length of vector \vec{k} is $|\vec{k}|$ where

$$|\vec{k}| = \frac{2\pi}{\lambda} \quad (2.67)$$

and λ is the wavelength of the wave. Using Eq. (2.58), we can write

$$k^\beta k_\beta = -(k^0)^2 + (k^1)^2 + (k^2)^2 + (k^3)^2 = 0 \quad (2.68)$$

$$(k^1)^2 + (k^2)^2 + (k^3)^2 = (k^0)^2 \quad (2.69)$$

The left-hand side of the equation above is $|\vec{k}|^2$ and right-hand side is $(\frac{\omega}{c})^2$. This gives us

$$|\vec{k}|^2 = \left(\frac{\omega}{c}\right)^2 \quad (2.70)$$

or,

$$\omega = c|\vec{k}| \quad (2.71)$$

The Eq. (2.71) is known as the dispersion relation for a the wave.

For a wave propagating in the $+z$ direction, $k^1 = k^2 = 0$. In this case, Eq. (59) gives $k^3 = \frac{\omega}{c}$ and the four-vector k^μ becomes

$$k^\mu = \left(\frac{\omega}{c}, 0, 0, \frac{\omega}{c}\right) \quad (2.72)$$

We can expand Eq. (2.60) as

$$k^\mu A_{\mu\nu} = k^0 A_{0\nu} + k^1 A_{1\nu} + k^2 A_{2\nu} + k^3 A_{3\nu} = 0 \quad (2.73)$$

Since $k^1 = k^2 = 0$, we get

$$A_{0\nu} = -A_{3\nu} \quad (2.74)$$

The Eq. (2.74) can also be written as

$$A_{\nu 0} = -A_{\nu 3} \quad (2.75)$$

because $A_{\mu\nu} = A_{\nu\mu}$. With the help of above equation, the relation between some of the components can be expressed as

$$A_{00} = -A_{03} = -A_{30} = +A_{33} \quad (2.76)$$

$$A_{10} = -A_{13} \quad (2.77)$$

$$A_{20} = -A_{23} \quad (2.78)$$

We started with 10 components of the metric tensor. By applying the transversality condition, we have obtained equations Eq. (2.76), Eq. (2.77) and Eq. (2.78). These three equations reduce the components from 10 to 6.

The condition $\square \zeta^\mu = 0$ allows us to write ζ^μ as

$$\zeta_\mu(x) = \tilde{\zeta}_\mu(\vec{k}) e^{ik^\alpha x_\alpha} \quad (2.79)$$

and the condition $\partial_\mu \zeta^\mu = 0$ gives

$$\partial_\mu [\tilde{\zeta}^\mu(\vec{k}) e^{ik^\alpha x_\alpha}] = \tilde{\zeta}_\mu \frac{\partial [e^{ik^\alpha x_\alpha}]}{\partial x^\mu} = \tilde{\zeta}_\mu \times ik_\alpha \frac{\partial x^\alpha}{\partial x^\mu} [e^{ik^\alpha x_\alpha}] = i\tilde{\zeta}_\mu k^\mu [e^{ik^\alpha x_\alpha}] = 0 \quad (2.80)$$

which implies

$$k^\mu \tilde{\zeta}_\mu = 0 \quad (2.81)$$

Using the Eq. (2.45), Eq. (2.66) and Eq. (2.79), we can express $A'_{\mu\nu}$ in terms of $A_{\mu\nu}$. After some computation, we get

$$\bar{h}'_{\mu\nu} = [A_{\mu\nu} - i\tilde{\zeta}_\mu k_\nu - i\tilde{\zeta}_\nu k_\mu] e^{ik^\alpha x_\alpha} \quad (2.82)$$

or

$$\bar{h}'_{\mu\nu} = A'_{\mu\nu} e^{ik^\alpha x_\alpha} \quad (2.83)$$

where

$$A'_{\mu\nu} = A_{\mu\nu} - i\tilde{\zeta}_\mu k_\nu - i\tilde{\zeta}_\nu k_\mu \quad (2.84)$$

We can compute the components of metric tensor using the above equation.

$$A'_{00} = A_{00} - i\tilde{\zeta}_0 k_0 - i\tilde{\zeta}_0 k_0 \quad (2.85)$$

or

$$A'_{00} = A_{00} - 2i\tilde{\zeta}_0 k_0 \quad (2.86)$$

We have already computed that $k^\mu = (k, 0, 0, k)$ where $k = \frac{\omega}{c}$. By lowering the index, we get $k_\mu = (-k, 0, 0, k)$. This gives us

$$A'_{00} = A_{00} + 2i\tilde{\zeta}_0 k \quad (2.87)$$

$$A'_{11} = A_{11} - 2i\tilde{\zeta}_1 k_1 = A_{11} \quad (2.88)$$

and

$$A'_{22} = A_{22} - 2i\tilde{\zeta}_2 k_2 = A_{22} \quad (2.89)$$

because $k_1 = k_2 = 0$. For the same reason

$$A'_{21} = A_{21} \quad (2.90)$$

In the same way, we can find

$$A'_{31} = A_{31} - i\tilde{\zeta}_1 k \quad (2.91)$$

$$A'_{32} = A_{32} - i\tilde{\zeta}_2 k \quad (2.92)$$

We can choose $\tilde{\zeta}_0$, $\tilde{\zeta}_1$ and $\tilde{\zeta}_2$ such that $A'_{00} = 0$, $A'_{31} = 0$ and $A'_{32} = 0$. Using the fact that $h = 2\Phi$, we can write

$$h = h_{00} + h_{11} + h_{22} + h_{33} = h_{11} + h_{22} = 2\Phi \quad (2.93)$$

We have ignored h_{00} and h_{33} in Eq. (2.93) because

$$h_{\mu\nu} = \bar{h}_{\mu\nu} = A_{\mu\nu} e^{ik^\alpha x_\alpha} \quad (2.94)$$

and we have already set $A_{00} = 0$. Since $A_{33} = A_{00}$ [Eq. (2.76)], A_{33} is also equal to zero. This makes $h_{00} = 0$ and $h_{33} = 0$.

Now, we can summarize the metric $h_{\mu\nu}$.

1. The metric $h_{\mu\nu}$ has 16 components. Since it is a symmetric tensor, we are left only with 10 independent components. [$h_{12} = h_{21}$, $h_{13} = h_{31}$, $h_{23} = h_{32}$, $h_{10} = h_{01}$, $h_{02} = h_{20}$ and $h_{03} = h_{30}$] are 6 conditions.
2. The transversality condition $k^\mu A_{\mu\nu}$ reduces them from 10 to 4 as given in equations (2.76), (2.77) and (2.78).
3. We have chosen $\tilde{\zeta}_0$, $\tilde{\zeta}_1$ and $\tilde{\zeta}_2$ such that they vanish the components A_{00} , A_{31} and A_{32} . This gauge condition reduces the number of independent components from 6 to 3.
4. Now we have to compute only 3 components. They are h_{12} , h_{11} and Φ . They are called as three independent polarization states of gravitational waves. h_{12} is called the 'cross' polarization h_\times , h_{11} is called the 'plus' polarization h_+ and Φ is called the 'scalar' field polarization h_S .

The GW described using the above gauges has a very simple form as written below

$$h_{\mu\nu}(t) = \begin{bmatrix} 0 & 0 & 0 & 0 \\ 0 & h_{11} + \Phi & h_{12} & 0 \\ 0 & h_{21} & -h_{11} + \Phi & 0 \\ 0 & 0 & 0 & 0 \end{bmatrix} = \begin{bmatrix} 0 & 0 & 0 & 0 \\ 0 & h_+ + h_S & h_\times & 0 \\ 0 & h_\times & -h_+ + h_S & 0 \\ 0 & 0 & 0 & 0 \end{bmatrix} \quad (2.95)$$

or

$$h_{\mu\nu}(t, \vec{x}) = h_+(t, \vec{x}) e_{\mu\nu}^+ + h_\times(t, \vec{x}) e_{\mu\nu}^\times + h_S e_{\mu\nu}^S \quad (2.96)$$

where

$$e_{\mu\nu}^+ \equiv \begin{bmatrix} 0 & 0 & 0 & 0 \\ 0 & +1 & 0 & 0 \\ 0 & 0 & -1 & 0 \\ 0 & 0 & 0 & 0 \end{bmatrix} \quad (2.97)$$

$$e_{\mu\nu}^\times \equiv \begin{bmatrix} 0 & 0 & 0 & 0 \\ 0 & 0 & +1 & 0 \\ 0 & +1 & 0 & 0 \\ 0 & 0 & 0 & 0 \end{bmatrix} \quad (2.98)$$

$$e_{\mu\nu}^S \equiv \begin{bmatrix} 0 & 0 & 0 & 0 \\ 0 & +1 & 0 & 0 \\ 0 & 0 & +1 & 0 \\ 0 & 0 & 0 & 0 \end{bmatrix} \quad (2.99)$$

In the following, it will be convenient to use the parameter ζ instead of the parameter ω_{BD} :

$$\zeta \equiv \frac{1}{2\omega_{BD} + 4}. \quad (2.100)$$

To obtain approximate expressions for the two polarizations h_+ and h_\times we use the standard quadrupole formalism (see Chapter 1.7 of [46]). Assuming that the wave propagates in the $+z$ direction, we have the following formulae for h_+ and h_\times polarizations

$$\begin{aligned} h_+ &= \frac{G}{rc^4} (1 - \zeta) (\ddot{Q}_W^{xx}(t') - \ddot{Q}_W^{yy}(t')) \\ h_\times &= \frac{2G}{rc^4} (1 - \zeta) \ddot{Q}_W^{xy}(t') \end{aligned} \quad (2.101)$$

where G is the gravitational constant, c is the speed of light, t' is the retarded time, r is the distance of the source, \ddot{Q}_W^{ij} is the second time derivative of the mass quadrupole moment in the wave frame. In the limit $\omega_{BD} \rightarrow \infty$, i.e. $\zeta \rightarrow 0$ the above expressions for the two polarizations reduce to the expression in classical general relativity given by Eqs. (1.114) of [46].

The scalar polarization is derived in Chapter 13.5 of [23] and it is given by the following expression (see Eqs. (13.164) and (13.168a) in [23])

$$h_S = \frac{2G}{rc^2} \zeta \left[M(t') + \frac{1}{c} \dot{D}_W^z(t') - \frac{1}{2c^2} \ddot{Q}_W^{zz}(t') \right] \quad (2.102)$$

where \dot{D}_W^i is the first time derivative of the mass dipole moment in the wave frame and M is the mass monopole moment. In GR, there is no contribution from the mass monopole moment and dipole moment because of mass and linear momentum conservation. But monopole and dipole radiation appear in BD theory because the scalar field ϕ does not satisfy a conservation law. The response of these three polarizations on a ring of test particles is shown in the Figure 2.1.

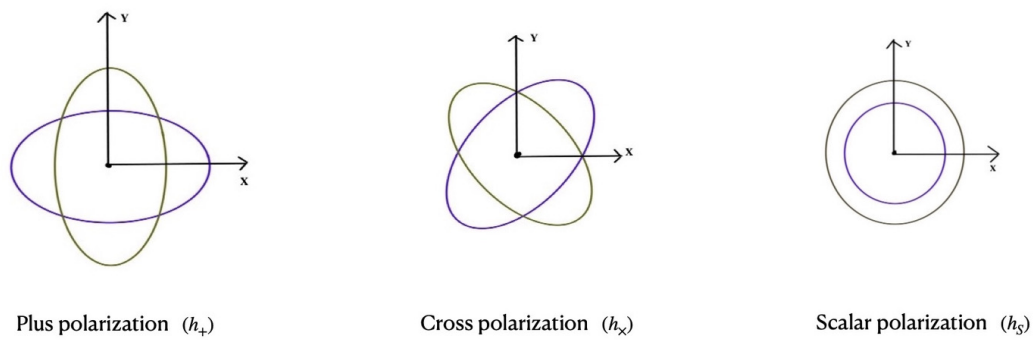


FIGURE 2.1: Effect of different polarizations in BD theory on a ring of test particles. In all the situations, GW travels in the z-direction.

Chapter 3

Neutron Stars in Brans-Dicke Theory

3.1 Rotating Neutron Star

3.1.1 Multipole moments

If the star is perfectly symmetric, both dipole and quadrupole moments vanish, and there is no gravitational radiation. However, a real neutron star is not perfectly symmetric because there may be some elastic deformations of its solid crust, which may be due to strong magnetic fields present in the neutron stars. We model the deformation as a mountain on a neutron star. This asymmetry leads both to quadrupolar and dipolar gravitational-wave emission

The multipole expansion $I^{<L>}$ in terms of symmetric trace-free (STF) tensors is given by [23]

$$I^{<L>} = \int \rho(\vec{x}) x^{<L>} d^3x \quad (3.1)$$

where $\vec{x} = (x, y, z)$ are Cartesian coordinates, ρ is the density of the star and d^3x is the volume element. $<L>$ denotes the STF tensor and L represents a collection of l individual indices. When $l = 1$ and $<L> = <i>$ we get

$$x^{<L>} = x^i \quad (3.2)$$

and when $l = 2$ and $<L> = <ij>$ we have

$$x^{<L>} = x^i x^j - \frac{1}{3} r^2 \delta^{ij} \quad (3.3)$$

where r^2 is equal to $x^2 + y^2 + z^2$ and δ_{ij} is the Kronecker delta function. Using the above relations, the i component of the dipole moment D_s^i in the star's frame is given by

$$D_s^i \equiv I^{<i>} = \int \rho x^i d^3x. \quad (3.4)$$

Similarly, the ij component of the quadrupole tensor Q_s^{ij} in the star's frame is calculated as

$$Q_s^{ij} \equiv I^{<ij>} = \int \rho [x^i x^j - \frac{1}{3} r^2 \delta_{ij}] d^3x \quad (3.5)$$

For simplicity, we consider the star to be a sphere of radius a , and we assume that the size of the mountain is minimal compared to the radius of the star. Consequently, we can model the mountain as a point mass. Moreover, we assume that the Cartesian coordinate of the mountain are $(a, 0, 0)$. Thus the mass density ρ of the mountain is

given by

$$\rho = m\delta(x-a)\delta(y)\delta(z) \quad (3.6)$$

where δ is the Dirac delta function and m is the mass of the mountain. Using the equations above, we can easily determine the components of the dipole and quadrupole moments for this model.

$$D_s = [ma, 0, 0] \quad (3.7)$$

and

$$Q_s = \begin{bmatrix} \frac{2}{3}ma^2 & 0 & 0 \\ 0 & -\frac{1}{3}ma^2 & 0 \\ 0 & 0 & -\frac{1}{3}ma^2 \end{bmatrix}. \quad (3.8)$$

Since our system is nearly spherical, it can also be expanded in terms of multipole moments I_{lm} given by

$$I_{lm} = \int \rho r^l Y_{lm}^*(\theta, \phi) d^3x \quad (3.9)$$

where (r, θ, ϕ) are usual spherical coordinates, $Y_{lm}^*(\theta, \phi)$ is the complex conjugate of spherical harmonics functions and $d^3x = r^2 \sin\theta dr d\theta d\phi$. The density of the mountain in spherical coordinates can be written as

$$\rho = m \frac{\delta(r-a)\delta(\theta-\frac{\pi}{2})\delta(\phi)}{r^2 \sin\theta}. \quad (3.10)$$

For the quadrupolar emission the most dominant moment is I_{22} and for the case of our model it can be simplified as

$$I_{22} = \sqrt{\frac{15}{32\pi}} ma^2. \quad (3.11)$$

3.1.2 Gravitational wave signal from a rotating neutron star

To obtain the explicit equations for the polarization function h_+ , h_\times , and h_s , we first transform the dipole vector D_s and quadrupole matrix Q_s from the source to wave frame. Following the construction in Chapter 2.5 of [46], we have

$$D_W(t) = S \cdot R(t) \cdot D_s \quad (3.12)$$

and

$$Q_W(t) = S \cdot R(t) \cdot Q_s \cdot R(t)^T \cdot S^T \quad (3.13)$$

where R is the transformation matrix from the source frame to an inertial frame, and S is the transformation matrix from the inertial frame to the wave frame as shown in Figure 3.1. The matrix R is given by

$$R(t) = \begin{bmatrix} \cos\phi_s(t) & -\sin\phi_s(t) & 0 \\ \sin\phi_s(t) & \cos\phi_s(t) & 0 \\ 0 & 0 & 1 \end{bmatrix} \quad (3.14)$$

where $\phi_s(t)$ is the instantaneous rotational phase of the star. The matrix S has the form

$$S = \begin{bmatrix} \cos \iota & 0 & -\sin \iota \\ 0 & 1 & 0 \\ \sin \iota & 0 & \cos \iota \end{bmatrix} \quad (3.15)$$

where ι is the angle between the angular momentum vector of the rotating neutron star and the direction along which the wave travels. We assume that the rotational phase $\phi_s(t)$ is slowly varying, and it can be modelled by Taylor expansion as

$$\phi_s(t) = \phi_o + 2\pi \sum_{k=0}^s f_0^{(k)} \frac{t^{k+1}}{(k+1)!} \quad (3.16)$$

where ϕ_o is a constant phase offset, $f_0^{(k)}$ is the k th time derivative of the instantaneous frequency evaluated at $t = 0$ and s is the number of spin-down parameters.

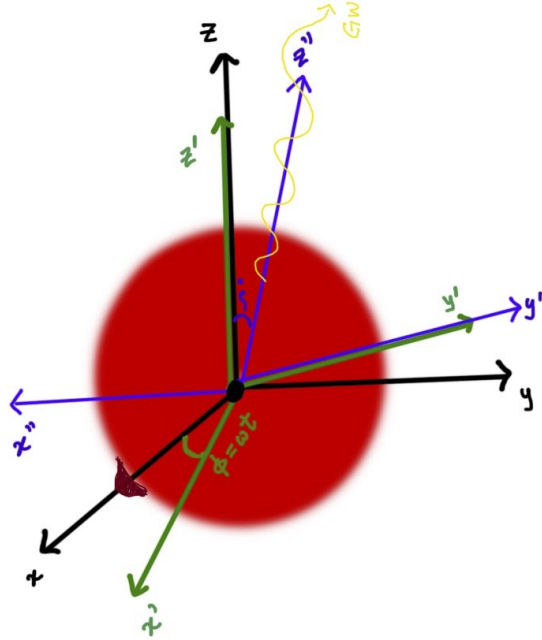


FIGURE 3.1

Using Eqs. (A.40) and neglecting the second order time derivatives of the phase $\phi(t)$, we obtain the following expressions for the two tensor polarizations

$$h_+(t) = h_o \frac{1 + \cos^2 \iota}{2} \cos 2\phi_s(t) \quad (3.17)$$

$$h_\times(t) = h_o \cos \iota \sin 2\phi_s(t) \quad (3.18)$$

where h_o is the constant amplitude given by

$$h_o = \frac{16\pi^2 G}{c^4} (1 - \zeta) Q \frac{f_0^2}{r} \quad (3.19)$$

where ζ is the BD parameter as defined in Eq. (2.100) and quadrupole parameter Q is given by

$$Q = Q_s^{xx} - Q_s^{yy} \quad (3.20)$$

and f_0 is the spin frequency of the star. We notice that when $\zeta \rightarrow 0$, the expressions for h_+ and h_\times reduce to the polarizations in classical general relativity.

To calculate the scalar polarization, we make a simplifying assumption that the only non-vanishing component of the dipole moment in the star's frame is in the x-direction like in the simple mountain model in Section 3.1.2, i.e. we have

$$D_s = (D, 0, 0). \quad (3.21)$$

With this assumption, we obtain the following formula for the scalar polarization, neglecting the mass monopole's contribution (see [23]). The scalar polarization has contributions both from the dipole and quadrupole parts.

$$h_s(t) = -h_0^d \sin \iota \sin \phi_s(t) + h_0^q \frac{\sin^2 \iota}{2} \cos 2\phi_s(t). \quad (3.22)$$

where constant amplitudes h_0^d and h_0^q are given by

$$h_0^d = \frac{4\pi G}{c^3} \zeta D \frac{f_0}{r}, \quad (3.23)$$

$$h_0^q = \frac{16\pi^2 G}{c^4} \zeta Q \frac{f_0^2}{r}. \quad (3.24)$$

We see that the quadrupole part of the radiation gives in a signal at twice the spin frequency of the star whereas dipole radiation results in a signal at once the spin frequency.

In this box, we briefly explain the absence of the dipole radiation in GR. First, let us consider an isolated system with only two point masses m_1 and m_2 as shown in Figure 3.2. The dipole moment, in this case, is given by

$$\vec{d} = m_1 \vec{r}_1 + m_2 \vec{r}_2 = \frac{m_1 \vec{r}_1 + m_2 \vec{r}_2}{M} M \quad (3.25)$$

where $M \equiv m_1 + m_2$. This simplifies to

$$\vec{d} = M \vec{r}_{com} \quad (3.26)$$

where \vec{r}_{com} is the position vector of the centre of mass (COM) of the system. The power P emitted in the gravitational dipole radiation is

$$P = \frac{2G}{3c^3} \langle |\ddot{\vec{d}}|^2 \rangle \quad (3.27)$$

where $\langle \cdot \rangle$ implies the time average. Using Eq. (3.26) and Eq. (3.27), we get

$$P = \frac{2GM^2}{3c^3} \langle |\ddot{\vec{r}}_{com}|^2 \rangle \quad (3.28)$$

But for an isolated system, the acceleration of the COM is zero, and hence there is no gravitational dipole radiation in GR. In reality, no system is perfectly isolated unless we take the entire universe as our system.

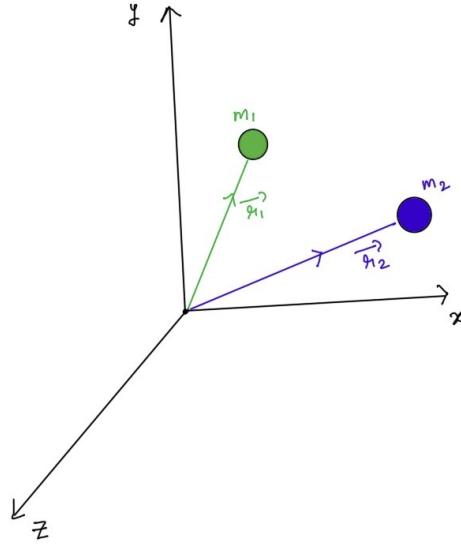


FIGURE 3.2: Two point masses m_1 and m_2 moving under the gravitational field of each other.

3.1.3 Response of the interferometric detector to a gravitational-wave signal from a rotating neutron star

To derive the detector's response function to gravitational-wave signal from a rotating neutron star, we follow the formalism presented in Section II of [47]. We obtain the response separately for the tensor and the scalar polarization. Thus we divide the three-dimensional matrix $H(t)$ of the spatial metric perturbation produced in the wave frame into tensor part $H_T(t)$ and the scalar part $H_S(t)$ defined by

$$H_T(t) = \begin{bmatrix} h_+(t) & h_\times(t) & 0 \\ h_\times(t) & -h_+(t) & 0 \\ 0 & 0 & 0 \end{bmatrix} \quad (3.29)$$

and

$$H_S(t) = \begin{bmatrix} h_S(t) & 0 & 0 \\ 0 & h_S(t) & 0 \\ 0 & 0 & 0 \end{bmatrix}. \quad (3.30)$$

Then the response function h_T^{BD} to the tensor polarization and the response function h_S^{BD} to the scalar polarization are given by

$$h_T^{BD}(t) = \frac{1}{2} \mathbf{n}_1 \cdot [\tilde{H}_T(t) \mathbf{n}_1] - \frac{1}{2} \mathbf{n}_2 \cdot [\tilde{H}_T(t) \mathbf{n}_2] \quad (3.31)$$

and

$$h_S^{BD}(t) = \frac{1}{2} \mathbf{n}_1 \cdot [\tilde{H}_S(t) \mathbf{n}_1] - \frac{1}{2} \mathbf{n}_2 \cdot [\tilde{H}_S(t) \mathbf{n}_2]. \quad (3.32)$$

In the above expressions, \mathbf{n}_1 and \mathbf{n}_2 denote the unit vectors parallel to the arm number 1 and 2 respectively. $\mathbf{n}_1 \times \mathbf{n}_2$ points outwards from the surface of the Earth. The responses are defined as the difference between the wave-induced relative length changes of the two interferometer arms. We assume that the detector arms are orthogonal and choose the x -axis to be along the first interferometer arm and the y -axis to be along the second arm. Hence we have

$$\mathbf{n}_1 = (1, 0, 0), \quad \mathbf{n}_2 = (0, 1, 0). \quad (3.33)$$

The matrices $\tilde{H}_T(t)$ and $\tilde{H}_S(t)$ are tensorial and scalar matrices respectively of the spatial metric perturbation produced by the wave in the proper reference frame of the detector. They are related to matrices in the wave frame by the following transformations

$$\tilde{H}_T(t) = M(t)H_T(t)M(t)^T \quad (3.34)$$

and

$$\tilde{H}_S(t) = M(t)H_S(t)M(t)^T. \quad (3.35)$$

The matrix M is a three-dimensional orthogonal matrix that transforms from the wave Cartesian coordinates in the wave frame to the Cartesian coordinates in the detector's proper reference frame. We have assumed that the wave travels in the $+z$ -direction. The matrix M can be expressed as

$$M = M_3 M_2 M_1^T. \quad (3.36)$$

M_1 is the matrix of transformation from wave to celestial sphere frame coordinates given by

$$M_1 = \begin{bmatrix} \sin \alpha \cos \psi - \cos \alpha \sin \delta \sin \psi & -\cos \alpha \cos \psi - \sin \alpha \sin \delta \sin \psi & \cos \delta \sin \psi \\ -\sin \alpha \sin \psi - \cos \alpha \sin \delta \cos \psi & \cos \alpha \sin \psi - \sin \alpha \sin \delta \cos \psi & \cos \delta \cos \psi \\ -\cos \alpha \cos \delta & -\sin \alpha \cos \delta & -\sin \delta \end{bmatrix} \quad (3.37)$$

where δ is the declination of the gravitational-wave source, α is its right ascension and ψ is the polarization angle. M_2 is the matrix of transformation from celestial coordinates to cardinal coordinates

$$M_2 = \begin{bmatrix} \sin \lambda \cos(\phi_r + \Omega_r t) & \sin \lambda \sin(\phi_r + \Omega_r t) & -\cos \lambda \\ -\sin(\phi_r + \Omega_r t) & \cos(\phi_r + \Omega_r t) & 0 \\ \cos \lambda \cos(\phi_r + \Omega_r t) & \cos \lambda \sin(\phi_r + \Omega_r t) & \sin \lambda \end{bmatrix} \quad (3.38)$$

where λ is the latitude of the detector's site, Ω_r is the rotational angular velocity of the Earth, ϕ_r is the deterministic phase which defines the position of the Earth in its diurnal motion at time $t = 0$. $(\phi_r + \Omega_r t)$ coincides with the local sidereal time of the detector's site. M_3 is the matrix of transformation from cardinal coordinates to detector proper reference frame coordinates.

$$M_3 = \begin{bmatrix} -\sin(\gamma + \frac{\pi}{4}) & \cos(\gamma + \frac{\pi}{4}) & 0 \\ -\cos(\gamma + \frac{\pi}{4}) & -\sin(\gamma + \frac{\pi}{4}) & 0 \\ 0 & 0 & 1 \end{bmatrix} \quad (3.39)$$

where the angle γ determines the orientation of the detector's arms with respect to local geographical directions.

Tensor response. The tensor response has exactly the same form as the response of the detector in classical general relativity except for the factor $1 - \zeta$ in the constant amplitude h_o (see Eq. (3.19)). The detailed derivation is given in Section II of [47]. Here we only summarize the basic formulae. The tensor response can be expressed as a linear combination of four time-dependent functions $h_i(t)$.

$$h_T^{\text{BD}}(t) = \sum_{i=1}^4 A_i h_i(t) \quad (3.40)$$

where A_i are four constant amplitudes given by

$$A_1 = h_o \left[\frac{1}{2} (1 + \cos^2 \iota) \cos 2\psi \cos 2\phi_o - \cos \iota \sin 2\psi \sin 2\phi_o \right] \quad (3.41)$$

$$A_2 = h_o \left[\frac{1}{2} (1 + \cos^2 \iota) \sin 2\psi \cos 2\phi_o + \cos \iota \cos 2\psi \sin 2\phi_o \right] \quad (3.42)$$

$$A_3 = h_o \left[-\frac{1}{2} (1 + \cos^2 \iota) \cos 2\psi \sin 2\phi_o - \cos \iota \sin 2\psi \cos 2\phi_o \right] \quad (3.43)$$

$$A_4 = h_o \left[-\frac{1}{2} (1 + \cos^2 \iota) \sin 2\psi \sin 2\phi_o + \cos \iota \cos 2\psi \cos 2\phi_o \right]. \quad (3.44)$$

where ϕ_o is the constant phase offset. The four time dependent functions $h_i(t)$ have the form

$$h_1 = a(t) \cos 2\phi(t) \quad (3.45)$$

$$h_2 = b(t) \cos 2\phi(t) \quad (3.46)$$

$$h_3 = a(t) \sin 2\phi(t) \quad (3.47)$$

$$h_4 = b(t) \sin 2\phi(t). \quad (3.48)$$

The expressions for two amplitude modulation functions $a(t)$ and $b(t)$ read.

$$\begin{aligned} a(t) = & \frac{1}{16} \sin 2\gamma (3 - \cos 2\lambda) (3 - \cos 2\delta) \cos[2(\alpha - \phi_r - \Omega_r t)] \\ & - \frac{1}{4} \cos 2\gamma \sin \lambda (3 - \cos 2\delta) \sin[2(\alpha - \phi_r - \Omega_r t)] \\ & + \frac{1}{4} \sin 2\gamma \sin 2\lambda \sin 2\delta \cos[\alpha - \phi_r - \Omega_r t] - \frac{1}{2} \cos 2\gamma \cos \lambda \sin 2\delta \sin[\alpha - \phi_r - \Omega_r t] \\ & + \frac{3}{4} \sin 2\gamma \cos^2 \lambda \cos^2 \delta, \end{aligned} \quad (3.49)$$

$$\begin{aligned} b(t) = & \cos 2\gamma \sin \lambda \sin \delta \cos[2(\alpha - \phi_r - \Omega_r t)] + \frac{1}{4} \sin 2\gamma (3 - \cos 2\lambda) \sin \delta \sin[2(\alpha - \phi_r - \Omega_r t)] \\ & + \cos 2\gamma \cos \lambda \cos \delta \cos[\alpha - \phi_r - \Omega_r t] + \frac{1}{2} \sin 2\gamma \sin 2\lambda \cos \delta \sin[\alpha - \phi_r - \Omega_r t]. \end{aligned} \quad (3.50)$$

The phase $\phi(t)$ of the signal in the detector's frame is approximately given by

$$\phi(t) = 2\pi \sum_{k=0}^s f_0^{(k)} \frac{t^{k+1}}{(k+1)!} + \frac{2\pi}{c} \mathbf{n}_0 \cdot \mathbf{r}_d(t) \sum_{k=0}^s f_0^{(k)} \frac{t^k}{k!} \quad (3.51)$$

where \mathbf{n}_0 is the constant unit vector in the direction of the star in the **SSB** reference frame

$$\mathbf{n}_0 = \begin{bmatrix} \cos \alpha \cos \delta \\ \sin \alpha \cos \delta \\ \sin \delta \end{bmatrix} \quad (3.52)$$

and \mathbf{r}_d is the position vector of the detector in that frame. The approximation that led to Eq. (3.51) above are discussed in detail in Sec. IIB and Appendix A of [47].

Scalar response We obtain the formula for the response of a detector to the scalar polarization by plugging in matrices M_1 , M_2 , and M_3 given by Eqs. (3.37), (3.38), and (3.39) into the Eq. (3.32). An extensive algebraic manipulations yields

$$h_S^{BD}(t) = c(t)h_S \quad (3.53)$$

where $c(t)$ is the amplitude modulation function given by

$$\begin{aligned} c(t) = & \frac{1}{8} [(-1 + 3 \cos 2\delta) \cos^2 \lambda \sin 2\gamma + 2 \cos(\alpha - \phi_r - t\Omega_r) \sin 2\gamma \sin 2\delta \sin 2\lambda] \\ & + \frac{1}{8} \cos^2 \delta [(-3 + \cos 2\lambda) \cos[2(-\alpha + \phi_r + t\Omega_r)] \sin 2\gamma + 4 \cos 2\gamma \sin \lambda \sin[2(\alpha - \phi_r + t\Omega_r)]] \\ & - \frac{1}{2} \cos 2\gamma \cos \lambda \sin 2\delta \sin(\alpha - \phi_r - t\Omega_r). \end{aligned} \quad (3.54)$$

The scalar polarization can be written as a linear combination of four time dependent functions $h_{iS}(t)$

$$h_S^{BD}(t) = \sum_{i=1}^4 A_{iS} h_{iS}(t) \quad (3.55)$$

where the four constant amplitudes A_{iS} are given by

$$A_{1S} = -h_0^d \sin \iota \sin \phi_0 \quad (3.56)$$

$$A_{2S} = -h_0^d \sin \iota \cos \phi_0 \quad (3.57)$$

$$A_{3S} = h_0^q \sin^2 \iota \cos 2\phi_0 \quad (3.58)$$

$$A_{4S} = -h_0^q \sin^2 \iota \sin 2\phi_0. \quad (3.59)$$

The amplitudes h_0^d and h_0^q are given by Eqs. (3.23) and (3.24) respectively. The time dependent functions $h_{iS}(t)$ have the form

$$h_{1S}(t) = c(t) \cos \phi(t) \quad (3.60)$$

$$h_{2S}(t) = c(t) \sin \phi(t) \quad (3.61)$$

$$h_{3S}(t) = c(t) \cos 2\phi(t) \quad (3.62)$$

$$h_{4S}(t) = c(t) \sin 2\phi(t). \quad (3.63)$$

We see that the scalar part of the response has contributions both from the dipole and quadrupole radiation. The functions $h_{1S}(t)$ and $h_{2S}(t)$ determine the response corresponding to the dipole contribution, whereas $h_{3S}(t)$ and $h_{4S}(t)$ define the quadrupole contribution.

It is helpful to rewrite the above equations as a correction to the GR part. To do so, first, we rewrite constant amplitudes for tensor polarizations as

$$A_1 = h_o^{\text{GR}} \left[\frac{1}{2}(1 + \cos^2 \iota) \cos 2\psi \cos 2\phi_o - \cos \iota \sin 2\psi \sin 2\phi_o \right] - \zeta h_o^{\text{GR}} \left[\frac{1}{2}(1 + \cos^2 \iota) \cos 2\psi \cos 2\phi_o - \cos \iota \sin 2\psi \sin 2\phi_o \right] \quad (3.64)$$

$$A_2 = h_o^{\text{GR}} \left[\frac{1}{2}(1 + \cos^2 \iota) \sin 2\psi \cos 2\phi_o + \cos \iota \cos 2\psi \sin 2\phi_o \right] - \zeta h_o^{\text{GR}} \left[\frac{1}{2}(1 + \cos^2 \iota) \sin 2\psi \cos 2\phi_o + \cos \iota \cos 2\psi \sin 2\phi_o \right] \quad (3.65)$$

$$A_3 = h_o^{\text{GR}} \left[-\frac{1}{2}(1 + \cos^2 \iota) \cos 2\psi \sin 2\phi_o - \cos \iota \sin 2\psi \cos 2\phi_o \right] - \zeta h_o^{\text{GR}} \left[-\frac{1}{2}(1 + \cos^2 \iota) \cos 2\psi \sin 2\phi_o - \cos \iota \sin 2\psi \cos 2\phi_o \right] \quad (3.66)$$

$$A_4 = h_o^{\text{GR}} \left[-\frac{1}{2}(1 + \cos^2 \iota) \sin 2\psi \sin 2\phi_o + \cos \iota \cos 2\psi \cos 2\phi_o \right] - \zeta h_o^{\text{GR}} \left[-\frac{1}{2}(1 + \cos^2 \iota) \sin 2\psi \sin 2\phi_o + \cos \iota \cos 2\psi \cos 2\phi_o \right] \quad (3.67)$$

where

$$h_o^{\text{GR}} \equiv \frac{16\pi^2 G}{c^4} Q \frac{f_0^2}{r} \quad (3.68)$$

The combined tensor and scalar response can be written as

$$h(t) = h_T^{\text{BD}}(t) + h_S^{\text{BD}}(t) \quad (3.69)$$

which can be simplified to

$$h(t) = h_T^{\text{GR}}(t) - \zeta h_T^{\text{GR}}(t) + h_S^{\text{BD}}(t) \quad (3.70)$$

We notice that the last two terms in Eq. (3.70) are corrections to the GR.

It is also advantageous to express the constant amplitude functions in terms of numerical astrophysical values.

$$h_o = 4.22 \times 10^{-25} \left(1 - \frac{\zeta}{10^{-3}}\right) \left(\frac{1\text{kpc}}{r}\right) \left(\frac{f_0}{100\text{Hz}}\right)^2 \left(\frac{Q}{10^{33} \text{kg m}^2}\right) \quad (3.71)$$

$$h_o^d = 1.01 \times 10^{-26} \left(\frac{\zeta}{10^{-3}}\right) \left(\frac{1\text{kpc}}{r}\right) \left(\frac{f_0}{100\text{Hz}}\right) \left(\frac{D}{10^{29} \text{kg m}}\right) \quad (3.72)$$

$$h_o^q = 4.22 \times 10^{-28} \left(\frac{\zeta}{10^{-3}}\right) \left(\frac{1\text{kpc}}{r}\right) \left(\frac{f_0}{100\text{Hz}}\right)^2 \left(\frac{Q}{10^{33} \text{kg m}^2}\right) \quad (3.73)$$

Often an asymmetric rotating neutron star is modeled as an ellipsoid rotating about its principal axis. In the model, the quadrupole coefficient Q in Eqs. (3.71) and (3.73) is given by

$$Q = I_{zz} \epsilon \quad (3.74)$$

I_{zz} is the moment of inertia of the neutron star about the z -axis, and ϵ is the ellipticity defined as

$$\epsilon \equiv \frac{|I_{xx} - I_{yy}|}{I_{zz}} \quad (3.75)$$

where I_{xx} and I_{yy} are the moments of inertia about the x and the y axis respectively. In terms of fiducial astrophysical values, Q can be expressed as

$$Q = 10^{33} \text{kg m}^2 \left(\frac{I_{zz}}{10^{38} \text{kg m}^2} \right) \left(\frac{\varepsilon}{10^{-5}} \right). \quad (3.76)$$

3.2 Detection statistic and parameter estimation

To obtain the detection statistic for the signal derived in the previous section, we use the maximum likelihood method described in Chapter 6 of [46]. We assume that the noise $n(t)$ in the detector is an additive and zero-mean Gaussian process. Thus when the signal $s(t)$ is present, the data can be written as

$$x(t) = n(t) + s(t). \quad (3.77)$$

For the Gaussian case, the log-likelihood function is given by

$$\ln \Lambda = (x|s) - \frac{1}{2}(s|s). \quad (3.78)$$

where for the case of white noise with one-sided spectral density S_o , the scalar product $(\cdot|\cdot)$ is defined as

$$(x|y) \equiv \frac{2}{S_o} \int_0^{T_0} x(t)y(t)dt. \quad (3.79)$$

Our signal is represented by a linear combination of time-dependent functions $h_l(t)$.

$$s(t) = A_1 h_1(t) + A_2 h_2(t) + A_3 h_3(t) + A_4 h_4(t) + A_{3S} h_{3S}(t) + A_{4S} h_{4S}(t) + A_{1S} h_{1S}(t) + A_{2S} h_{2S}(t), \quad (3.80)$$

where the eight amplitudes depend on the six parameters $h_0, h_0^d, h_0^q, \psi, \iota$ and ϕ_0 . The first six terms in the signal (3.80) originate from the quadrupolar radiation, whereas the last two are the dipolar contribution.

The signal $s(t)$ can be expressed in the following compact form

$$s(t) = \sum_{l=1}^8 A_l h_l(t) = A^T \cdot h, \quad (3.81)$$

where A^T is the transpose of A and \cdot denotes matrix multiplication. A is a vector of constant amplitudes and h represents a vector of time-dependent functions $h_l(t)$ given by.

$$A = \begin{bmatrix} A_1 \\ \cdot \\ \cdot \\ \cdot \\ \cdot \\ A_8 \end{bmatrix} \quad \text{and} \quad h = \begin{bmatrix} h_1(t) \\ \cdot \\ \cdot \\ \cdot \\ \cdot \\ h_8(t) \end{bmatrix} \quad (3.82)$$

By substituting Eq. (3.81) into the likelihood function (3.78), we get

$$\ln \Lambda = A^T \cdot N - \frac{1}{2} A^T \cdot M \cdot A, \quad (3.83)$$

where N is a vector with components

$$N_l \equiv (x|h_l), \quad l = 1, \dots, 8 \quad (3.84)$$

and M is a matrix with components of the amplitudes A_i

$$M_{ij} \equiv (h_i|h_j), \quad i, j = 1, \dots, 8. \quad (3.85)$$

The maximum likelihood estimators of the amplitudes A_i are found by maximizing the Eq. (3.83) with respect to amplitudes

$$\frac{\partial \ln \Lambda}{\partial A_i} = N - A \cdot M = 0 \quad (3.86)$$

and this results in the following explicit formulae for maximum likelihood estimators \hat{A}_i of amplitudes A_i

$$\hat{A} = M^{-1} \cdot N \quad (3.87)$$

By substituting these estimators back in Eq. (3.83), we obtain the \mathcal{L} -statistic. The final result is

$$\mathcal{L} = \frac{1}{2} N^T \cdot M^{-1} \cdot N. \quad (3.88)$$

Two fundamental quantities for the data analysis method presented in this paper are the signal-to-noise ratio ρ and the Fisher matrix Γ . The signal-to-noise ratio is defined as

$$\rho = \sqrt{(s|s)} \quad (3.89)$$

and for the signal (3.81) it is given by

$$\rho = \sqrt{A^T \cdot M \cdot A}. \quad (3.90)$$

The Fisher matrix for the case of Gaussian noise is defined by

$$\Gamma_{A_l A_{l'}} = \left(\frac{\partial s}{\partial A_l} \middle| \frac{\partial s}{\partial A_{l'}} \right), \quad l, l' \in [1, 8]. \quad (3.91)$$

and for the case of signal (3.81), we simply have

$$\Gamma(A) = M. \quad (3.92)$$

For the case of Gaussian noise, the signal-to-noise ratio determines the probability of detection of the signal. For a large signal-to-noise ratio, the inverse of the Fisher matrix approximates the covariance matrix of the estimators of the parameters. For the case of signal (3.81), which is a linear function of the amplitude parameters, one can show that the maximum likelihood estimators of the amplitudes given by Eq. (3.87) are unbiased, and their covariance matrix is precisely equal to the inverse of the Fisher matrix.

We shall now obtain an explicit form of the \mathcal{L} -statistic for the case of the gravitational-wave signal from a rotating neutron star in BD theory. First, we need the matrix M given by Eq. (3.85). It can approximately be computed as

$$M = \left(\begin{array}{c|c} M_Q & \mathbf{0} \\ \hline \mathbf{0} & M_D \end{array} \right), \quad (3.93)$$

where

$$M_Q \approx \frac{1}{2} \begin{pmatrix} A & C & 0 & 0 & E & 0 \\ C & B & 0 & 0 & G & 0 \\ 0 & 0 & A & C & 0 & E \\ 0 & 0 & C & B & 0 & G \\ E & G & 0 & 0 & H & 0 \\ 0 & 0 & E & G & 0 & H \end{pmatrix} \quad (3.94)$$

and

$$M_D \approx \frac{1}{2} \begin{pmatrix} H & 0 \\ 0 & H \end{pmatrix}. \quad (3.95)$$

$A \equiv (a|a)$, $B \equiv (b|b)$, $C \equiv (a|b)$, $E \equiv (a|c)$, $G \equiv (b|c)$ and $H \equiv (c|c)$. To obtain the above approximation, we assume that the phase $\phi(t)$ has many oscillations over the observation time T_0 . Consequently, we have $\int_0^{T_0} \sin \phi(t) dt \approx 0$ and $\int_0^{T_0} \cos \phi(t) dt \approx 0$.

Similarly, we can split the column vector N into a quadrupolar part as well as a dipolar part and write it as

$$N = \begin{bmatrix} N_Q \\ N_D \end{bmatrix}, \quad (3.96)$$

where

$$N_Q = \begin{bmatrix} (x|h_1) \\ (x|h_2) \\ (x|h_3) \\ (x|h_4) \\ (x|h_{3S}) \\ (x|h_{4S}) \end{bmatrix}, \quad (3.97)$$

and

$$N_D = \begin{bmatrix} (x|h_{1S}) \\ (x|h_{2S}) \end{bmatrix}. \quad (3.98)$$

Consequently the likelihood ratio statistic \mathcal{L} can be expressed as a sum of the two statistics \mathcal{F}_Q^{BD} and \mathcal{F}_D^{BD} for the quadrupole and dipole part of the signal respectively.

$$\mathcal{L} = \mathcal{F}_Q^{BD} + \mathcal{F}_D^{BD} \quad (3.99)$$

where

$$\mathcal{F}_Q^{BD} = \frac{1}{2} N_Q^T M_{11}^{-1} N_Q \quad (3.100)$$

and

$$\mathcal{F}_D^{BD} = \frac{1}{2} N_D^T M_{22}^{-1} N_D. \quad (3.101)$$

The explicit expressions for \mathcal{F}_Q^{BD} and \mathcal{F}_D^{BD} are given by

$$\begin{aligned} \mathcal{F}_Q^{BD} = & \frac{(G^2 - BH)[(x|h_1)^2 + (x|h_3)^2] + (E^2 - AH)[(x|h_2)^2 + (x|h_4)^2] - AB[(x|h_{3S})^2 + (x|h_{4S})^2]}{2U} \\ & + \frac{2[CH - GE](x|h_1)(x|h_2) + 2CH(x|h_3)(x|h_4)}{2U} \\ & + \frac{2[(GA - CE)(x|h_2) + (BE - GE)(x|h_1)](x|h_{3S})}{2U} \\ & + \frac{2[(GA - CE)(x|h_4) + (BE - GC)(x|h_3)](x|h_{4S})}{2U} \end{aligned} \quad (3.102)$$

where

$$U = E^2B - 2CEG + C^2H + AG^2 - ABH \quad (3.103)$$

and

$$\mathcal{F}_D^{BD} = \frac{(x|h_{1S})^2 + (x|h_{2S})^2}{H} \quad (3.104)$$

From Eq. (3.87) the amplitude estimators take the following explicit form

$$\hat{A}_1 = 2 \frac{(x|h_1)(G^2 - BH) + (x|h_2)(CH - GE) + (x|h_{3S})(EB - GC)}{U}, \quad (3.105)$$

$$\hat{A}_2 = 2 \frac{(x|h_1)(CH - EG) + (x|h_2)(E^2 - AH) + (x|h_{3S})(AG - EC)}{U}, \quad (3.106)$$

$$\hat{A}_3 = 2 \frac{(x|h_3)(G^2 - BH) + (x|h_4)(CH - GE) + (x|h_{4S})(EB - GC)}{U}, \quad (3.107)$$

$$\hat{A}_4 = 2 \frac{(x|h_3)(CH - EG) + (x|h_4)(E^2 - AH) + (x|h_{4S})(AG - EC)}{U}, \quad (3.108)$$

$$\hat{A}_{3S} = 2 \frac{(x|h_1)(EB - CG) + (x|h_2)(AG - CE) + (x|h_{3S})(C^2 - AB)}{U}, \quad (3.109)$$

$$\hat{A}_{4S} = 2 \frac{(x|h_3)(EB - CG) + (x|h_4)(AG - CE) + (x|h_{4S})(C^2 - AB)}{U}, \quad (3.110)$$

$$\hat{A}_{1S} = 2 \frac{(x|h_{1S})}{H}, \quad (3.111)$$

$$\hat{A}_{2S} = 2 \frac{(x|h_{2S})}{H}. \quad (3.112)$$

It should be noted that amplitude estimators ($\hat{A}_1, \hat{A}_2, \hat{A}_3, \hat{A}_4$) are related to the quadrupolar part in the tensor polarization, the estimators ($\hat{A}_{3S}, \hat{A}_{4S}$) correspond to the quadrupolar part in scalar polarization and ($\hat{A}_{1S}, \hat{A}_{2S}$) represent the dipole part in the scalar polarization. The quadrupole part has six amplitudes, four from tensor polarization and two from scalar polarization. On the other hand, the dipole part has only two amplitudes from the scalar polarization. The observations indicate that the ζ coefficient in the Brans-Dicke theory is small. Consequently, the quadrupole part from the scalar polarization is small compared to the quadrupole part from the tensor polarizations. Also, the amplitude h_0 is deviated from its GR counterpart by a factor of $(1 - \zeta)$ and to first approximation we can neglect parameter ζ in h_0 . Thus we can safely approximate the quadrupole radiation in BD theory by quadrupole radiation in ordinary GR. Thus the statistic \mathcal{L} in Eq. (3.99) can be approximated by

$$\mathcal{L} = \mathcal{F} + \mathcal{D}, \quad (3.113)$$

where \mathcal{F} is the statistic for the quadrupole signal in Einstein's GR and \mathcal{D} is the statistic for the dipole signal in BD theory. The \mathcal{F} -statistic is given by

$$\mathcal{F} = \frac{B [(x|h_1)^2 + (x|h_3)^2] + A [(x|h_2)^2 + (x|h_4)^2]}{V} - \frac{2C [(x|h_1)(x|h_2) + (x|h_3)(x|h_4)]}{V} \quad (3.114)$$

and corresponding amplitude estimators are

$$\hat{A}_1 = 2 \frac{B(x|h_1) - C(x|h_2)}{V}, \quad (3.115)$$

$$\hat{A}_2 = 2 \frac{A(x|h_2) - C(x|h_1)}{V}, \quad (3.116)$$

$$\hat{A}_3 = 2 \frac{B(x|h_3) - C(x|h_4)}{V}, \quad (3.117)$$

$$\hat{A}_4 = 2 \frac{A(x|h_4) - C(x|h_3)}{V} \quad (3.118)$$

where

$$V = AB - C^2. \quad (3.119)$$

The \mathcal{D} -statistic is equal to \mathcal{F}_D^{BD} given by Eq. (3.104). \mathcal{F} -statistic has been used extensively in searching GWs from known pulsars [48], [49], [50].

With the approximations above, we are left only with the six amplitude parameters $\mathcal{A} = (A_1, A_2, A_3, A_4, A_{1S}, A_{2S})$ which depend on five astrophysical parameters $\theta = (h_o, h_o^d, \psi, \iota, \phi_0)$ and the GW signal in Eq. (3.80) simplifies to

$$s = A_1 h_1 + A_2 h_2 + A_3 h_3 + A_4 h_4 + A_{1S} h_{1S} + A_{2S} h_{2S}. \quad (3.120)$$

3.2.1 Data analysis method

In this section, we shall present the data analysis method to detect the signal $s(t)$ given by Eq. (3.120) and estimate its parameters. The signal $s(t)$ is a linear combination of six amplitudes, and these amplitudes are functions of five astrophysical

parameters. To detect the signal, we adopt the likelihood ratio test which is equivalent to comparing the statistic \mathcal{L} given by Eq. (3.113) to a threshold. Once the signal is detected, we obtain the maximum likelihood estimators \hat{A}_l of the six amplitude parameters A_l using the Eqs. (3.111, 3.112, 3.115, 3.116, 3.117, 3.118). It is important to estimate the five astrophysical parameters $h_o, h_o^d, \psi, \iota,$ and ϕ_0 . We estimate these five parameters by a least-squares (LS) fit determined by six amplitude parameters.

The estimators are obtained by minimizing the following function with respect to the astrophysical parameters:

$$LS = \sum_{l=1}^6 \sum_{l'=1}^6 \left[\hat{A}_l - A_l(h_o, h_o^d, \psi, \iota, \phi_0) \right] \Gamma_{A_l A_{l'}} \left[\hat{A}_{l'} - A_{l'}(h_o, h_o^d, \psi, \iota, \phi_0) \right], \quad (3.121)$$

where $\Gamma_{A_l A_{l'}}$ are components of the Fisher matrix given by Eq. (3.92). The least-squares fit involves a non-linear minimization procedure for which we need the initial values for the five parameters ($h_o, h_o^d, \psi, \iota, \phi_0$) with respect to which the LS function is minimized. We use an analytic solution for the six parameters in terms of the amplitude estimators for the initial values. Several such solutions exist, but we use the one given by the equations below. Firstly we introduce the following auxiliary quantities.

$$A \equiv \hat{A}_1^2 + \hat{A}_2^2 + \hat{A}_3^2 + \hat{A}_4^2, \quad (3.122)$$

$$P \equiv \hat{A}_1 \hat{A}_4 - \hat{A}_2 \hat{A}_3, \quad (3.123)$$

$$h_{0+} = \sqrt{\frac{1}{2}(A + \sqrt{A^2 - 4P^2})}, \quad (3.124)$$

$$h_{0\times} = \text{sign}(P) \sqrt{\frac{1}{2}(A - \sqrt{A^2 - 4P^2})}. \quad (3.125)$$

The quadrupole amplitude h_0^Q is then given by

$$h_o = h_{0+} + \sqrt{(h_{0+})^2 - (h_{0\times})^2}. \quad (3.126)$$

The expressions for parameters ψ and ι are

$$\tan 4\psi = \frac{2(\hat{A}_1 \hat{A}_2 + \hat{A}_3 \hat{A}_4)}{\hat{A}_1^2 + \hat{A}_3^2 - \hat{A}_2^2 - \hat{A}_4^2} \quad (3.127)$$

and

$$\iota = \arccos \left(\frac{h_{0\times}}{h_o} \right). \quad (3.128)$$

We see that the quadrupole amplitude and angles ψ and ι can be calculated from the four amplitudes of the quadrupole signal. With the value of inclination angle ι obtained from Eq. (3.128) above, we easily obtain expressions for dipole amplitude h_o^d and phase angle ϕ_0 from the two dipole amplitudes.

$$h_{0S}^d = \frac{\sqrt{\hat{A}_{1S}^2 + \hat{A}_{2S}^2}}{\sin \iota} \quad (3.129)$$

$$\phi_o = \arctan \left(\frac{\hat{A}_{1S}}{\hat{A}_{2S}} \right) \quad (3.130)$$

Chapter 4

Monte Carlo Simulations

4.0.1 Monte Carlo simulations

We have performed Monte Carlo simulations to test the performance of the data analysis method proposed in the previous Section. Each simulation consists of generating a signal given by Eq. (3.120) and adding it to white, Gaussian noise. Then for each simulation we calculate the \mathcal{F} and \mathcal{D} statistics given by Eqs. (3.114) and (3.104) and we estimate the four quadrupole amplitudes and the two dipole amplitudes from Eqs. (3.115, 3.116, 3.117, 3.118) and (3.111, 3.112) respectively. We perform the simulations for a range of signal-to-noise ratios. For each value of the signal-to-noise ratio we repeat our simulations 1000 times for different realizations of noise.

Figure 4.1 shows the plots of the means and standard deviations of the \mathcal{D} -statistic and the \mathcal{F} -statistic against the signal-to-noise ratio of the signals added whereas Figure 4.2 shows the sum of \mathcal{D} and \mathcal{F} statistics. We compare the simulated values with the theoretical predictions. In Gaussian noise the $2 \times \mathcal{F}$ -statistic has the non-central χ^2 distribution with 4 degrees of freedom (when the signal is present) and non-centrality parameter equal to ρ^2 whereas $2 \times \mathcal{D}$ -statistic has the non-central χ^2 distribution with 2 degrees of freedom. For any non-central χ^2 distribution with k independent degrees of freedom, the mean (μ) and standard deviation (σ) are given by

$$\mu = k + \lambda \quad (4.1)$$

and

$$\sigma = \sqrt{2(k + 2\lambda)} \quad (4.2)$$

where λ is the non-centrality parameter. In our case, $\lambda = \rho^2$, where ρ is the signal-to-noise ratio defined by Eq. (3.89).

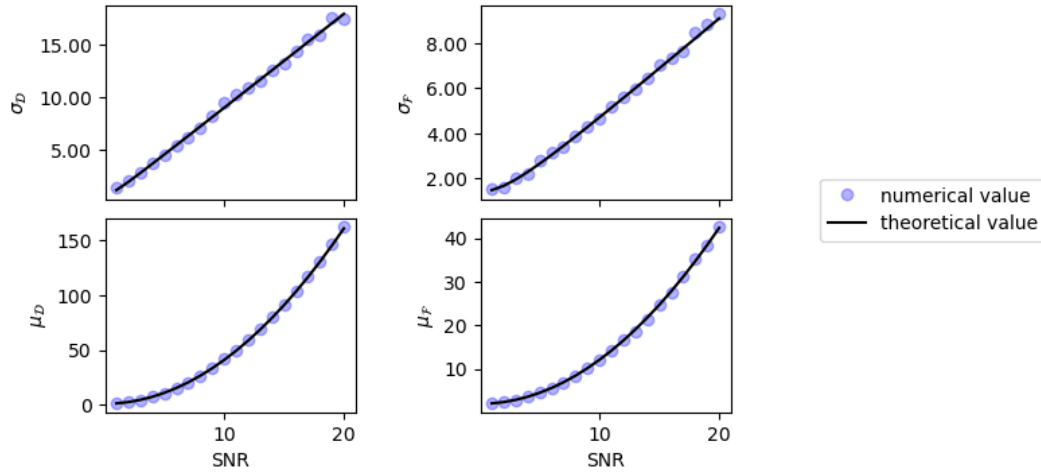


FIGURE 4.1: Simulated mean μ and standard deviation σ of the \mathcal{F} -statistic (left panels) and the \mathcal{D} -statistic (right panel) for an array of SNRs. Continuous lines are the theoretical predictions.

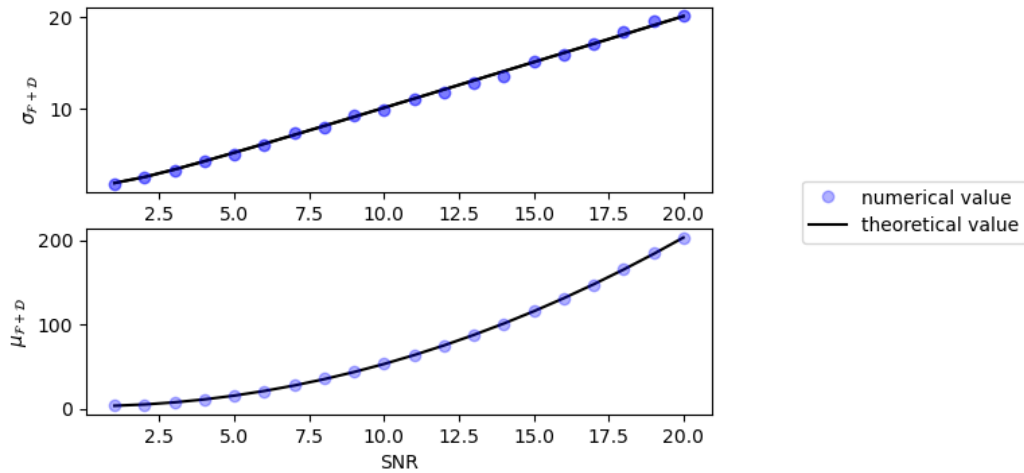


FIGURE 4.2: Simulated mean μ and standard deviation σ of the sum of \mathcal{F} -statistic and \mathcal{D} -statistic for an array of SNRs. Continuous lines are the theoretical predictions.

For the case of amplitude parameters we calculate biases and variances of the parameter estimators and compare them with the theoretical values. For a parameter, the numerical bias in percentage is $\frac{\text{numerical value} - \text{true value}}{\text{true value}} \times 100$. The theoretical biases of parameter estimators are zero whereas the variances are square roots of the diagonal elements of the inverse of the Fisher matrix given by Eq. (3.92). Figures 4.3 and 4.4 show the biases and standard deviations of the estimators of the four quadrupole amplitudes.

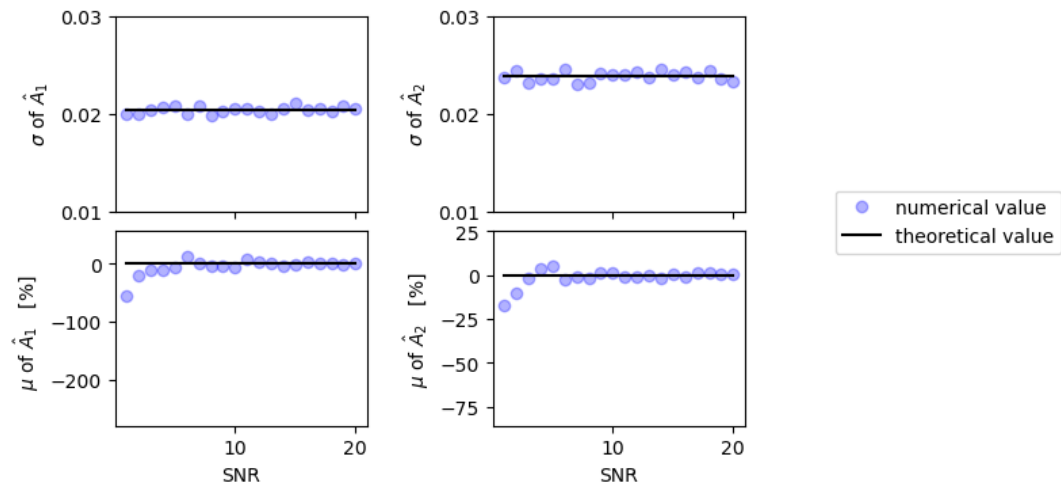


FIGURE 4.3: Bias and standard deviation of the quadrupole amplitudes A_1 (left panel) and A_2 (right panel). Theoretical predictions are drawn as continuous lines.

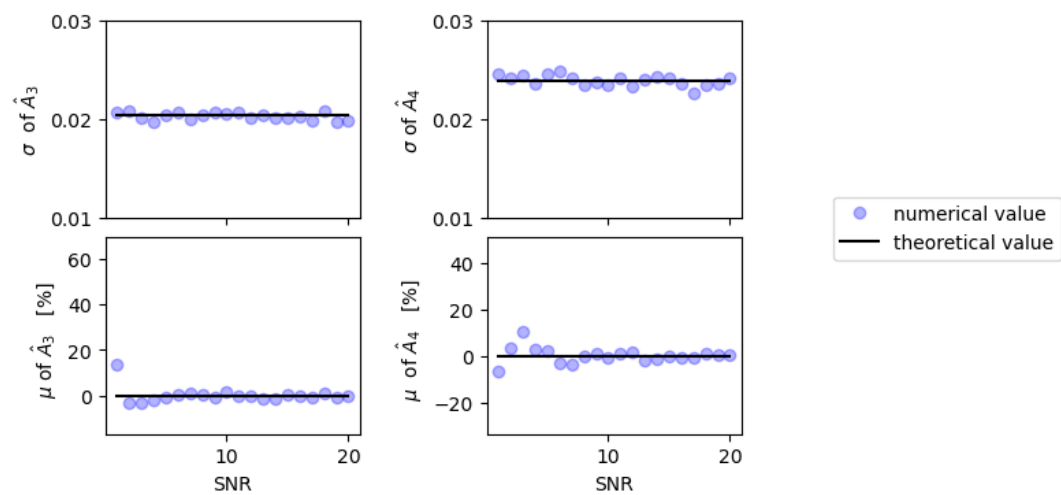


FIGURE 4.4: Bias and standard deviation of the quadrupole amplitudes A_3 (left panel) and A_4 (right panel). Theoretical predictions are drawn as continuous lines.

In Figure 4.5 we present the bias and standard deviation of the estimators of two amplitudes from the dipole radiation.

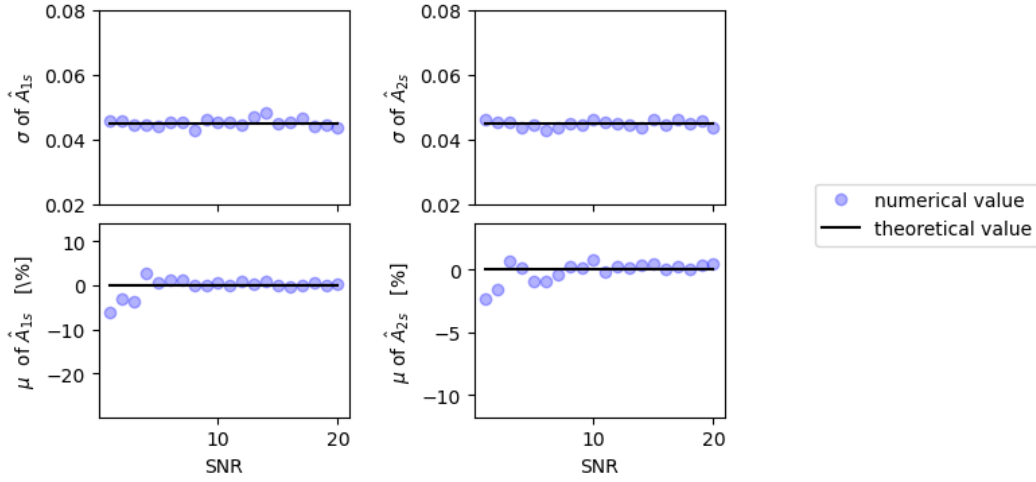


FIGURE 4.5: Bias and standard deviation of dipole amplitudes: A_{1s} (left) and A_{2s} (right)

From our simulations we also estimate the five astrophysical parameters $\theta = (h_o, h_o^d, \psi, \iota, \phi_o)$ using the least squares procedure presented in the previous section. The theoretical estimates of the standard deviation can be obtained from the Fisher matrix $\Gamma(\theta)$ for the astrophysical parameters which is given by the following formula

$$\Gamma(\theta) = J^T \cdot \Gamma(\mathcal{A}) \cdot J \quad (4.3)$$

where $\Gamma(\mathcal{A})$ is the Fisher matrix for the amplitude parameters given by Eq. (3.92) and J is the 6×5 Jacobi matrix with elements $J_{lm} = \frac{\partial A_l}{\partial \theta_m}$ ($l \in [1, 6]$ and $m \in [1, 5]$).

Figures 4.6, 4.7, and 4.8 present the biases and standard deviations of the five astrophysical parameters. We have plotted the theoretical mean and standard deviation against the initial estimators and estimators obtained from the LS procedure as described in the subsection 3.2.1 of chapter 3.

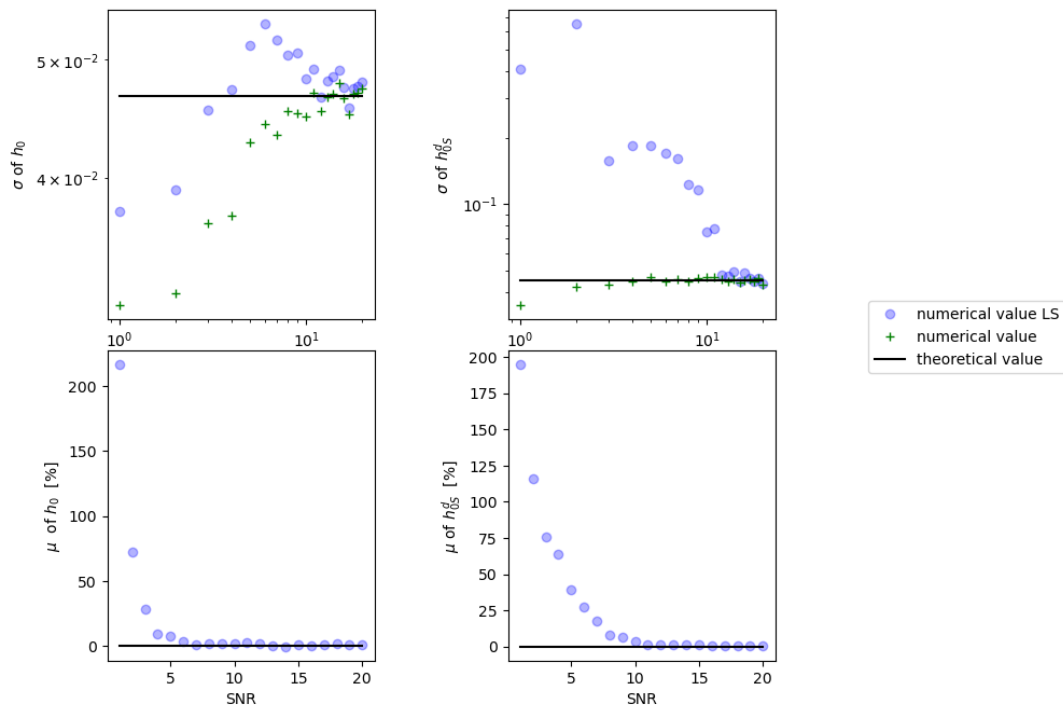


FIGURE 4.6: Bias and standard deviation of estimators of the two amplitude parameters h_o (left panels) and h_o^d (right panels). The crosses are for initial estimators obtained from the Eqs. (3.126, 3.129) and the dots are for the estimators from the least-squares procedure. Continuous lines are theoretical predictions from the Fisher matrix. The standard deviation is a log-log plot.

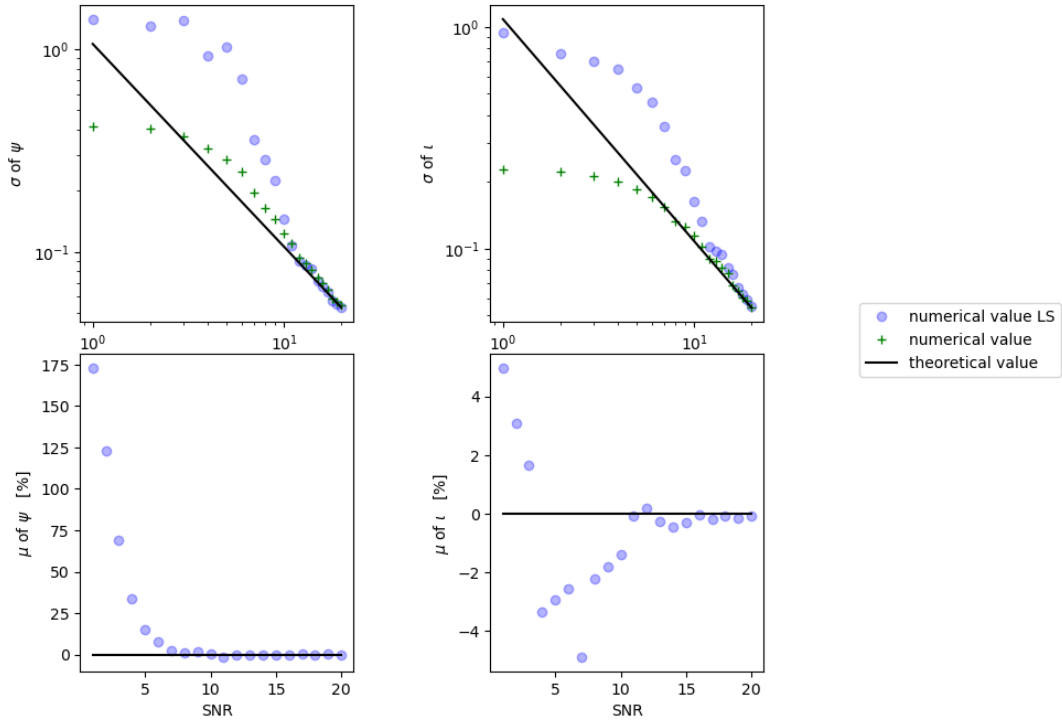


FIGURE 4.7: Bias and standard deviation of estimators of angles ψ (left panels) and ι (right panels). The crosses are for initial estimators obtained from the Eqs. (3.127, 3.128) and the dots are for the estimators from the least-squares procedure. Continuous lines are theoretical predictions from the Fisher matrix. The standard deviation is a log-log plot.

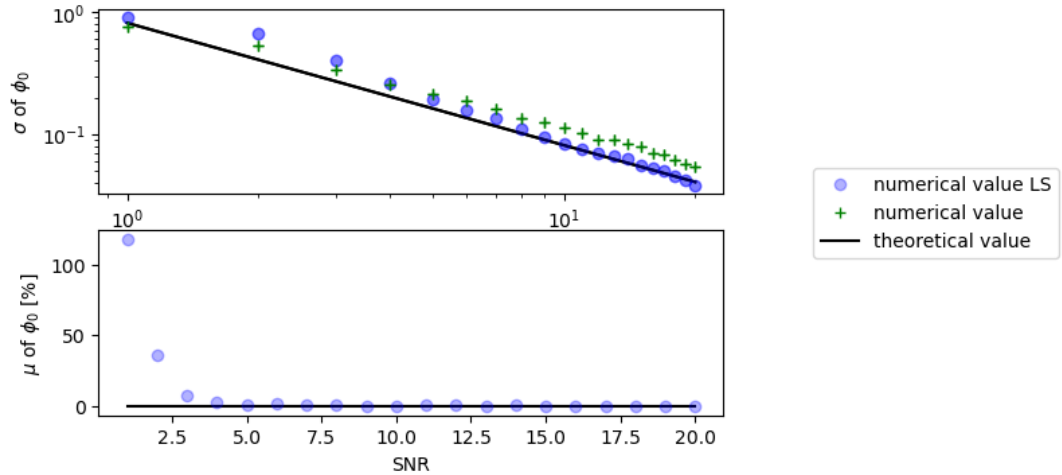


FIGURE 4.8: Bias and standard deviation of phase angle ϕ_0 . The crosses are for initial estimators obtained from the Eq. (3.130) and the dots are for the estimators from the least-squares procedure. Continuous lines are theoretical predictions from the Fisher matrix. The standard deviation is a log-log plot.

The astrophysical parameters are related to amplitude parameters by non-linear transformation consequently we can expect that their estimators will be unbiased and minimum variance only asymptotically, for a large signal-to-noise ratio. Also,

the estimators obtained from the LS procedure agree well with the theoretical predictions.

Chapter 5

Analysis of LIGO-Virgo-Kagra data

5.1 Introduction

In this chapter, we discuss the results of our quest to search for the continuous waves (CWs) from known pulsars. We look for the signals at once and twice the spin frequency of the star. We include in the analysis the search for dipole radiation predicted by Brans-Dicke (BD) theory that comes at once the spin frequency of the pulsar. First, we briefly discuss the data used for this analysis and some basic definitions used frequently in searching for continuous GWs.

5.2 Data

Electromagnetic observations from different observatories provided ephemerides (pulsar position, frequency and frequency measurements) used to follow potential GW signals in the data through a coherent integration process. The ephemerides for the pulsars have been obtained from observations using the CHIME, Hobart, Jodrell Bank, MeerKAT, Nancay, NICER and UTMOST observatories.

After obtaining the pulsar parameters, we have used LVK O2 and O3 data to perform our analysis. The O2 run commenced on October 30, 2016, and ended on August 25, 2017. The Virgo detector joined the observation run on August 01, 2017. The duty factors for LLO, LHO and Virgo were 57%, 59% and 80%, respectively. The O3 observation was run between April 01, 2019, and March 27, 2020. The duty factors for LLO, LHO and Virgo were 76%, 71% and 76%, respectively.

5.3 Definitions

This section presents some essential definitions that frequently appear in the searches of continuous GWs from pulsars.

1. **Recycled pulsar:** A pulsar that may not necessarily rotate fast enough to be classified as a millisecond pulsar, but is expected to have acquired its high rotational velocity by accreting matter from a companion star.
2. **Glitches:** A transient increase in the spin frequency or its first derivative is known as a *glitch*, and this phenomenon is usually common in young non-recycled pulsars. Glitches affect the GW phase identically to the electromagnetic radiation phase with an unknown phase offset at the glitch time.
3. **Restricted orientation:** The determination of the pulsar's orientation from the X-ray modelling of its pulsar wind nebulae is known as restricted orientation. This provides a prior on inclination angle and polarization angle.

4. **Clean process:** The removal of narrow-band spectral artefacts at the calibration and power lines is known as the cleaning process.
5. **Spin-down limit:** The limit placed on the amplitude of gravitational waves from a pulsar is based on the assumption that all the rotational kinetic energy lost by the star as it spins down is through gravitational radiation. This assumes a precisely known distance to the pulsar, whereas in reality, pulsar distances can be uncertain by up to a factor of about two. However, we do know that there are other ways that pulsars lose energy, with the primary assumed mechanism being electromagnetic radiation. So, this is the maximum GW amplitude that the scalar or tensor polarization can achieve.
6. **Upper limit:** A statement on the maximum value some quantity can have while still being consistent with the data. Here, the quantity of interest is the maximum intrinsic gravitational-wave strain amplitude of a given continuous wave signal arriving at Earth. We use a 95 % degree-of-belief limit, i.e. given the data there is a 95% probability that the quantity is below this limit.
7. **High value pulsars:** A pulsar is known as a high-value pulsar if the upper limit on the amplitude of the signal is less than the spin-down limit ($h_0^{ul} < h_0^{sd}$). In this case, we say that pulsar has surpassed the spin-down limit.
8. **Ellipticity:** Roughly it can be thought of as the ratio between the size of deformation, or "mountain", Δr , compared to star's radius, r , so $\epsilon = \Delta r/r$. But, technically this is a ratio of the difference between two perpendicular moments of inertia and the third perpendicular, principal, moment of inertia.
9. **Characteristic age:** The "age" of a pulsar as determined using its current frequency and spin-down rate, and an assumption about the mechanism(s) that is slowing it down, i.e., through gravitational-wave emission.
10. **Millisecond pulsar:** A rapidly rotating pulsar with a rotational period less than about 30 milliseconds and a very low spin-down rate.

5.4 Search Methods

This section briefly explains different search methods employed to detect continuous GWs.

1. **Targeted search:** In a targeted search, we look for signals from known pulsars. The GW rotational phase is accurately determined from EM observations. This search is over a small parameter space and limited to unknown signal amplitude and orientation. This is a relatively sensitive search method.
2. **Narrow band search:** The narrow band search is performed around expected frequencies. Here, we drop the assumption that the GW phase evolution follows that of EM observation. This search is more computationally expensive than the targeted search due to the larger parameter space, and hence, only a few targets are considered.
3. **Directed search:** We look at signals from a small sky region in a directed search. This region is a high probability region where a supernovae explosion occurred.

4. **All sky search:** In an all-sky search, we look for signals in all directions over a wide range of parameters.

This thesis employs the targeted search method to search for continuous waves from pulsars.

5.5 Data Analysis Methods

In targeted searches, there are three different procedures to analyze the data obtained from detectors. They are:

1. **Time domain Bayesian method:** Fermi-Dirac distribution priors are used in this method, and raw GW data is heterodyned using their expected phase evolution. In addition, it includes the correction for relative motion of source with respect to the detector and various relativistic effects [51].
2. **5n-vector method:** This method is a multi-detector matched filter in the frequency domain, based on the sidereal modulation of the expected signal amplitude and phase [52].
3. **$\mathcal{F}/\mathcal{G}/\mathcal{D}$ -statistics:** The \mathcal{F} -statistics is used when amplitude, phase and polarizations are unknown [47]. The \mathcal{G} -statistics is implemented when amplitude and phase are unknown, but polarizations are known [53]. The \mathcal{D} -statistics is used to search for the dipole radiation in the BD theory [54]. The \mathcal{F} and \mathcal{D} -statistics are given by Eqs. (3.114) and (3.104) respectively in chapter 3.

The details of time domain Bayesian method and 5n-vector method are presented in the LIGO-Virgo-Kagra paper [55]. *This thesis utilises $\mathcal{F}/\mathcal{G}/\mathcal{D}$ -statistics to search for CW signals in the noisy detector data.*

5.6 Theoretical models for GW emission

We search for signals from three theoretical models using the $\mathcal{F}/\mathcal{G}/\mathcal{D}$ -statistics. These models are briefly described in subsequent subsections.

5.6.1 Dual Harmonic

In this model, the GWs are emitted at both once and twice the spin frequency of the pulsar. Consider a rotating ellipsoid (symmetric top) as shown in the Figure 5.1. The pulsar is at rest in the body axes system (unprimed coordinate system), and the space axes system (primed coordinate system) represents the inertial reference frame. The Z-axis rotates about the Z'-axis with an angular velocity $2\pi f_0$ that points in the Z-direction, where f_0 is the spin frequency of the pulsar [56], [57].

The angular momentum \vec{L} , in this case, is given by

$$\vec{L} = \begin{bmatrix} I_{xx} & I_{xy} & I_{xz} \\ I_{yx} & I_{yy} & I_{yz} \\ I_{zx} & I_{zy} & I_{zz} \end{bmatrix} \begin{bmatrix} 0 \\ 0 \\ 2\pi f_0 \end{bmatrix} \quad (5.1)$$

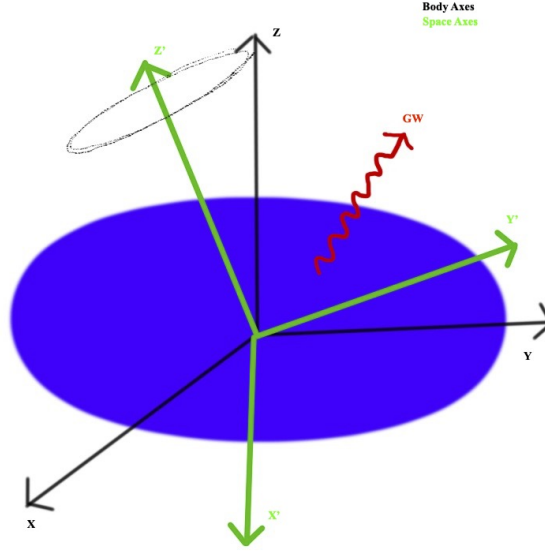


FIGURE 5.1: An ellipsoid rotates about an axis different from its principal axes. The ellipsoid is at rest in the body axes XYZ (black), and it rotates about Z' -axis, an inertial frame (green).

where I_{ij} is the moment of inertia tensor. This gives $L_x = 2\pi f_0 I_{xz}$, $L_y = 2\pi f_0 I_{yz}$ and $L_z = 2\pi f_0 I_{zz}$. The angular velocity in the Z -direction produces angular momentum in all three directions and in this model, GWs are emitted at the frequencies $f = f_0$ and $f = 2f_0$.

The signals h_{21} and h_{22} at once and twice the pulsar rotation frequency can be defined as [55]

$$h_{21} = -\frac{C_{21}}{2} \left[F_+(\alpha, \delta, \psi; t) \sin \iota \cos \iota \cos \left(\phi(t) + \Phi_{21}^C \right) + F_\times(\alpha, \delta, \psi; t) \sin \iota \sin \left(\phi(t) + \Phi_{21}^C \right) \right], \quad (5.2)$$

$$h_{22} = -C_{22} \left[F_+(\alpha, \delta, \psi; t) (1 + \cos^2 \iota) \cos \left(2\phi(t) + \Phi_{22}^C \right) + 2F_\times(\alpha, \delta, \psi; t) \cos \iota \sin \left(2\phi(t) + \Phi_{22}^C \right) \right], \quad (5.3)$$

where C_{21} and C_{22} are the dimensionless constants that give the component amplitudes, the angles (α, δ) are the right ascension and declination of the source, while the angles (ι, ψ) describe the orientation of the source's spin axis with respect to the observer in terms of inclination and polarization, Φ_{21}^C and Φ_{22}^C are phase angles at a defined epoch and $\phi(t)$ is the rotational phase of the source given by the Eq. (3.51). The antenna functions F_+ and F_\times describe how the two polarization components (plus and cross) are projected onto the detector. h_{21} corresponds to $l=2, m=1$, and h_{22} represents $l=2, m=2$ components in spherical harmonics. The explicit formulae for $F_+(t)$ and $F_\times(t)$ are

$$F_+(t) = a(t) \cos 2\psi + b(t) \sin 2\psi \quad (5.4)$$

$$F_+(t) = b(t) \cos 2\psi - a(t) \sin 2\psi \quad (5.5)$$

where $a(t)$ and $b(t)$ are modulation functions given by Eqs. (3.49) and (3.50).

5.6.2 Single Harmonic

In this model, the GWs are emitted at twice the spin frequency of the pulsar. Consider a rotating ellipsoid (symmetric top) as shown in the Figure 5.2. The pulsar is at rest in the body axes system (unprimed coordinate system), and the space axes system (primed coordinate system) represents the inertial reference frame. The z-axes of both the coordinate systems coincide, and the angular velocity $2\pi f_0$ points in the Z-direction, where f_0 is the spin frequency of the pulsar. This situation represents a symmetric top that rotates about one principal axis.

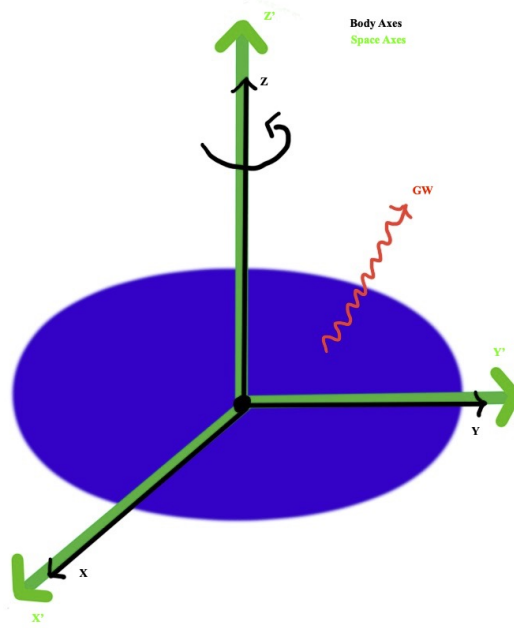


FIGURE 5.2: An ellipsoid rotates about an axis same as its principal axes. The body coordinate system is represented by XYZ (black), and the inertial coordinate system is shown by X'Y'Z' (green).

The angular momentum \vec{L} , in this case, is given by

$$\vec{L} = \begin{bmatrix} I_{xx} & 0 & 0 \\ 0 & I_{yy} & 0 \\ 0 & 0 & I_{zz} \end{bmatrix} \begin{bmatrix} 0 \\ 0 \\ 2\pi f_0 \end{bmatrix} \quad (5.6)$$

and we get $L_x = L_y = 0$ and $L_z = 2\pi f_0 I_{zz}$. The angular velocity in the z -direction produces angular momentum only in the z -direction and in this model, GWs are emitted at the frequency $f = 2f_0$.

For the ideal case of a steadily spinning triaxial star emitting GWs only at twice the rotation frequency, the equatorial ellipticity is defined by Eq. (3.75) as

$$\varepsilon \equiv \frac{|I_{xx} - I_{yy}|}{I_{zz}}, \quad (5.7)$$

The ellipticity defines the amount of deformation as a fraction of the star's radius. For the single harmonic model, $C_{21} = 0$ and $C_{22} = 2h_0$ where h_0 is the amplitude of the circularly polarized signal that would be observed if the source lay directly above or below the plane of the detector and had its spin axis pointed directly towards or away from the detector. The equation for h_0 , given by Eq. (3.68), is [58]

$$h_0 = 2C_{22} = \frac{16\pi^2 G}{c^4} \frac{I_{zz} \varepsilon f_0^2}{r}, \quad (5.8)$$

where r is the distance of the source. The spin-down limit in this case is [59]

$$h_0^{\text{sd}} = \frac{1}{r} \left(\frac{5GI_{zz}}{2c^3} \frac{|\dot{f}_0|}{f_0} \right)^{1/2} \quad (5.9)$$

and it is derived as Eq. (D.19) in Appendix D.

5.6.3 Dipole radiation

As discussed in previous chapters, BD theory predicts three independent polarization states: two tensor polarizations, as in GR, and an additional scalar polarization. The dominant scalar radiation in BD theory originates from the time-dependent dipole moment. The signal $h_{11}(l = 1, m = 1)$ due to dipole radiation is [54]

$$h_{11} = A_{1S}h_{1S} + A_{2S}h_{2S}, \quad (5.10)$$

Using Eqs. (3.56), (3.57), (3.60) and (3.61) from chapter 3, we obtain

$$h_{11} = -h_0^d c(\alpha, \delta; t) \sin \iota \sin(\phi(t) + \phi_0), \quad (5.11)$$

where $c(\alpha, \delta; t)$ is the amplitude modulation function and ϕ_0 is the phase angle at time $t = 0$. We see that the dipole radiation comes at the rotational frequency of the pulsar. We assume that the only non-vanishing component D of the dipole moment in the pulsar's frame is in the x -direction. We derived the dipole amplitude h_0^d in Eq. (3.23) of chapter 3 and it is given by

$$h_0^d = \frac{4\pi G}{c^3} \zeta \frac{Df_0}{r}, \quad (5.12)$$

where ζ is the parameter of the BD theory defined by Eq. (2.100). The spin-down limit for the dipole radiation is

$$h_0^{\text{d, sd}} = \frac{1}{r} \left(\zeta \frac{12G}{c^3} I_{zz} \frac{|\dot{f}_0|}{f_0} \right)^{1/2} \quad (5.13)$$

and it is derived as Eq. (D.11) in Appendix D.

In this case, we consider NS as a perfect sphere, and a mountain on its equator produces a time-varying dipole moment. These mountains might be leftover from the conditions during the supernova explosion when the star formed or could be caused during the pulsar's lifetime, such as through accretion. The gravity on the surface of a pulsar is so robust that, according to our measurements, any mountain larger than a few centimeter would be flattened as it crumbled under its own weight.

5.7 Results

We have used the $\mathcal{F}/\mathcal{G}/\mathcal{D}$ -statistics only for the 23 high-value pulsars for this PhD thesis. No statistically significant signals were detected and consequently we imposed upper limits in gravitational wave amplitudes.

The 95% confidence upper limits on the dipole amplitude are given in the second last column of Table 5.1, and the last column shows the false alarm probability, i.e., the probability that the obtained values of the \mathcal{D} -statistic result only from the noise in the data. The most constraining upper limit for dipole radiation is obtained for the millisecond pulsar J0437-4715.

The results for quadrupolar emission in high-value pulsars are shown in Table 5.2. As no CWs were observed, we present the 95% credible upper limits on the gravitational-wave amplitudes C_{22} and C_{21} for the dual harmonic run (searching for the mass quadrupole modes $l = 2, m = 1, 2$) and the gravitational-wave amplitude h_0 for the single harmonic ($l = 2, m = 2$) search. These were all calculated using coherently combined data from all three detectors over the O2 and O3 observing runs or just the O3 run, as appropriate. Due to the calibration amplitude systematic uncertainties for the detectors, the amplitude estimates can have uncertainties of up to $\sim 8\%$. Table 5.3 presents the results for two promising pulsars: Crab and Vela.

No evidence was found for GWs from any pulsars using the standard search methods or the BD method. However, we have produced updated upper limits on the signal amplitudes and surpassed (built limits smaller than) the spin-down limits for 23 pulsars, 9 of which did so for the first time. Two-millisecond pulsars are included in this number: J0437 – 4715 and J0711 – 6830, and J0537 – 6910 which was not analysed in this work but was found to surpass its spin-down limit in a previous analysis. This is exciting because most pulsars surpassing their spin-downs are younger pulsars, and they are spinning down faster, therefore delivering more energy that can be converted to GWs. Moreover, lower mountains are adequate for millisecond pulsars to emit observable GWs due to their higher frequencies. So, for these pulsars, our observations furnish very stringent limits on the mountain height of fractions of a millimetre. We have enhanced the limits calculated in the previous analysis for the Crab pulsar, calculating the upper limit to be the maximum percentage of spin-down caused by GWs to be less than 0.009% (previously $\sim 0.02\%$). This means other mechanisms cause the majority of the spin-down. With an ellipticity of 7.2×10^{-6} this corresponds to a maximum mountain height of ~ 2 cm (previously ~ 3 cm).

TABLE 5.1: Limits on Gravitational-wave Amplitude from dipole radiation in Brans-Dicke theory for 23 Pulsars using the \mathcal{D} -statistic.

Pulsar Name (J2000)	f_0 (Hz)	\dot{P}_0 (ss^{-1})	Distance (kpc)	$h_{0d}^{95\%}$	FAP
J0437-4715	173.7	1.4×10^{-20}	0.16	9.7×10^{-27}	0.92
J0534+2200	29.6	4.2×10^{-13}	2.00	$9.5(7.0) \times 10^{-26}$	0.95(0.31)
J0711-6830	182.1	1.4×10^{-20}	0.11	1.9×10^{-26}	0.96
J0835-4510	11.2	1.2×10^{-13}	0.28	$1.1(0.74) \times 10^{-23}$	0.89(0.39)
J0908-4913	9.4	1.5×10^{-14}	1.00	1.4×10^{-22}	0.89
J1101-6101	15.9	8.6×10^{-15}	7.00	4.7×10^{-25}	0.99
J1105-6107	15.8	1.6×10^{-14}	2.36	2.0×10^{-25}	0.99
J1302-6350	20.9	2.3×10^{-15}	2.30	2.3×10^{-25}	0.93
J1412+7922	16.9	3.3×10^{-15}	2.00	9.6×10^{-25}	0.54
J1745-0952	51.6	8.6×10^{-20}	0.23	2.0×10^{-26}	0.97
J1756-2251	35.1	1.0×10^{-18}	0.73	1.7×10^{-25}	0.99
J1809-1917	12.1	2.6×10^{-14}	3.27	2.7×10^{-23}	0.97
J1813-1749	22.4	1.3×10^{-13}	6.20	2.1×10^{-25}	0.95
J1828-1101	13.9	1.5×10^{-14}	4.77	6.6×10^{-24}	0.96
J1838-0655	14.2	4.9×10^{-14}	6.60	4.7×10^{-24}	0.52
J1849-0001	26.0	1.4×10^{-14}	7.00	1.7×10^{-26}	0.99
J1856+0245	12.4	6.2×10^{-14}	6.32	1.1×10^{-23}	0.71
J1913+1011	27.8	3.4×10^{-15}	4.61	7.5×10^{-26}	0.98
J1925+1720	13.2	1.0×10^{-14}	5.06	5.7×10^{-24}	0.84
J1928+1746	14.5	1.3×10^{-14}	4.34	2.6×10^{-24}	0.72
J1935+2025	12.5	6.1×10^{-14}	4.60	4.2×10^{-24}	0.99
J1952+3252	25.3	5.8×10^{-15}	3.00	8.1×10^{-26}	0.99
J2229+6114	19.4	7.8×10^{-14}	3.00	$5.3(5.8) \times 10^{-26}$	0.99(0.95)

Values in parentheses are those produced using the restricted orientation. The last column shows the false-alarm probability (FAP) for a signal, assuming that the $2\mathcal{D}$ value has a χ^2 distribution with 2 degrees-of-freedom. f_0 is the spin-frequency of the pulsar, \dot{P}_0 is the first time derivative of the time period and $h_{0d}^{95\%}$ is the 95% credible upper limits on the dipole amplitudes of h_{0d} .

5.8 Summary

In this thesis, we have searched for evidence of GWs from 23 pulsars throughout the LIGO and Virgo O2 and O3 runs and across all three detectors (LIGO Hanford, LIGO Livingston and Virgo). These 23 pulsars are the ones that surpassed their spin-down limit. Searches were carried out for three emission models. One assumed GW emission from the $l = m = 2$ mass quadrupole mode, and the other assumed emission from the $l = 2, m = 1, 2$ modes. The third model corresponds to $l = m = 1$ (dipole radiation). For the single harmonic search, new upper limits on amplitude h_0 were produced. New limits on C_{21} and C_{22} are found for the dual harmonic search. The millisecond pulsars that surpassed their spin-down limits, J0437-4715 and J0711-6830, have upper ellipticity limits of 8.5×10^{-9} and 5.3×10^{-9} , respectively. These ellipticity values are lower than the maximum values predicted for various neutron star equations of state [60]. Therefore, our results provide new constraints in physically realistic parts of the ellipticity parameter space. No search found strong evidence of GW emission from any of the pulsars. However, with so many pulsars now surpassing their spin-down limit, including the millisecond pulsars J0437-4715 and J0711-6830, the next observing run O4 could add more pulsars to this count and bring us closer to observing CWs from pulsars for the first time. In addition to the search for CW signals consisting of the tensorial polarizations predicted by GR, this paper provides the first search explicitly targeting the emission of scalar polarization modes predicted by the Brans-Dicke theory.

TABLE 5.2: Limits on Gravitational-wave Amplitude, and Other Derived Quantities, for 23 High-value Pulsars from the $\mathcal{F}(\mathcal{S})$ -statistic Method. For the $\mathcal{F}\text{-}/(\mathcal{S})$ -statistic, the table presents the false-alarm probability for a signal at $l = 2$, $m = 1$ mode and $l = m = 2$ mode, assuming that the $2\mathcal{F}$ value has a χ^2 distribution with 4 degrees-of-freedom and the $2\mathcal{S}$ value has a χ^2 distribution with 2 degrees of freedom.

Pulsar Name (J2000)	f_0 (Hz)	\dot{f}_0 (ss^{-1})	Distance (kpc)	h_0^{sd}	$C_{21}^{95\%}$	$C_{22}^{95\%}$	$h_0^{95\%}$	$Q_{22}^{95\%}$	$e^{95\%}$ ($\text{kg}\cdot\text{m}^2$)	$h_0^{95\%}/h_0^{\text{sd}}$	$\mathcal{F}(\mathcal{S})$ -stat $l=2, m=1$	$\mathcal{F}(\mathcal{S})$ -stat $l=2, m=2$
J0437-4715 ^{cd}	173.7	1.4×10^{-20}	0.16 (e)	8.0×10^{-27}	$7.0(3.1) \times 10^{-26}$	$8.8(5.5) \times 10^{-27}$	$1.7(1.0) \times 10^{-26}$	$6.9(4.4) \times 10^{32}$	$8.9(5.7) \times 10^{-6}$	0.01(0.01)	0.65(0.52)	0.56(0.24)
J0534+2200 ^{c7}	29.6	4.2×10^{-13}	2.00	1.4×10^{-24}	$7.0(3.1) \times 10^{-26}$	$8.8(5.5) \times 10^{-27}$	$1.7(1.0) \times 10^{-26}$	$6.9(4.4) \times 10^{32}$	$8.9(5.7) \times 10^{-6}$	0.01(0.01)	0.65(0.52)	0.56(0.24)
J0711-6830	182.1	1.4×10^{-20}	0.11	1.2×10^{-26}	1.9×10^{-26}	5.2×10^{-27}	9.9×10^{-27}	6.0×10^{29}	7.8×10^{-9}	0.83	0.17	0.34
J0835-4510	11.2	1.2×10^{-13}	0.28	3.4×10^{-24}	$1.7(1.3) \times 10^{-23}$	$1.0(0.16) \times 10^{-25}$	$2.0(0.67) \times 10^{-25}$	$8.2(2.7) \times 10^{33}$	$1.1(0.36) \times 10^{-4}$	0.06(0.02)	0.24(0.17)	0.09(0.02)
J0908-4913	9.4	1.5×10^{-14}	1.00	3.0×10^{-25}	1.1×10^{-22}	2.2×10^{-25}	4.8×10^{-25}	1.0×10^{35}	1.3×10^{-3}	1.6	0.31	0.16
J1101-6101	15.9	8.6×10^{-15}	7.00	4.3×10^{-26}	8.9×10^{-25}	6.5×10^{-27}	1.3×10^{-26}	6.6×10^{33}	8.5×10^{-5}	0.3	0.68	0.88
J1105-6107	15.8	1.6×10^{-14}	2.36	1.7×10^{-25}	1.2×10^{-24}	2.9×10^{-26}	5.8×10^{-26}	1.0×10^{34}	1.3×10^{-4}	0.34	0.48	0.11
J1302-6350	20.9	2.3×10^{-15}	2.30	7.7×10^{-26}	4.2×10^{-25}	1.6×10^{-26}	3.2×10^{-26}	3.1×10^{33}	4.0×10^{-5}	0.41	0.18	0.03
J1412+7922	16.9	3.3×10^{-15}	2.00	9.5×10^{-26}	1.4×10^{-24}	1.2×10^{-26}	2.4×10^{-26}	3.0×10^{33}	3.9×10^{-5}	0.25	0.32	0.66
J1745-0952	51.6	8.6×10^{-20}	0.23	7.5×10^{-27}	2.1×10^{-26}	1.0×10^{-27}	3.7×10^{-27}	5.8×10^{30}	7.5×10^{-8}	0.49	0.60	0.90
J1756-2251	35.1	1.0×10^{-18}	0.73	6.6×10^{-27}	4.4×10^{-26}	1.1×10^{-27}	3.7×10^{-27}	4.0×10^{31}	5.2×10^{-7}	0.56	0.34	0.92
J1809-1917	12.1	2.6×10^{-14}	3.27	1.4×10^{-25}	7.0×10^{-24}	6.3×10^{-26}	1.3×10^{-25}	5.2×10^{34}	6.8×10^{-4}	0.91	0.37	0.11
J1813-1749	22.4	1.3×10^{-13}	6.20	2.2×10^{-25}	1.9×10^{-25}	3.6×10^{-27}	7.2×10^{-27}	1.6×10^{33}	2.1×10^{-5}	0.03	0.42	0.87
J1828-1101	13.9	1.5×10^{-14}	4.77	7.7×10^{-26}	4.1×10^{-24}	1.4×10^{-26}	2.3×10^{-26}	1.0×10^{34}	1.3×10^{-4}	0.30	0.76	0.89
J1838-0655	14.2	4.9×10^{-14}	6.60	1.0×10^{-25}	2.1×10^{-24}	6.3×10^{-26}	1.0×10^{-25}	6.0×10^{34}	7.8×10^{-4}	1.00	0.67	0.96
J1849-0001	26.0	1.4×10^{-14}	7.00	7.0×10^{-26}	3.4×10^{-26}	9.3×10^{-27}	1.9×10^{-26}	3.5×10^{33}	4.6×10^{-5}	0.27	0.92	0.13
J1856+0245	12.4	6.2×10^{-14}	6.32	1.1×10^{-25}	1.2×10^{-23}	1.9×10^{-26}	4.6×10^{-26}	3.5×10^{34}	4.5×10^{-4}	0.42	0.07	0.82
J1913+1011	27.8	3.4×10^{-15}	4.61	5.4×10^{-26}	8.7×10^{-26}	1.0×10^{-26}	2.2×10^{-26}	2.4×10^{33}	3.1×10^{-5}	0.40	0.53	0.08
J1925+1720	13.2	1.0×10^{-14}	5.06	5.9×10^{-26}	6.0×10^{-24}	2.2×10^{-26}	4.3×10^{-26}	2.3×10^{34}	2.9×10^{-4}	0.72	0.10	0.73
J1928+1746	14.5	1.3×10^{-14}	4.34	8.1×10^{-26}	7.8×10^{-25}	2.1×10^{-26}	4.3×10^{-26}	1.6×10^{34}	2.1×10^{-4}	0.53	0.90	0.55
J1935+2025	12.5	6.1×10^{-14}	4.60	1.5×10^{-25}	1.2×10^{-23}	4.2×10^{-26}	8.5×10^{-26}	4.6×10^{34}	5.9×10^{-4}	0.56	1.00	0.43
J1952+3252	25.3	5.8×10^{-15}	3.00	1.0×10^{-25}	1.0×10^{-25}	1.6×10^{-26}	3.0×10^{-26}	2.6×10^{33}	3.4×10^{-5}	0.30	0.54	0.16
J2229+6114	19.4	7.8×10^{-14}	3.00	3.3×10^{-25}	$3.2(4.0) \times 10^{-25}$	$8.0(6.4) \times 10^{-27}$	$1.6(1.2) \times 10^{-26}$	$2.3(1.8) \times 10^{33}$	$3.0(2.3) \times 10^{-5}$	0.05(0.04)	0.78(0.52)	0.74(0.52)

f_0 is the spin-frequency of the pulsar, \dot{f}_0 is the first time derivative of the time period, h_0^{sd} is the 95% credible upper limits on the amplitudes of h_0 , $h_0^{95\%}$ is the 95% credible upper limits on the gravitational-wave amplitudes C_{21} , $C_{22}^{95\%}$ is the 95% credible upper limits on the gravitational-wave amplitudes C_{22} , $Q_{22}^{95\%}$ is the 95% credible upper limits on the quadrupole moments and $e^{95\%}$ is the 95% credible upper limits on the ellipticity. Values in parentheses are those produced using the restricted orientation.

TABLE 5.3: A comparison between Crab and Vela pulsars.

Crab (J0534+2200)	Vela (J0835-4510)
Glitch occurred	No glitch occurred
GWs contributes < 0.009% of the spin-down	GWs contributes < 0.27% of the spin-down
$h_0^{95\%} = 1.3(1.2) \times 10^{-26}$ at d = 2 kpc	$h_0^{95\%} = 1.8(1.7) \times 10^{-25}$ at d = 0.28 kpc
$Q_{22}^{95\%} = 5.6(5.0) \times 10^{32}$ kg-m ²	$Q_{22}^{95\%} = 7.2(7.1) \times 10^{33}$ kg-m ²
$\epsilon^{95\%} = 7.2(6.5) \times 10^{-6}$	$\epsilon^{95\%} = 9.3(9.2) \times 10^{-5}$

$h_0^{95\%}$ is the 95% credible upper limits on the amplitudes h_0 , $Q_{22}^{95\%}$ is the 95% credible upper limits on the quadrupole moments and $\epsilon^{95\%}$ is the 95% credible upper limits on the ellipticity. Values in parentheses are those produced using the restricted orientation.

Appendix A

STF tensors and Spherical harmonics

A.1 Multipole expansion

In the Newtonian gravity, the gravitational potential due to a spherically symmetric body at an exterior point is given by $U_{ext} = -\frac{GM}{r}$. Here G is the gravitational constant, M is the total mass of the body, and r is the distance of the point of observation from the centre of the body. Even if the body is not spherically symmetric, we can use the same expression for the potential at a vast distance (compared to the size of the body). This approximation is valid because from a very large distance, the body can be considered as a point mass.

But if the body is not spherically symmetric, then the potential in the vicinity of the body depends on the total mass of the body as well as the distribution of this mass. The theory of multipole expansion takes into account the distribution of mass in a body, and we shall discuss two different formalisms for the multipole expansion [23].

A.1.1 Spherical-harmonic decomposition

This method is valid when a body is not perfectly spherical but slightly deviated from a sphere, for example, a mountain on a neutron star or spherical bodies deformed due to centrifugal forces or tidal forces. In this case, the gravitational potential at an exterior point is given by

$$U_{ext}(t, \vec{x}) = G \sum_{l,m} \frac{4\pi}{2l+1} I_{lm}(t) \frac{Y_{lm}(\theta, \phi)}{r^{l+1}} \quad (\text{A.1})$$

In the above expressions, the range of l is 0 to ∞ , and that of m is $-l$ to l . The quantity I_{lm} is known as multipole moments of mass distribution and it is given by

$$I_{lm}(t) = \int \rho(t, \vec{x}') r'^l Y_{l,m}^*(\theta', \phi') d^3x' \quad (\text{A.2})$$

where $\rho(t, \vec{x}')$ is the density of the body. It should be noted that (r, θ, ϕ) corresponds to the field point and (r', θ', ϕ') corresponds to the source point. $Y_{l,m}(\theta, \phi)$ are known as spherical harmonics functions which are the solution of the angular part of the Laplace equation. The angle θ varies from 0 to π , whereas ϕ varies from 0 to 2π . For $m = 0$, we have

$$Y_{l,0}(\theta) = \sqrt{\frac{2l+1}{4\pi}} P_l(\cos \theta) \quad (\text{A.3})$$

where

$$P_l(\mu) \equiv \frac{1}{2^l l!} \frac{d^l}{d\mu^l} (\mu^2 - 1)^l \quad (\text{A.4})$$

For $m > 0$,

$$Y_{l,m}(\theta, \phi) = \sqrt{\frac{2l+1}{4\pi} \frac{(l-m)!}{(l+m)!}} P_l^m(\cos \theta) e^{im\phi} \quad (\text{A.5})$$

where

$$P_l^m(\mu) \equiv (-1)^m (1 - \mu^2)^{\frac{m}{2}} \frac{d^m}{d\mu^m} P_l(\mu) \quad (\text{A.6})$$

$Y_{l,m}^*(\theta, \phi)$ is the complex conjugate of $Y_{l,m}(\theta, \phi)$. One of the crucial properties of spherical harmonics is

$$Y_{l,-m}(\theta, \phi) = (-1)^m Y_{l,m}^*(\theta, \phi) \quad (\text{A.7})$$

The physical interpretation of l and m is as follows. $l = 0$ and $m = 0$ gives monopole moment, $l = 1$ and $m = (-1, 0, 1)$ corresponds to dipole moment and $l = 2$ and $m = (-2, -1, 0, 1, 2)$ compares with the quadrupole moment.

The decomposition in spherical harmonics relies on spherical polar coordinates, and keeps the polar angles (θ, ϕ) segregated from the radial coordinate r .

A.1.2 Symmetric tracefree tensors

The next approach is to expand gravitational potential in terms of tensorial combinations of the unit vector $\hat{n} = \frac{\vec{x}}{r}$ instead of spherical harmonics. Each tensor that we shall construct from \hat{n} will have the property of being symmetric under the exchange of any two of its indices, and of being tracefree in any pair of indices; these tensors are known as symmetric tracefree tensors, or STF tensors. In this case, the potential at an external point can be written as

$$U_{ext}(t, \vec{x}) = G \sum_{l=0}^{\infty} (-1)^l I^{<L>} \partial_{<L>} \left(\frac{1}{r} \right) \quad (\text{A.8})$$

where

$$I^{<L>}(t) = \int \rho(t, \vec{x}') x'^{<L>} d^3 x' \quad (\text{A.9})$$

In the above expression, $<L>$ denotes the STF tensor and L represents a collection of l individual indices. $I^{<L>}$ represents the multipole expansion in terms of STF tensor. For example, let $l = 2$ and $<L> = <ij>$, then

$$\partial_L \left(\frac{1}{r} \right) = \partial_i \partial_j \left(\frac{1}{r} \right) = (3n_j n_k - \delta_{jk}) r^{-3} \quad (\text{A.10})$$

If the function is continuous, then the partial derivatives commute, and hence we can write $\partial_i \partial_j = \partial_j \partial_i$. This, in general, valid for any number of indices. If we exclude the origin, then $(\frac{1}{r})$ is a continuous function. We observe that the tensors on the right-hand side are all symmetric under an exchange of any two indices, and that they all vanish when a trace is taken over any pair of indices (which means that

the indices within the pair are made equal and summed over). So, we can conclude that $\partial_L \left(\frac{1}{r}\right)$ is a STF tensor and we can write it as $\partial_{\langle L \rangle} \left(\frac{1}{r}\right)$.

Similarly, we can understand the difference between x'^L and $x'^{\langle L \rangle}$. When $l = 1$ and $\langle L \rangle = \langle i \rangle$, we get

$$x'^{\langle L \rangle} = x'^L = x'^i \quad (\text{A.11})$$

When $l = 2$ and $\langle L \rangle = \langle ij \rangle$

$$x'^L = x'^i x'^j \quad (\text{A.12})$$

$$x'^{\langle L \rangle} = x'^i x'^j - \frac{1}{3} r'^2 \delta^{ij} \quad (\text{A.13})$$

By using the above equations, the dipole moment in terms of STF tensor is given by

$$D^i \equiv I^{\langle i \rangle} = \int \rho(t, \vec{x}') x'^i d^3 x' \quad (\text{A.14})$$

and the quadrupole moment is written as

$$Q^{ij} \equiv I^{\langle ij \rangle} = \int \rho(t, \vec{x}') \left(x'^i x'^j - \frac{1}{3} r'^2 \delta^{ij} \right) d^3 x' \quad (\text{A.15})$$

Similarly, one can obtain higher multipole moments using more number of indices.

A.1.3 The relation between spherical harmonics decomposition and STF tensors

We have seen that spherical harmonics decomposition and STF tensors are two different ways of finding the gravitational potential from the same body. Therefore, there must exist a way to move from one formalism to another.

The multipole moments in spherical harmonics can be obtained from STF using the relation

$$I_{l,m} = y_{l,m}^{\langle L \rangle} I_{\langle L \rangle} \quad (\text{A.16})$$

where $y_{l,m}^{\langle L \rangle}$ is a constant STF tensor which are related to spherical harmonics using the relation

$$Y_{l,m}(\theta, \phi) = y_{l,m}^{*\langle L \rangle} n_{\langle L \rangle} \quad (\text{A.17})$$

where $n_{\langle L \rangle}$ is a STF combination of unit radial vectors given by

$$\hat{n} = (n^x, n^y, n^z) = (\sin \theta \cos \phi, \sin \theta \sin \phi, \cos \theta) \quad (\text{A.18})$$

For a quadrupole moment tensor, $\langle L \rangle = \langle ij \rangle$ and $I_{\langle L \rangle} = I_{\langle ij \rangle} = Q_{ij}$. This gives

$$I_{lm} = y_{lm}^{\langle ij \rangle} Q_{ij} \quad (\text{A.19})$$

The reverse relation to obtaining STF tensors from spherical harmonics is given by

$$I^{<L>} = \frac{4\pi(l)!}{(2l+1)!!} \sum_{m=-l}^l y_{lm}^{*<L>} I_{lm} \quad (\text{A.20})$$

where $y_{lm}^{*<L>}$ is the complex conjugate of $y_{lm}^{<L>}$. For a quadrupole moment tensor, $l = 2$, $<L> = <ij>$ and $I^{<L>} = I^{<ij>} = Q^{ij}$. This gives

$$Q^{ij} = \frac{16\pi}{15} \sum_{m=-2}^2 y_{2m}^{*<ij>} I_{2m} \quad (\text{A.21})$$

One of the important properties of constant STF tensor is

$$y_{l,-m}^{<L>} = (-1)^m y_{lm}^{*<L>} \quad (\text{A.22})$$

A.2 Mountain on a neutron star

We shall obtain the multipole expansion for a case when there is a mountain on a spherical neutron star of radius 'a'. In the frame of the star, let the coordinates of the mountain are $(x, y, z) = (a, 0, 0)$. In spherical coordinates, the position of the mountain is given by $(r, \theta, \phi) = (a, \frac{\pi}{2}, 0)$. The quadrupole moment of a perfect sphere is zero, so we need to find the quadrupole moment only due to the mountain. We shall also replace the primed variables with the unprimed variables because it is a definite integration.

Calculation using spherical-harmonic decomposition

$$I_{lm} = \int \rho r^l Y_{lm}^*(\theta, \phi) d^3x \quad (\text{A.23})$$

In spherical coordinates, the density of mountain of mass m is given by

$$\rho = m \frac{\delta(r-a)\delta(\theta-\frac{\pi}{2})\delta(\phi)}{r^2 \sin\theta} \quad (\text{A.24})$$

and the volume element is written as $d^3x = r^2 \sin\theta dr d\theta d\phi$. The gravitational wave emission is dominated by $l = m = 2$, so shall compute I_{22} .

$$Y_{22}(\theta, \phi) = \sqrt{\frac{15}{32\pi}} \sin^2\theta e^{2i\phi} \quad \text{and} \quad Y_{22}^*(\theta, \phi) = \sqrt{\frac{15}{32\pi}} \sin^2\theta e^{-2i\phi} \quad (\text{A.25})$$

Plugging back in all the expressions, we get

$$I_{22} = \sqrt{\frac{15}{32\pi}} m \int_0^a r^2 \delta(r-a) dr \int_0^\pi \delta(\theta-\frac{\pi}{2}) \sin^2\theta d\theta \int_0^{2\pi} e^{-2i\phi} \delta(\phi) d\phi \quad (\text{A.26})$$

or,

$$I_{22} = \sqrt{\frac{15}{32\pi}} m a^2 \quad (\text{A.27})$$

Calculation using STF tensors

$$Q^{ij} = \int \rho(x^i x^j - \frac{1}{3} r^2 \delta^{ij}) d^3x \quad (\text{A.28})$$

In cartesian coordinates, the volume element $d^3x = dx dy dz$ and the density of mountain of mass m is given by

$$\rho = m \delta(x-a) \delta(y) \delta(z) \quad (\text{A.29})$$

$x^1 = x, x^2 = y, x^3 = z$ and $r^2 = x^2 + y^2 + z^2$. The Q^{11} component is given by

$$Q^{11} = Q^{xx} = \frac{2}{3} \int \rho x^2 dx dy dz - \frac{1}{3} \int \rho y^2 dx dy dz - \frac{1}{3} \int \rho z^2 dx dy dz \quad (\text{A.30})$$

We can analyze each term separately.

$$\int \rho x^2 dx dy dz = m \int_{-\infty}^{\infty} x^2 \delta(x-a) dx \int_{-\infty}^{\infty} \delta(y) dy \int_{-\infty}^{\infty} \delta(z) dz = ma^2 \quad (\text{A.31})$$

$$\int \rho y^2 dx dy dz = m \int_{-\infty}^{\infty} \delta(x-a) dx \int_{-\infty}^{\infty} y^2 \delta(y) dy \int_{-\infty}^{\infty} \delta(z) dz = 0 \quad (\text{A.32})$$

$$\int \rho z^2 dx dy dz = m \int_{-\infty}^{\infty} \delta(x-a) dx \int_{-\infty}^{\infty} \delta(y) dy \int_{-\infty}^{\infty} z^2 \delta(z) dz = 0 \quad (\text{A.33})$$

Substituting Eq. (A.31), Eq. (A.32) and Eq. (A.33) in Eq. (A.30), we get

$$Q^{11} = Q^{xx} = \frac{2}{3} ma^2 \quad (\text{A.34})$$

By following the same procedure, we can also calculate other components of the STF quadrupole tensor. The final result is

$$Q^{ij} = \begin{bmatrix} \frac{2}{3} ma^2 & 0 & 0 \\ 0 & -\frac{1}{3} ma^2 & 0 \\ 0 & 0 & -\frac{1}{3} ma^2 \end{bmatrix} \quad (\text{A.35})$$

A.2.1 Verifying the relation between spherical harmonics decomposition and STF tensors

We shall obtain the I_{22} component from STF quadrupole tensor using the relation Eq. (A.19)

We use simple trigonometric identities to obtain constant STF tensors. From any standard textbook, the spherical harmonic function can be written as

$$Y_{22} = \sqrt{\frac{15}{32\pi}} \sin^2 \theta e^{2i\phi} \quad (\text{A.36})$$

which can be expanded as

$$Y_{22} = \sqrt{\frac{15}{32\pi}} [\sin^2 \theta \cos^2 \phi - \sin^2 \theta \sin^2 \phi + 2i \sin^2 \theta \sin \phi \cos \phi] \quad (\text{A.37})$$

Using the Eq. (A.18), we can write

$$\begin{aligned} n^{xx} &= \sin^2 \theta \cos^2 \phi \\ n^{yy} &= \sin^2 \theta \sin^2 \phi \\ n^{zz} &= \cos^2 \theta \\ n^{xy} &= \sin^2 \theta \sin \phi \cos \phi \\ n^{yz} &= \sin \theta \cos \theta \sin \phi \\ n^{xz} &= \sin \theta \cos \theta \cos \phi \end{aligned} \quad (\text{A.38})$$

In terms of unit vectors, we can express Eq. (A.37) as

$$Y_{22} = \sqrt{\frac{15}{32\pi}} [n^{xx} + n^{yy} + in^{xy} + in^{yx}] \quad (\text{A.39})$$

Now, comparing Eq. (A.39) with Eq. (A.17), we obtain

$$\begin{aligned} y_{22}^{<xx>} &= \sqrt{\frac{15}{32\pi}} \\ y_{22}^{<yy>} &= -\sqrt{\frac{15}{32\pi}} \\ y_{22}^{<zz>} &= 0 \\ y_{22}^{<xy>} &= -i\sqrt{\frac{15}{32\pi}} \\ y_{22}^{<yz>} &= 0 \\ y_{22}^{<zx>} &= 0 \end{aligned} \quad (\text{A.40})$$

The only non-vanishing components of Q_{ij} are Q_{xx} , Q_{yy} and Q_{zz} . Plugging back the expressions for Q_{ij} and $y_{lm}^{<ij>}$ (from the box above) in Eq. (A.19) gives

$$I_{22} = y_{22}^{<xx>} Q_{xx} + y_{22}^{<yy>} Q_{yy} + y_{22}^{<zz>} Q_{zz} \quad (\text{A.41})$$

or,

$$I_{22} = \sqrt{\frac{15}{32\pi}} ma^2 \quad (\text{A.42})$$

This result matches the one obtained directly from the spherical harmonics decomposition.

Appendix B

The χ^2 distribution

If Z_1, Z_2, \dots, Z_k are k independent (i.e. $E[Z_i Z_j] = E[Z_i]E[Z_j]$ when $i \neq j$) standard normal random variables (i.e. with zero mean and variance equal to one), then

$$Q_k = Z_1^2 + Z_2^2 + Z_3^2 + \dots + Z_k^2 \quad (\text{B.1})$$

has a χ^2 distribution with k degrees of freedom. The probability density function of this distribution is given by

$$f(x) = \frac{x^{\frac{k}{2}-1} e^{-\frac{x}{2}}}{2^{\frac{k}{2}} \Gamma(\frac{k}{2})} \quad (\text{B.2})$$

The mean of the distribution is given by

$$\mu_0 = k \quad (\text{B.3})$$

and the variance is

$$\sigma_0^2 = 2k \quad (\text{B.4})$$

This is called the *central* χ^2 distribution because all the independent random variable have standard normal distribution with zero mean ($\mu = 0$) and the variance equal to one ($\sigma^2 = 1$).

There is also a *noncentral* χ^2 distribution which is the generalization of the central χ^2 distribution. Let X_1, X_2, \dots, X_k are k independent normal random variables with means $\mu_1, \mu_2, \dots, \mu_k$ and variances equal to one, then

$$P_k = X_1^2 + X_2^2 + X_3^2 + \dots + X_k^2 \quad (\text{B.5})$$

has the *noncentral* χ^2 distribution with k degrees of freedom. The mean of this distribution is given by

$$\bar{\mu} = k + \lambda \quad (\text{B.6})$$

$$\lambda = \sum_{i=1}^k \mu_i^2 \quad (\text{B.7})$$

and the variance is

$$\bar{\sigma}^2 = 2(k + 2\lambda) \quad (\text{B.8})$$

Appendix C

Signal detection and parameter estimation

C.1 Signal detection and parameter estimation in Gaussian noise

Suppose that we want to detect a known signal $s(t)$ embedded in noise $n(t)$, where $s(t)$ and $n(t)$ are continuous functions of time t . The signal detection problem can be posed as a hypothesis testing problem, where the null hypothesis is that the signal is absent, and the alternative hypothesis is that the signal is present. A solution to this problem has been found by Neyman and Pearson [61]. They have shown that, subject to a given false alarm probability, the test that maximizes the detection probability is the likelihood ratio test. Likelihood ratio Λ is the ratio of the probability density function (pdf) when the signal is present to the pdf when it is absent. Assuming that the noise is *additive*, the data $x(t)$ can be written as

$$x(t) = n(t) + s(t). \quad (\text{C.1})$$

In addition if the noise is a *zero-mean*, *stationary*, and *Gaussian* random process, the log likelihood ratio $\log \Lambda$ is given by

$$\log \Lambda = (x|s) - \frac{1}{2}(s|s), \quad (\text{C.2})$$

where the scalar product $(\cdot | \cdot)$ is defined by

$$(x|y) \equiv 4\Re \int_0^\infty \frac{\tilde{x}(f)\tilde{y}^*(f)}{\tilde{S}(f)} df. \quad (\text{C.3})$$

In Eq. (C.3) \Re denotes the real part of a complex expression, f is the frequency, the asterisk is complex conjugation, and \tilde{S} is the *one-sided spectral density of the noise* in the detector. $\tilde{x}(f)$ is the Fourier transform defined by

$$\tilde{x}(f) = \int_{-\infty}^{+\infty} x(t)e^{-2\pi ift} dt \quad (\text{C.4})$$

Eq. (C.2) is called the *Cameron-Martin formula*. From the Cameron-Martin formula we immediately see that in the Gaussian case, the likelihood ratio test consists of correlating the data $x(t)$ with the signal $s(t)$ that is present in the noise and comparing the correlation to a threshold. Such a correlation $G = (x|s)$ is called the *matched filter*. The matched filter is a linear operation on the data.

An important quantity is the optimal *signal-to-noise ratio* ρ defined by

$$\rho^2 \equiv (s|s) = 4 \int_0^\infty \frac{|\tilde{s}(f)|^2}{\tilde{S}(f)} df. \quad (\text{C.5})$$

Since data x is Gaussian and G is linear in x , it has a normal probability density function. Probability density distributions p_0 and p_1 of correlation G when respectively signal is absent and present are given by.

$$p_0(G) = \frac{1}{\sqrt{2\pi\rho^2}} \exp\left[-\frac{1}{2} \frac{G^2}{\rho^2}\right] \quad (\text{C.6})$$

$$p_1(G) = \frac{1}{\sqrt{2\pi\rho^2}} \exp\left[-\frac{1}{2} \frac{(G - \rho^2)^2}{\rho^2}\right]. \quad (\text{C.7})$$

Probability of false alarm Q_F and of detection Q_D are readily expressed in terms of error functions.

$$Q_F = \frac{1}{2} \left[1 - \operatorname{erf}\left(\frac{1}{\sqrt{2}} \frac{G_o}{\rho}\right)\right] \quad (\text{C.8})$$

$$Q_D = \frac{1}{2} \left[1 - \operatorname{erf}\left(\frac{1}{\sqrt{2}} \left(\frac{G_o}{\rho} - \rho\right)\right)\right], \quad (\text{C.9})$$

where G_o is the threshold and the error function erf is defined as

$$\operatorname{erf}(x) = \frac{2}{\sqrt{\pi}} \int_0^x e^{-t^2} dt. \quad (\text{C.10})$$

Thus to detect the signal we proceed as follows. We choose a certain value of the false alarm probability. From Eq. (C.8) we calculate the threshold G_o . We evaluate the correlation G . If G is larger than the threshold G_o we say that the signal is present. We see that in the Gaussian case, a single parameter – signal-to-noise ratio ρ determines both probabilities – of false alarm and detection, and consequently the receiver's operating characteristic. For a given false alarm probability, the greater the signal-to-noise ratio, the greater the probability of detection of the signal.

In general, we know the signal as a function of several unknown parameters θ . Thus to detect the signal we also need to estimate its parameters. A convenient method is the maximum likelihood method, by which estimators are those values of the parameters that maximize the likelihood ratio. Thus the *maximum likelihood estimators* $\hat{\theta}$ of parameters θ are obtained by solving the set of equations

$$\frac{\partial \Lambda(\theta, x)}{\partial \theta_i} = 0, \quad (\text{C.11})$$

where θ_i is the i th parameter. The quality of any parameter estimation method can be assessed using the *Fisher information matrix* Γ and the Cramèr - Rao bound [62]. The components of this matrix are defined by

$$\Gamma_{ij} \equiv \mathbb{E} \left[\frac{\partial \log \Lambda}{\partial \theta_i} \frac{\partial \log \Lambda}{\partial \theta_j} \right] = -\mathbb{E} \left[\frac{\partial^2 \log \Lambda}{\partial \theta_i \partial \theta_j} \right]. \quad (\text{C.12})$$

The Cramèr-Rao bound states that for *unbiased* estimators, the covariance matrix of the estimators $C \geq \Gamma^{-1}$. (The inequality $A \geq B$ for matrices means that the matrix

$A - B$ is non-negative definite). In the case of Gaussian noise, the formula for the Fisher matrix takes the form

$$\Gamma_{ij} = \left(\frac{\partial s(\theta)}{\partial \theta_i} \middle| \frac{\partial s(\theta)}{\partial \theta_j} \right), \quad (\text{C.13})$$

where the scalar product $(\cdot | \cdot)$ is given by Eq. (C.3).

C.2 The case of a monochromatic signal in white noise

Let us consider an application of the maximum likelihood estimation method to the case of a simple signal - a *monochromatic signal*. The monochromatic signal depends on three parameters: amplitude A_o , phase ϕ_o , and angular frequency ω_o , and it has the form

$$s = A_o \cos(\omega_o t - \phi_o). \quad (\text{C.14})$$

Let us rewrite the signal (C.14) as

$$s = A_c \cos(\omega_o t) + A_s \sin(\omega_o t), \quad (\text{C.15})$$

where

$$A_c = A_o \cos \phi_o, \quad (\text{C.16})$$

$$A_s = A_o \sin \phi_o. \quad (\text{C.17})$$

Let us also assume that the noise $n(t)$ is white. In the case of a white noise, the one-sided spectral density $\tilde{S}(f)$ is constant and we denote it by S_0 . Then using the Parseval's theorem, the scalar product $(x|y)$ can be written as

$$(x|y) = \frac{2}{S_0} \int_{-\infty}^{+\infty} x(t)y(t)dt. \quad (\text{C.18})$$

We need $(x|s)$ and $(s|s)$ to calculate $\log \Lambda$. The expression of $(x|s)$ is

$$(x|s) = \frac{2}{S_0} \int_{-\infty}^{+\infty} x(t)s(t)dt = \frac{2}{S_0} \int_{-\infty}^{+\infty} x(t)[A_c \cos(\omega_o t) + A_s \sin(\omega_o t)]dt \quad (\text{C.19})$$

Let us assume that observation time is fixed and finite observation time is equal to T . In this case,

$$(x|s) = \frac{2T}{S_0} [A_c \langle x(t) \cos(\omega_o t) \rangle + A_s \langle x(t) \sin(\omega_o t) \rangle] \quad (\text{C.20})$$

where the operator $\langle \cdot \rangle$ is defined as

$$\langle g(t) \rangle \equiv \frac{1}{T} \int_0^T g(t) dt \quad (\text{C.21})$$

Similarly, $(s|s)$ is given by

$$(s|s) = \frac{2T}{S_0} [A_c^2 \langle \cos^2(\omega_o t) \rangle + A_s^2 \langle \sin^2(\omega_o t) \rangle + A_c A_s \langle \sin(2\omega_o t) \rangle] \quad (\text{C.22})$$

The signal to noise ratio ρ^2 is given by

$$\rho^2 = (s|s) \approx \frac{T}{S_0} [A_c^2 + A_s^2] = \frac{T}{S_0} A_0^2 \quad (\text{C.23})$$

where $A_0^2 = A_c^2 + A_s^2$. We make use of the following identities in the expression of $(s|s)$: $\cos^2(\omega_0 t) = \frac{1+\cos(2\omega_0 t)}{2}$ and $\sin^2(\omega_0 t) = \frac{1-\cos(2\omega_0 t)}{2}$. We assume that the observation time T is much larger than the period of the wave. Thus approximately we have that $\int_0^T \sin(2\omega_0 t) dt = \int_0^T \cos(2\omega_0 t) dt \approx 0$. For the monochromatic signal above, the log Λ ratio is given by

$$\log \Lambda = \frac{T}{S_0} [2A_c \langle x \cos(\omega_0 t) \rangle + 2A_s \langle x \sin(\omega_0 t) \rangle - \frac{1}{2}(A_c^2 + A_s^2)] \quad (\text{C.24})$$

The maximum likelihood estimators \hat{A}_c and \hat{A}_s of the amplitudes A_c and A_s are obtained by solving the set of the following two linear equations which are obtained by differentiating Eq. (C.24) with respect to A_c and A_s .

$$\frac{\partial \log \Lambda}{\partial A_c} = 0, \quad (\text{C.25})$$

$$\frac{\partial \log \Lambda}{\partial A_s} = 0 \quad (\text{C.26})$$

or

$$2 \langle x \cos(\omega_0 t) \rangle - A_c = 0, \quad (\text{C.27})$$

$$2 \langle x \sin(\omega_0 t) \rangle - A_s = 0. \quad (\text{C.28})$$

The maximum likelihood estimators of amplitudes are

$$\hat{A}_c = 2 \langle x \cos(\omega_0 t) \rangle, \quad (\text{C.29})$$

$$\hat{A}_s = 2 \langle x \sin(\omega_0 t) \rangle. \quad (\text{C.30})$$

and substituting them back into the log likelihood ratio we get

$$\log \Lambda_r = 2 \frac{T}{S_0} [\langle x \cos(\omega_0 t) \rangle^2 + \langle x \sin(\omega_0 t) \rangle^2] \quad (\text{C.31})$$

where $\log \Lambda_r$ is called reduced likelihood ratio. The maximum likelihood estimators $\hat{\phi}_0$ and \hat{A}_0 of the phase and amplitude are given by

$$\hat{\phi}_0 = \text{atan}\left[\frac{\langle x \sin(\omega_0 t) \rangle}{\langle x \cos(\omega_0 t) \rangle}\right],$$

$$\hat{A}_0 = 2\sqrt{\langle x \cos(\omega_0 t) \rangle^2 + \langle x \sin(\omega_0 t) \rangle^2}. \quad (\text{C.32})$$

In practice, we are dealing with discrete data. If we divide the time T into N equally spaced samples, we have $T = N\Delta$, where Δ is the step size. The integral sign becomes the summation sign and we have

$$\langle x(t) \cos(\omega_0 t) \rangle = \frac{1}{T} \int_0^T x(t) \cos(\omega_0 t) dt \approx \frac{1}{N\Delta} \sum_{k=1}^N x(t_k) \cos(\omega_0 t_k) \Delta \quad (\text{C.33})$$

or,

$$\langle x(t) \cos(\omega_0 t) \rangle = \frac{1}{N} \sum_{k=1}^N x(t_k) \cos(\omega_0 t_k). \quad (\text{C.34})$$

So, in the discrete case, the maximum likelihood estimators \hat{A}_c and \hat{A}_s are

$$\hat{A}_c = 2 \langle x \cos(\omega_0 t) \rangle = \frac{2}{N} \sum_{k=1}^N x(t_k) \cos(\omega_0 t_k), \quad (\text{C.35})$$

$$\hat{A}_s = 2 \langle x \sin(\omega_0 t) \rangle = \frac{2}{N} \sum_{k=1}^N x(t_k) \sin(\omega_0 t_k).$$

In the case of discrete data spectral density is given by $S_0 = 2\sigma^2\Delta$ and we can rewrite the Eq. (C.31) as

$$\log \Lambda_r = 2 \frac{N\Delta}{2\sigma^2\Delta} \left[\left(\frac{1}{N} \sum_{k=1}^N x(t_k) \cos(\omega_0 t_k) \right)^2 + \left(\frac{1}{N} \sum_{k=1}^N x(t_k) \sin(\omega_0 t_k) \right)^2 \right] \quad (\text{C.36})$$

or,

$$\log \Lambda_r = \frac{1}{N\sigma^2} \left[\left(\sum_{k=1}^N x(t_k) \cos(\omega_0 t_k) \right)^2 + \left(\sum_{k=1}^N x(t_k) \sin(\omega_0 t_k) \right)^2 \right]. \quad (\text{C.37})$$

For the discrete case, the expression for ρ^2 is

$$\rho^2 = \frac{1}{2} \frac{A_0^2}{\sigma^2} N. \quad (\text{C.38})$$

We shall denote the reduced likelihood ratio $\log \Lambda_r$ by \mathcal{F} and we shall call it the \mathcal{F} - statistic. Thus to find the maximum likelihood estimators of parameters of the monochromatic signal, we first find the maximum of the \mathcal{F} - statistic with respect to angular frequency, and the angular frequency $\hat{\omega}_0$ corresponding to the maximum of \mathcal{F} is the maximum likelihood estimator of ω_0 . Then we use Eqs. (C.32) with $\omega_0 = \hat{\omega}_0$ to find the maximum likelihood estimators of phase and amplitude. The maximum likelihood detection method consists of correlating the data $x(t)$ with two filters $F_c = \cos(\omega_0 t_k)$ and $F_s = \sin(\omega_0 t_k)$.

The \mathcal{F} - statistic for the monochromatic signal can also be written as

$$\mathcal{F} = \frac{|\tilde{X}|^2}{N\sigma^2}, \quad (\text{C.39})$$

where \tilde{X} is the discrete Fourier transform of the data:

$$\tilde{X} = \sum_{k=1}^N x(t_k) \exp(-i\omega_0 t_k). \quad (\text{C.40})$$

Thus searching for a monochromatic signal in the white noise consists essentially of Fourier transforming the data.

C.3 The Fisher Matrix

In this Section we shall calculate the Fisher matrix (see Eq. C.12) for the case of a monochromatic signal buried in the white noise.

C.3.1 The case of known angular frequency

Using the above results, we can also calculate the Fisher matrix for this case. Since we have only two unknown parameters in this example, the Fisher matrix will be a 2×2 matrix. The elements of the Fisher matrix for a monochromatic signal $s(t)$ (see Eq. C.15) are given by

$$\begin{aligned} \Gamma_{11} &= \left(\frac{\partial s(\theta)}{\partial A_c} \middle| \frac{\partial s(\theta)}{\partial A_c} \right) = \left(\cos(\omega_0 t) \middle| \cos(\omega_0 t) \right) = \\ &= \frac{2}{S_0} \int_0^T \cos^2(\omega_0 t) dt = \frac{2}{S_0} \int_0^T \left[\frac{1 + \cos(2\omega_0 t)}{2} \right] dt \approx \frac{T}{S_0} \end{aligned} \quad (\text{C.41})$$

Similarly,

$$\Gamma_{12} = \left(\frac{\partial s(\theta)}{\partial A_c} \middle| \frac{\partial s(\theta)}{\partial A_s} \right) = \left(\cos(\omega_0 t) \middle| \sin(\omega_0 t) \right) \approx 0 \quad (\text{C.42})$$

$$\Gamma_{21} = \left(\frac{\partial s(\theta)}{\partial A_s} \middle| \frac{\partial s(\theta)}{\partial A_c} \right) = \left(\sin(\omega_0 t) \middle| \cos(\omega_0 t) \right) \approx 0 \quad (\text{C.43})$$

$$\Gamma_{22} = \left(\frac{\partial s(\theta)}{\partial A_s} \middle| \frac{\partial s(\theta)}{\partial A_s} \right) = \left(\sin(\omega_0 t) \middle| \sin(\omega_0 t) \right) \approx \frac{T}{S_0} \quad (\text{C.44})$$

With the above approximations, the Fisher matrix Γ for the signal (C.14) are given by

$$\Gamma_{ij} = \frac{T}{S_0} \begin{bmatrix} 1 & 0 \\ 0 & 1 \end{bmatrix} \quad (\text{C.45})$$

where $i, j = (A_c, A_s)$.

The covariance matrix is inverse of the Fisher information matrix. That is

$$C = \Gamma^{-1} = \frac{S_0}{T} \begin{bmatrix} 1 & 0 \\ 0 & 1 \end{bmatrix}. \quad (\text{C.46})$$

In the discrete case the covariance matrix takes the form

$$C = \frac{2\sigma^2}{N} \begin{bmatrix} 1 & 0 \\ 0 & 1 \end{bmatrix}, \quad (\text{C.47})$$

where σ^2 is the variance of the noise and N is the number of data points.

C.3.2 The case of unknown frequency ω_0

So far we have studied the case when the unknown parameters are A_c and A_s . We can extend it to the case when the angular frequency ω_0 is also an unknown parameter. As done previously, we can again compute the Fisher matrix but now it will be a 3×3 matrix as we have 3 unknown parameters. Following the similar calculation, we get

$$\Gamma_{11} \approx \frac{T}{S_0} \quad (\text{C.48})$$

$$\Gamma_{12} = \left(\frac{\partial s(\theta)}{\partial A_c} \middle| \frac{\partial s(\theta)}{\partial A_s} \right) = \left(\cos(\omega_0 t) \middle| \sin(\omega_0 t) \right) \approx 0 \quad (\text{C.49})$$

$$\Gamma_{13} = \left(\frac{\partial s(\theta)}{\partial A_c} \middle| \frac{\partial s(\theta)}{\partial \omega_0} \right) = \left(\cos(\omega_0 t) \middle| -A_c t \sin(\omega_0 t) + A_s t \cos(\omega_0 t) \right) \approx \frac{A_s T^2}{2S_0} \quad (\text{C.50})$$

$$\Gamma_{21} = \left(\frac{\partial s(\theta)}{\partial A_s} \middle| \frac{\partial s(\theta)}{\partial A_c} \right) = \left(\sin(\omega_0 t) \middle| \cos(\omega_0 t) \right) \approx 0 \quad (\text{C.51})$$

$$\Gamma_{22} = \left(\frac{\partial s(\theta)}{\partial A_s} \middle| \frac{\partial s(\theta)}{\partial A_s} \right) = \left(\sin(\omega_0 t) \middle| \sin(\omega_0 t) \right) = \frac{T}{S_0} \quad (\text{C.52})$$

$$\Gamma_{23} = \left(\frac{\partial s(\theta)}{\partial A_s} \middle| \frac{\partial s(\theta)}{\partial \omega_0} \right) = \left(\sin(\omega_0 t) \middle| -A_c t \sin(\omega_0 t) + A_s t \cos(\omega_0 t) \right) \approx -\frac{A_c T^2}{2S_0} \quad (\text{C.53})$$

$$\Gamma_{31} = \Gamma_{13} \quad (\text{C.54})$$

$$\Gamma_{32} = \Gamma_{23} \quad (\text{C.55})$$

$$\begin{aligned} \Gamma_{33} &= \left(\frac{\partial s(\theta)}{\partial \omega_0} \middle| \frac{\partial s(\theta)}{\partial \omega_0} \right) \\ &= \left(-A_c t \sin(\omega_0 t) + A_s t \cos(\omega_0 t) \middle| -A_c t \sin(\omega_0 t) + A_s t \cos(\omega_0 t) \right) \\ &\approx \frac{T^3}{3S_0} (A_c^2 + A_s^2) \end{aligned} \quad (\text{C.56})$$

Thus the 3×3 Fisher matrix, in this case, is given by

$$\Gamma_{ij} = \frac{T}{S_0} \begin{bmatrix} 1 & 0 & \frac{A_s T}{2} \\ 0 & 1 & -\frac{A_c T}{2} \\ \frac{A_s T}{2} & -\frac{A_c T}{2} & \frac{T^2}{3} A_0^2 \end{bmatrix} \quad (\text{C.57})$$

and the covariance matrix has the form

$$\mathbf{C} = \Gamma_{ij}^{-1} = \frac{12A_0^2}{T^2 \rho^2} \begin{bmatrix} T^2 \left(\frac{1}{3} - \frac{A_c^2}{4A_0^2} \right) & -\frac{A_c A_s T^2}{4A_0^2} & -T \frac{A_s}{2A_0^2} \\ -\frac{A_c A_s T^2}{4A_0^2} & T^2 \left(\frac{1}{3} - \frac{A_s^2}{4A_0^2} \right) & T \frac{A_c}{2A_0^2} \\ -T \frac{A_s}{2A_0^2} & T \frac{A_c}{2A_0^2} & \frac{1}{A_0^2} \end{bmatrix}, \quad (\text{C.58})$$

where ρ is the signal-to-noise ratio given by Eq. (C.23) and $A_0^2 = A_c^2 + A_s^2$.

While calculating the terms of the Fisher matrix, we have made the following approximations for the oscillatory terms.

$$\int_0^T t \cos(\omega_0 t - \phi) dt \approx \int_0^T t \sin(\omega_0 t - \phi_0) dt \approx 0, \quad (\text{C.59})$$

$$\int_0^T t^2 \cos(\omega_0 t - \phi) dt \approx \int_0^T t^2 \sin(\omega_0 t - \phi_0) dt \approx 0. \quad (\text{C.60})$$

C.3.3 The unknown parameters are A_0 , ϕ and ω_0

Previously we have written down the signal as a function of A_c , A_s and ω_0 . But it can also be written as a function of A_0 , ϕ_0 and ω_0 .

$$s(A_0, \phi_0, \omega_0) = A_0 \cos(\omega_0 t - \phi_0) \quad (\text{C.61})$$

Using the same analysis, the Fisher matrix can be computed as

$$\Gamma_{ij} = \rho^2 \begin{bmatrix} \frac{1}{A_0^2} & 0 & 0 \\ 0 & 1 & -\frac{T}{2} \\ 0 & -\frac{T}{2} & \frac{T^2}{3} \end{bmatrix} \quad (\text{C.62})$$

and hence the covariance matrix is

$$C = \Gamma_{ij}^{-1} = \frac{1}{\rho^2} \begin{bmatrix} A_0^2 & 0 & 0 \\ 0 & 4 & \frac{6}{T} \\ 0 & \frac{6}{T} & \frac{12}{T^2} \end{bmatrix} \quad (\text{C.63})$$

We have expressed the signal in two different sets of parameters. So, we can calculate the Jacobian matrix to move from one parameter space to another. The relation between two different sets of parameters is

$$A_c = A_0 \cos \phi_0$$

$$A_s = A_0 \sin \phi_0$$

$$\omega_0 = \omega_0$$

and the Jacobian matrix is given by

$$J = \begin{bmatrix} \frac{\partial A_c}{\partial A_0} & \frac{\partial A_c}{\partial \phi_0} & \frac{\partial A_c}{\partial \omega_0} \\ \frac{\partial A_s}{\partial A_0} & \frac{\partial A_s}{\partial \phi_0} & \frac{\partial A_s}{\partial \omega_0} \\ \frac{\partial \omega_0}{\partial A_0} & \frac{\partial \omega_0}{\partial \phi_0} & \frac{\partial \omega_0}{\partial \omega_0} \end{bmatrix} = \begin{bmatrix} \cos \phi_0 & -A_0 \sin \phi_0 & 0 \\ \sin \phi_0 & A_0 \cos \phi_0 & 0 \\ 0 & 0 & 1 \end{bmatrix} \quad (\text{C.64})$$

The determinant of the Jacobian matrix is

$$|J| = A_0^2. \quad (\text{C.65})$$

C.4 Statistical properties of the \mathcal{F} -statistic and maximum likelihood estimators

C.4.1 Statistical properties of the maximum likelihood estimators

Let us consider the discrete case and assume that the data are given by

$$x_k = s_k + n_k, \quad k = 1, \dots, N \quad (\text{C.66})$$

where noise samples n_k are drawn from zero mean value Gaussian noise of variance σ^2 and are independent. Thus we have

$$E[n_k] = 0, \quad (\text{C.67})$$

$$E[n_k n_l] = \delta_{kl} \sigma^2, \quad (\text{C.68})$$

where δ_{kl} is the Kronecker delta function.

For the monochromatic signal, the signal samples s_k are given by

$$s_k = A_c \cos(\omega_0 t_k) + A_s \sin(\omega_0 t_k) \quad (\text{C.69})$$

The expectation values of the data samples read

$$E[x_k] = s_k + E[n_k] = s_k. \quad (\text{C.70})$$

The expectation value of the product of the data samples is given by

$$E[x_k x_l] = E[(s_k + n_k)(s_l + n_l)] = E[s_k s_l + s_k n_l + n_k s_l + n_k n_l] \quad (\text{C.71})$$

or

$$E[x_k x_l] = s_k s_l + E[n_k n_l], \quad (\text{C.72})$$

where we have used the fact that $E[s_k n_l] = E[s_k] E[n_l] = 0$ because $E[n_l] = 0$ and similarly $E[s_l n_k] = 0$. As we have seen before, when $k = l$, $E[n_k n_l] = \sigma^2$ otherwise $E[n_k n_l] = 0$. This gives

$$E[x_k x_l] = s_k s_l + \sigma^2 \delta_{kl} \quad (\text{C.73})$$

Let us now calculate the expectation values and variances of the estimators of the amplitude parameters A_c and A_s assuming that the angular frequency ω_0 is known.

The estimator \hat{A}_c of the parameter A_c is given by

$$\hat{A}_c = \frac{2}{N} \sum_{k=1}^N x_k \cos(\omega_0 t_k) = \frac{2}{N} (s_k + n_k) \cos(\omega_0 t_k) \quad (\text{C.74})$$

or

$$\hat{A}_c = \frac{2}{N} (A_c \cos(\omega_0 t_k) + A_s \sin(\omega_0 t_k) + n_k) \cos(\omega_0 t_k) \quad (\text{C.75})$$

or

$$\hat{A}_c = \frac{2}{N} (A_c \cos^2(\omega_0 t_k) + \frac{A_s}{2} \sin(2\omega_0 t_k) + n_k \cos(\omega_0 t_k)) \quad (\text{C.76})$$

The expectation value of \hat{A}_c is

$$E[\hat{A}_c] = A_c \frac{2}{N} \sum_{k=1}^N \cos^2(\omega_0 t_k) + A_s \frac{1}{N} \sum_{k=1}^N \sin(2\omega_0 t_k) + E[n_k] \cos(\omega_0 t_k) \quad (\text{C.77})$$

We use the identity that $\cos^2(\omega_0 t_k) = \frac{1+\cos(2\omega_0 t_k)}{2}$ and the fact that $\sum_{k=1}^N \sin(2\omega_0 t_k) \approx \sum_{k=1}^N \cos(2\omega_0 t_k) \approx \sum_{k=1}^N \cos(\omega_0 t_k) \approx 0$

This gives

$$E[\hat{A}_c] = A_c \frac{2}{N} \frac{1}{2} \sum_{k=1}^N 1 \quad (\text{C.78})$$

or

$$E[\hat{A}_c] = A_c \quad (\text{C.79})$$

Thus, the expectation of the estimator \hat{A}_c of the amplitude A_c is equal to the true value of the amplitude. Such an estimator is called an *unbiased* estimator.

The variance of the estimator \hat{A}_c is given by

$$\text{Var}(\hat{A}_c) = E[(\hat{A}_c - E[\hat{A}_c])^2] = E[(\hat{A}_c - A_c)^2] = E[(\hat{A}_c^2 + A_c^2 - 2\hat{A}_c A_c)] \quad (\text{C.80})$$

or

$$\text{Var}(\hat{A}_c) = E[\hat{A}_c^2] + E[A_c^2] - 2E[\hat{A}_c A_c] \quad (\text{C.81})$$

Using the fact that $E[A_c^2] = A_c^2$ and $E[A_c] = A_c$, we get

$$\text{Var}(\hat{A}_c) = E[\hat{A}_c^2] - A_c^2 \quad (\text{C.82})$$

The value of $E[\hat{A}_c^2]$ can be calculated as shown below

$$E[\hat{A}_c^2] = \frac{4}{N^2} E \left[\sum_{k=1}^N \sum_{l=1}^N x_l \cos(\omega_0 t_l) x_k \cos(\omega_0 t_k) \right] \quad (\text{C.83})$$

or

$$E[\hat{A}_c^2] = \frac{4}{N^2} \sum_{k=1}^N \sum_{l=1}^N E[x_l x_k] \cos(\omega_0 t_l) x_k \cos(\omega_0 t_k) \quad (\text{C.84})$$

Using the Eq. (C.73), this can be written as

$$E[\hat{A}_c^2] = \frac{4}{N^2} \sum_{k=1}^N \sum_{l=1}^N [s_k s_l + \sigma^2 \delta_{kl}] \cos(\omega_0 t_l) \cos(\omega_0 t_k) \quad (\text{C.85})$$

or

$$E[\hat{A}_c^2] = A_c^2 + \frac{2}{N} \sigma^2. \quad (\text{C.86})$$

Thus variance of the estimator of amplitude A_c reads

$$\text{Var}(\hat{A}_c) = \frac{2}{N} \sigma^2 \quad (\text{C.87})$$

We can do the similar analysis for A_s and the final results are

$$E[\hat{A}_s] = A_s \quad (\text{C.88})$$

$$\text{Var}(\hat{A}_s) = \frac{2}{N}\sigma^2 \quad (\text{C.89})$$

Thus we see that the variances of the estimators of the amplitudes A_c and A_s are precisely equal to the diagonal elements of the covariance matrix given by Eq. (C.47) which is the inverse of the Fisher matrix. Consequently, as $E[\hat{A}_c]$ and $E[\hat{A}_s]$ are unbiased, by Cramèr-Rao inequality the estimators $E[\hat{A}_c]$ and $E[\hat{A}_s]$ are also of minimum variance. Such estimators are called *efficient*. Thus in the case of known angular frequency, the amplitude estimators are unbiased and efficient.

In the case of unknown angular frequency ω_0 , this is not the case and the estimators of the amplitudes and ω_0 can only tend to be unbiased and efficient asymptotically for high signal-to-noise ratio. From the diagonal elements of the covariance matrix given by Eq. (C.58) the variances of the parameters are

$$\text{Var}(A_c) = \frac{12A_0^2}{N^2} \left(\frac{1}{3} - \frac{A_c^2}{4A_0^2} \right) \frac{1}{\rho^2}, \quad (\text{C.90})$$

$$\text{Var}(A_s) = \frac{12A_0^2}{N^2} \left(\frac{1}{3} - \frac{A_s^2}{4A_0^2} \right) \frac{1}{\rho^2}, \quad (\text{C.91})$$

$$\text{Var}(\omega_0) = \frac{12}{N^2\Delta^2} \frac{1}{\rho^2}. \quad (\text{C.92})$$

To test the performance of the maximum likelihood estimators in this case, we have performed Monte Carlo simulations. For each simulation we add the monochromatic signal to Gaussian noise. We calculate the \mathcal{F} -statistic using the Fast Fourier Transform. We find the maximum of the statistic and record the angular frequency corresponding to the maximum. This is called the *coarse* search. Then we find the maximum of \mathcal{F} more accurately using the Brent's algorithm with the initial value for ω_0 from the coarse search. This second step is called the *fine* search. Then from the equations (C.35), we calculate the maximum likelihood estimators of the amplitudes using the estimate of ω_0 from the fine search. We have performed this simulation for an array for signal-to-noise ratios from 2 to 42. For each value of SNR, we have performed 1000 injections of the signal to the noise. In Figure C.1, we have plotted biases and standard deviations of the estimators of the two amplitudes for each SNR and in Figure C.2, we have plotted bias and standard deviation of the estimator of angular frequency.

We see that above a certain threshold signal-to-noise ratio (ρ_{th} , $\rho_{th} \sim 8$ in our case), the maximum likelihood estimators are unbiased to a very good accuracy and their variances are close to the minimum variance obtained from the Fisher matrix. Below the threshold signal-to-noise ratio, large deviations occur. This is because when SNR is low, the maximum of the statistic may occur at a frequency for a high noise excursion and not near the frequency of the injected signal.

C.4.2 Statistical distribution of the \mathcal{F} - statistic

In this section, we shall prove that for Gaussian noise the function $2 \times \mathcal{F}$ where \mathcal{F} is the \mathcal{F} - statistic given by Eq. (C.37) has a χ^2 distribution with two degrees of freedom.

We have

$$2\mathcal{F} = Z_1^2 + Z_2^2, \quad (\text{C.93})$$

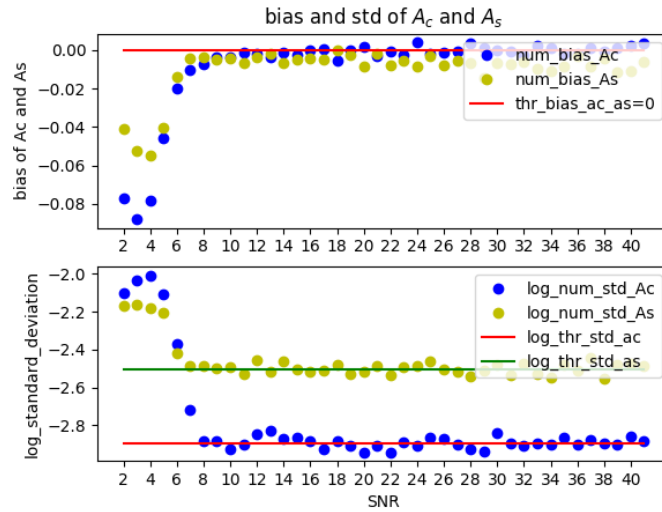


FIGURE C.1: The bias and standard deviation of \hat{A}_c and \hat{A}_s in the three parameter estimation.

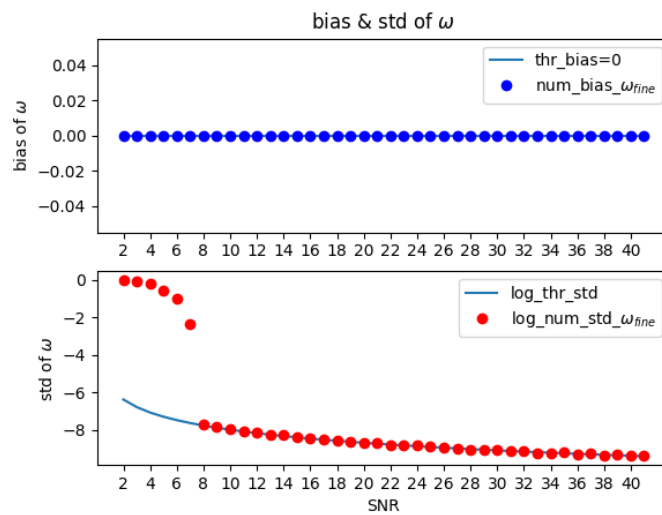


FIGURE C.2: The bias and standard deviation of $\hat{\omega}_0$.

where

$$Z_1 = \sqrt{\frac{2}{N}} \frac{1}{\sigma} \left[\sum_{k=1}^N x_k(t) \cos(\omega_o t_k) \right] \quad (\text{C.94})$$

and

$$Z_2 = \sqrt{\frac{2}{N}} \frac{1}{\sigma} \left[\sum_{k=1}^N x_k(t) \sin(\omega_o t_k) \right]. \quad (\text{C.95})$$

As the functions Z_1 and Z_2 are linear function of the Gaussian data x_k , Z_1 and Z_2 also have Gaussian distributions.

Let us calculate the expectation values of Z_1 and Z_2 when the signal is absent and present.

$$E[Z_1] = \sqrt{\frac{2}{N}} \frac{1}{\sigma} \sum_{k=1}^N E[(n_k + s_k)] \cos(\omega_o t_k). \quad (\text{C.96})$$

Thus when the signal is absent ($s_k = 0$) we have $E_0[Z_1] = 0$ as Gaussian noise has zero mean. When the signal is present we have

$$\begin{aligned} E_1[Z_1] &= \sqrt{\frac{2}{N}} \frac{1}{\sigma} \sum_{k=1}^N s_k \cos(\omega_o t_k) \\ &= \sqrt{\frac{2}{N}} \frac{1}{\sigma} \left[\sum_{k=1}^N (A_c \cos^2(\omega_o t_k) + A_s \sin(\omega_o t_k) \cos(\omega_o t_k)) \right] \\ &= \sqrt{\frac{2}{N}} \frac{1}{\sigma} \left[\sum_{k=1}^N (A_c (\frac{1}{2}(1 + \cos(2\omega_o t_k)) + A_s \sin(\omega_o t_k) \cos(\omega_o t_k)) \right] \\ &= \sqrt{\frac{N}{2}} \frac{A_c}{\sigma} \end{aligned} \quad (\text{C.97})$$

where the last equality results from neglecting the oscillatory terms. Similarly for the variable Z_2 we have

$$E_0[Z_2] = 0, \quad (\text{C.98})$$

$$E_1[Z_2] = \sqrt{\frac{N}{2}} \frac{A_s}{\sigma}. \quad (\text{C.99})$$

To calculate the variances of Z_1 and Z_2 , we need the expectation values $E[Z_1 Z_1]$ and $E[Z_2 Z_2]$. We have

$$\begin{aligned} E[Z_1 Z_1] &= \frac{2}{N\sigma^2} \sum_{k=1}^N \sum_{l=1}^N E[x_l x_l] \cos(\omega_o t_k) \cos(\omega_o t_l) \\ &= \frac{2}{N\sigma^2} \sum_{k=1}^N \sum_{l=1}^N (s_k s_l + \sigma^2 \delta_{kl}) \cos(\omega_o t_k) \cos(\omega_o t_l). \end{aligned} \quad (\text{C.100})$$

When the signal is absent we have

$$\begin{aligned} E_0[Z_1 Z_1] &= \frac{2}{N} \sum_{k=1}^N \cos^2(\omega_o t_k) \\ &= \frac{1}{N} \sum_{k=1}^N (1 + \cos(2\omega_o t_k)) \\ &= 1. \end{aligned} \quad (\text{C.101})$$

where the last equality results from neglecting an oscillatory term.

Thus when signal is absent we have

$$\text{Var}[Z_1] = 1. \quad (\text{C.102})$$

Let us next show that functions Z_1 and Z_2 are independent random variables, i.e. $E[Z_1 Z_2] = E[Z_1]E[Z_2]$ both when the signal is present and absent. We have

$$\begin{aligned} E[Z_1 Z_2] &= \frac{2}{N\sigma^2} \sum_{k=1}^N \sum_{l=1}^N E[x_k x_l] \cos(\omega_o t_k) \sin(\omega_o t_l) \\ &= \frac{2}{N\sigma^2} \sum_{k=1}^N \sum_{l=1}^N (s_k s_l + \sigma^2 \delta_{kl}) \cos(\omega_o t_k) \sin(\omega_o t_l) \\ &= \frac{2}{N\sigma^2} \sum_{k=1}^N \sum_{l=1}^N s_k s_l \cos(\omega_o t_k) \sin(\omega_o t_l) + \frac{1}{N} \sum_{k=1}^N \sin(2\omega_o t_k). \end{aligned} \quad (\text{C.103})$$

Neglecting oscillatory term we have

$$\begin{aligned} E[Z_1 Z_2] &= \frac{2}{N\sigma^2} \sum_{k=1}^N \sum_{l=1}^N E[s_k \cos(\omega_o t_k)] E[s_l \sin(\omega_o t_l)] \\ &= \frac{2}{N\sigma^2} \sum_{k=1}^N \sum_{l=1}^N E[x_k \cos(\omega_o t_k)] E[x_l \sin(\omega_o t_l)] \\ &= E[Z_1] E[Z_2]. \end{aligned} \quad (\text{C.104})$$

Thus we have shown that in the case when signal is absent $2 \times \mathcal{F}$ is the sum of the squares of two independent Gaussian random variables Z_1 and Z_2 with zero means and variances equal to one. Thus when signal is absent by definition (Appendix B) $2 \times \mathcal{F}$ has central χ^2 distribution with two degrees of freedom.

Now we consider the case when signal is present in the data. In this case $2 \times \mathcal{F}$ is the sum of the squares of two Gaussian random variables Z_1 and Z_2 which, as we have shown above are independent.

The non-centrality parameter λ is defined as

$$\lambda = E_1^2[Z_1] + E_1^2[Z_2]. \quad (\text{C.105})$$

From Eqs. (C.97) and (C.99) we have

$$\lambda = \frac{N A_c^2 + A_s^2}{2 \sigma^2} = \frac{N A_0^2}{2 \sigma^2}. \quad (\text{C.106})$$

Thus by Eq. (C.38), the non-centrality parameter is precisely equal to the signal-to-noise ratio squared.

Let us next calculate the expectation value of $2\mathcal{F}$. We have

$$E_1[Z_1 Z_1] = \frac{2}{N\sigma^2} \sum_{k=1}^N \sum_{l=1}^N (s_k s_l + \sigma^2 \delta_{kl}) \cos(\omega_o t_k) \cos(\omega_o t_l). \quad (\text{C.107})$$

Using $s_k = A_c \cos(\omega_o t_k) + A_s \sin(\omega_o t_k)$, we get

$$\begin{aligned}
 E_1[Z_1 Z_1] &= \frac{2}{N\sigma^2} \sum_{k=1}^N \sum_{l=1}^N A_c^2 \cos^2(\omega_o t_k) \cos^2(\omega_o t_l) \\
 &+ \frac{2}{N\sigma^2} \sum_{k=1}^N \sum_{l=1}^N A_c A_s [\sin(\omega_o t_k) \cos(\omega_o t_l) + \cos(\omega_o t_k) \sin(\omega_o t_l)] \cos(\omega_o t_k) \cos(\omega_o t_l) \\
 &+ \frac{2}{N\sigma^2} \sum_{k=1}^N \sum_{l=1}^N A_s^2 \sin(\omega_o t_k) \cos(\omega_o t_k) \sin(\omega_o t_l) \cos(\omega_o t_l) + 1
 \end{aligned} \tag{C.108}$$

Neglecting oscillatory terms we get

$$E_1[Z_1 Z_1] = \frac{2}{N\sigma^2} \sum_{k=1}^N \sum_{l=1}^N A_c^2 \cos^2(\omega_o t_k) \cos^2(\omega_o t_l) + 1. \tag{C.109}$$

or

$$E_1[Z_1 Z_1] = \frac{N}{2\sigma^2} A_c^2 + 1. \tag{C.110}$$

Similarly

$$E_1[Z_2 Z_2] = \frac{N}{2\sigma^2} A_s^2 + 1. \tag{C.111}$$

Then

$$E_1[2\mathcal{F}] = E_1[Z_1^2 + Z_2^2] = 2 + \frac{N}{2\sigma^2} (A_c^2 + A_s^2) = 2 + \lambda. \tag{C.112}$$

To obtain the variance of $2\mathcal{F}$, we start with calculating $E_1[Z_1^4]$ when the signal is present. It is written as

$$E_1[Z_1^4] = \frac{4}{N^2\sigma^4} \sum_{k=1}^N \sum_{l=1}^N \sum_{m=1}^N \sum_{n=1}^N E[x_k x_l x_m x_n] \cos(\omega_o t_k) \cos(\omega_o t_l) \cos(\omega_o t_m) \cos(\omega_o t_n) \tag{C.113}$$

To solve the Eq. (C.113), we make use of Isserlis theorem which states that

$$E[x_k x_l x_m x_n] = E[x_k x_l] E[x_m x_n] + E[x_k x_m] E[x_l x_n] + E[x_k x_n] E[x_l x_m] \tag{C.114}$$

Ignoring the oscillatory terms after implementing the summation, we get

$$E_1[Z_1^4] = \frac{1}{4} \frac{N^2 A_c^4}{\sigma^4} + 3 \frac{N A_c^2}{\sigma^2} + 3 \tag{C.115}$$

The next term is $E_1[Z_2^4]$ which is given by

$$E_1[Z_2^4] = \frac{4}{N^2\sigma^4} \sum_{k=1}^N \sum_{l=1}^N \sum_{m=1}^N \sum_{n=1}^N E[x_k x_l x_m x_n] \sin(\omega_o t_k) \sin(\omega_o t_l) \sin(\omega_o t_m) \sin(\omega_o t_n) \tag{C.116}$$

or,

$$E_1[Z_2^4] = \frac{1}{4} \frac{N^2 A_s^4}{\sigma^4} + 3 \frac{N A_s^2}{\sigma^2} + 3 \tag{C.117}$$

The expression for $E_1[Z_1^2 Z_2^2]$ is

$$E_1[Z_1^2 Z_2^2] = \frac{4}{N^2 \sigma^4} \sum_{k=1}^N \sum_{l=1}^N \sum_{m=1}^N \sum_{n=1}^N E[x_k x_l x_m x_n] \cos(\omega_0 t_k) \cos(\omega_0 t_l) \sin(\omega_0 t_m) \sin(\omega_0 t_n) \quad (\text{C.118})$$

or,

$$E_1[Z_1^2 Z_2^2] = \frac{1}{4} \frac{N^2 A_c^2 A_s^2}{\sigma^4} + \frac{1}{2} \frac{N (A_c^2 + A_s^2)}{\sigma^2} + 1 \quad (\text{C.119})$$

The variance of $2 \times \mathcal{F}$ – statistic is

$$\text{Var}_1[2\mathcal{F}] = E_1[Z_1^4] + E_1[Z_2^4] + 2E_1[Z_1^2 Z_2^2] - E_1^2[2\mathcal{F}] \quad (\text{C.120})$$

By substituting Eqs. (C.119, C.117, C.115, C.112) in Eq. (C.120), we get

$$\text{Var}_1[2\mathcal{F}] = 2(2 + 2\lambda) \quad (\text{C.121})$$

Hence, Eqs. (C.112 and C.121) show that $2 \times \mathcal{F}$ has the the expected form of the mean and variance of a non-central χ^2 distribution in the presence of a signal (Appendix B). This completes the proof that when the signal is present $2 \times \mathcal{F}$ has noncentral χ^2 distribution with two degrees of freedom.

Appendix D

Power emitted and spin-down limits

The total power per unit area radiated away in BD theory is given by [63], [64]

$$\frac{dP}{dA} = \frac{c^3}{16\pi f(\zeta)} \langle \dot{h}_+^2(t) + \dot{h}_\times^2(t) + \left(\frac{1-\zeta}{\zeta}\right) \dot{h}_s^2(t) \rangle \quad (\text{D.1})$$

where $f(\zeta) \equiv (1-\zeta)G$ is the coupling constant of this theory, and $h_+(t)$, $h_\times(t)$ and $h_s(t)$ denote the plus, cross, and scalar polarizations. $\langle . \rangle$ represents the time average and the parameter ζ is defined by Eq. (2.100). dA is the area element in spherical coordinates given by $dA = r^2 \sin \iota d\iota d\rho$. The total power can be divided into two parts as

$$\frac{dP}{dA} = \frac{dP^{(T)}}{dA} + \frac{dP^{(S)}}{dA} \quad (\text{D.2})$$

where $\frac{dP^{(T)}}{dA}$ is the power emitted in the tensor polarizations

$$\frac{dP^{(T)}}{dA} \equiv \frac{c^3}{16\pi(1-\zeta)G} \langle \dot{h}_+^2(t) + \dot{h}_\times^2(t) \rangle \quad (\text{D.3})$$

and $\frac{dP^{(S)}}{dA}$ is the power radiated away in the scalar polarization.

$$\frac{dP^{(S)}}{dA} \equiv \frac{c^3}{16\pi\zeta G} \langle \dot{h}_s^2(t) \rangle \quad (\text{D.4})$$

To compute the spin-down limit of the dipole radiation, first we need to find the power emitted in the scalar radiation for a spinning NS with a mountain on its equator. We can ignore the contributions from mass monopole and quadrupole moments and approximate the scalar polarization given by Eq. (3.22) as

$$h_s(t) \approx -h_0^d \sin \iota \sin \phi_s(t) \quad (\text{D.5})$$

where $\phi_s(t) = \omega t$ and ω is the spinning frequency of the star. h_0^d is the amplitude of dipole radiation given by Eq. (3.23)

$$h_0^d \equiv \frac{4\pi G}{c^3} \zeta D \frac{f_0}{r}, \quad (\text{D.6})$$

D is the dipole moment of the star in the comoving frame and $\omega = 2\pi f_0$. By plugging the first time derivative of Eq. (D.5) into Eq. (D.4), we obtain

$$P^{(S)} = \frac{c^3}{16\pi G \zeta} \omega^2 r^2 \left(h_0^d\right)^2 \langle \cos^2(\omega t) \rangle \int_{\iota=0}^{\pi} \int_{\rho=0}^{2\pi} \sin^3 \iota d\iota d\rho \quad (\text{D.7})$$

and using the fact that $\langle \cos^2(\omega t) \rangle \approx 1/2$, we obtain

$$P^{(S)} = \frac{c^3}{12G\zeta} \omega^2 r^2 (h_0^d)^2 \quad (\text{D.8})$$

The rotational kinetic energy of the star is given by

$$E = \frac{1}{2} I \omega^2 \quad (\text{D.9})$$

and the rate of loss of the kinetic energy is

$$\frac{dE}{dt} = I \omega \dot{\omega} \quad (\text{D.10})$$

I is the moment of inertia of the star.

By comparing Eqs. (D.8) and (D.10), we get

$$h_{0sd}^d = \frac{1}{r} \sqrt{\zeta \frac{12G}{c^3} I \frac{|\dot{f}_0|}{f_0}} \quad (\text{D.11})$$

To calculate the spin-down limit due to the quadrupole radiation in GR, we can obtain the power in the tensor polarizations in the BD theory and take the limiting case of $\zeta \rightarrow 0$

$$\frac{dP^{(T)}}{dA} \equiv \frac{c^3}{16\pi(1-\zeta)G} \langle \dot{h}_+^2(t) + \dot{h}_\times^2(t) \rangle \quad (\text{D.12})$$

where $h_+(t)$ and $h_\times(t)$ are described by Eqs. (3.17, 3.18)

$$h_+(t) = h_0 \frac{1 + \cos^2 \iota}{2} \cos 2\phi_s(t) \quad (\text{D.13})$$

$$h_\times(t) = h_0 \cos \iota \sin 2\phi_s(t) \quad (\text{D.14})$$

and h_0 is the constant amplitude given by Eq. (3.19)

$$h_0 = \frac{16\pi^2 G}{c^4} (1-\zeta) Q \frac{f_0^2}{r} \quad (\text{D.15})$$

By substituting the derivatives of Eqs. (D.13) and (D.14) in Eq. (D.12), we get

$$P^{(T)} = \frac{c^3}{32\pi G} h_0^2 \omega^2 r^2 \int_{\rho=0}^{2\pi} d\rho \int_{\iota=0}^{\pi} \left[\sin \iota + \sin \iota \cos^4 \iota + 6 \sin \iota \cos^2 \iota \right] d\iota \quad (\text{D.16})$$

or,

$$P^{(T)} = \frac{2}{5} \frac{c^3}{G} h_0^2 r^2 \omega^2 \quad (\text{D.17})$$

In Eq. (D.16), we have already taken into account $\langle \cos^2(2\omega t) \rangle \approx \langle \sin^2(2\omega t) \rangle \approx 1/2$. By equating Eq. (D.17) and (D.10), we get

$$h_{0sd}^q = \frac{1}{r} \sqrt{\frac{5G}{2c^3} I \frac{|\dot{f}_0|}{f_0}} \quad (\text{D.18})$$

The Eq. (D.18) gives the spin-down limit for the quadrupole radiation in tensor polarizations. Since, there is no ζ dependence, this is indeed the expression for the spin-down limit in GR and we can write it as

$$h_0^{sd} = \frac{1}{r} \sqrt{\frac{5G}{2c^3} I \frac{|\dot{f}_0|}{f_0}} \quad (\text{D.19})$$

Bibliography

- [1] A. Einstein. “Die Grundlage der allgemeinen Relativitätstheorie”. In: *Annalen der Physik* 354.7 (Jan. 1916), pp. 769–822. DOI: [10.1002/andp.19163540702](https://doi.org/10.1002/andp.19163540702).
- [2] Andrzej Trautman. “Radiation and Boundary Conditions in the Theory of Gravitation”. In: *Bull. Acad. Pol. Sci. Ser. Sci. Math. Astron. Phys.* 6.6 (1958), pp. 407–412. arXiv: [1604.03145](https://arxiv.org/abs/1604.03145) [gr-qc].
- [3] Ivor Robinson and A. Trautman. “Spherical Gravitational Waves”. In: *Phys. Rev. Lett.* 4 (8 Apr. 1960), pp. 431–432. DOI: [10.1103/PhysRevLett.4.431](https://doi.org/10.1103/PhysRevLett.4.431). URL: <https://link.aps.org/doi/10.1103/PhysRevLett.4.431>.
- [4] Maximiliano Isi, Matthew Pitkin, and Alan J. Weinstein. “Probing dynamical gravity with the polarization of continuous gravitational waves”. In: *Phys. Rev. D* 96 (4 Aug. 2017), p. 042001. DOI: [10.1103/PhysRevD.96.042001](https://doi.org/10.1103/PhysRevD.96.042001). URL: <https://link.aps.org/doi/10.1103/PhysRevD.96.042001>.
- [5] C. Brans and R. H. Dicke. “Mach’s Principle and a Relativistic Theory of Gravitation”. In: *Phys. Rev.* 124 (3 Nov. 1961), pp. 925–935. DOI: [10.1103/PhysRev.124.925](https://doi.org/10.1103/PhysRev.124.925). URL: <https://link.aps.org/doi/10.1103/PhysRev.124.925>.
- [6] B. P. Abbott et al. “Observation of Gravitational Waves from a Binary Black Hole Merger”. In: *Phys. Rev. Lett.* 116 (6 Feb. 2016), p. 061102. DOI: [10.1103/PhysRevLett.116.061102](https://doi.org/10.1103/PhysRevLett.116.061102). URL: <https://link.aps.org/doi/10.1103/PhysRevLett.116.061102>.
- [7] Christian D Ott. “The gravitational-wave signature of core-collapse supernovae”. In: *Classical and Quantum Gravity* 26.6 (Feb. 2009), p. 063001. DOI: [10.1088/0264-9381/26/6/063001](https://doi.org/10.1088/0264-9381/26/6/063001). URL: <https://doi.org/10.1088/0264-9381/26/6/063001>.
- [8] M. Maggiore. “Gravitational wave experiments and early universe cosmology”. In: 331.6 (July 2000), pp. 283–367. DOI: [10.1016/S0370-1573\(99\)00102-7](https://doi.org/10.1016/S0370-1573(99)00102-7). arXiv: [gr-qc/9909001](https://arxiv.org/abs/gr-qc/9909001) [gr-qc].
- [9] Peter G. Bergmann. “Summary of the Chapel Hill Conference”. In: *Rev. Mod. Phys.* 29 (3 July 1957), pp. 352–354. DOI: [10.1103/RevModPhys.29.352](https://doi.org/10.1103/RevModPhys.29.352). URL: <https://link.aps.org/doi/10.1103/RevModPhys.29.352>.
- [10] M. E. Gertsenshtein and V. I. Pustovoit. “On the Detection of Low-Frequency Gravitational Waves”. In: *Soviet Journal of Experimental and Theoretical Physics* 16 (Jan. 1963), p. 433. URL: http://jetp.ras.ru/cgi-bin/dn/e_016_02_0433.pdf.
- [11] G. E. Moss, L. R. Miller, and R. L. Forward. “Photon-Noise-Limited Laser Transducer for Gravitational Antenna”. In: *Appl. Opt.* 10.11 (Nov. 1971), pp. 2495–2498. DOI: [10.1364/AO.10.002495](https://doi.org/10.1364/AO.10.002495). URL: <http://opg.optica.org/ao/abstract.cfm?URI=ao-10-11-2495>.
- [12] R. Weiss. “Quarterly Progress Report 1972”. In: *MIT 105* (1972), pp. 54–76. URL: http://www.hep.vanderbilt.edu/BTeV/test-DocDB/0009/000949/001/Weiss_1972.pdf.

- [13] Piotr Jaranowski and Andrzej Krolak. “Optimal solution to the inverse problem for the gravitational wave signal of a coalescing compact binary”. In: *Phys. Rev. D* 49 (4 Feb. 1994), pp. 1723–1739. DOI: [10.1103/PhysRevD.49.1723](https://doi.org/10.1103/PhysRevD.49.1723). URL: <https://link.aps.org/doi/10.1103/PhysRevD.49.1723>.
- [14] Piotr Jaranowski et al. “On the estimation of parameters of the gravitational-wave signal from a coalescing binary by a network of detectors”. In: *Classical and Quantum Gravity* 13.6 (June 1996), pp. 1279–1307. DOI: [10.1088/0264-9381/13/6/004](https://doi.org/10.1088/0264-9381/13/6/004). URL: <https://doi.org/10.1088/0264-9381/13/6/004>.
- [15] *Einstein Telescope*. URL: <http://www.et-gw.eu/>.
- [16] *Cosmic explorer*. URL: <https://cosmicexplorer.org/>.
- [17] *LISA*. URL: <https://www.lisamission.org>.
- [18] *Pulsar Timing*. URL: <http://www.ipta4gw.org>.
- [19] P. Jordan. “Zum gegenwärtigen Stand der Diracschen kosmologischen Hypothesen”. In: *Zeitschrift für Physik* 157.1 (Feb. 1959), pp. 112–121. DOI: [10.1007/BF01375155](https://doi.org/10.1007/BF01375155).
- [20] Markus Fierz. “Über die physikalische Deutung der erweiterten Gravitationstheorie P. Jordans”. In: *Helv. Phys. Acta* 29 (1956), p. 128.
- [21] Orfeu Bertolami and PJ Martins. “Nonminimal coupling and quintessence”. In: *Physical Review D* 61.6 (2000), p. 064007. DOI: <https://doi.org/10.1103/PhysRevD.61.064007>.
- [22] Clifford M Will. “The confrontation between general relativity and experiment”. In: *Living reviews in relativity* 17.1 (2014), pp. 1–117. DOI: <https://doi.org/10.12942/lrr-2014-4>.
- [23] Eric Poisson and Clifford M Will. *Gravity: Newtonian, post-newtonian, relativistic*. Cambridge University Press, 2014. URL: <https://www.cambridge.org/pl/academic/subjects/physics/astrophysics/gravity-newtonian-post-newtonian-relativistic?format=HB&isbn=9781107032866>.
- [24] Charles W Misner, Kip S Thorne, and John Archibald Wheeler. *Gravitation*. Macmillan, 1973. URL: <https://press.princeton.edu/books/hardcover/9780691177793/gravitation>.
- [25] DE Lebach et al. “Measurement of the solar gravitational deflection of radio waves using very-long-baseline interferometry”. In: *Physical Review Letters* 75.8 (1995), p. 1439. DOI: <https://doi.org/10.1103/PhysRevLett.92.121101>.
- [26] E Fomalont et al. “Progress in measurements of the gravitational bending of radio waves using the VLBA”. In: *The Astrophysical Journal* 699.2 (2009), p. 1395. DOI: [10.1088/0004-637x/699/2/1395](https://doi.org/10.1088/0004-637x/699/2/1395).
- [27] Steven S Shapiro et al. “Measurement of the solar gravitational deflection of radio waves using geodetic very-long-baseline interferometry data, 1979–1999”. In: *Physical Review Letters* 92.12 (2004), p. 121101. DOI: <https://doi.org/10.1103/PhysRevLett.92.121101>.
- [28] SB Lambert and C Le Poncin-Lafitte. “Determining the relativistic parameter γ using very long baseline interferometry”. In: *Astronomy & Astrophysics* 499.1 (2009), pp. 331–335. DOI: <https://doi.org/10.1051/0004-6361/200911714>.
- [29] SB Lambert and Chr Le Poncin-Lafitte. “Improved determination of γ by VLBI”. In: *Astronomy & Astrophysics* 529 (2011), A70. DOI: <https://doi.org/10.1051/0004-6361/201016370>.

- [30] Bruno Bertotti, Luciano Iess, and Paolo Tortora. "A test of general relativity using radio links with the Cassini spacecraft". In: *Nature* 425.6956 (2003), pp. 374–376. DOI: <https://doi.org/10.1038/nature01997>.
- [31] Alex S Konopliv et al. "Mars high resolution gravity fields from MRO, Mars seasonal gravity, and other dynamical parameters". In: *Icarus* 211.1 (2011), pp. 401–428. DOI: <https://doi.org/10.1016/j.icarus.2010.10.004>.
- [32] EV Pitjeva. "Relativistic effects and solar oblateness from radar observations of planets and spacecraft". In: *Astronomy Letters* 31.5 (2005), pp. 340–349. DOI: <https://doi.org/10.1134/1.1922533>.
- [33] Aditya Vijaykumar, Shasvath J Kapadia, and Parameswaran Ajith. "Constraints on the time variation of the gravitational constant using gravitational wave observations of binary neutron stars". In: *Physical Review Letters* 126.14 (2021), p. 141104. DOI: <https://doi.org/10.1103/PhysRevLett.126.141104>.
- [34] Alejandro H Córscico et al. "An independent constraint on the secular rate of variation of the gravitational constant from pulsating white dwarfs". In: *Journal of Cosmology and Astroparticle Physics* 2013.06 (2013), p. 032. DOI: <https://doi.org/10.1088/1475-7516/2013/06/032>.
- [35] Kenneth Nordtvedt Jr. "Equivalence principle for massive bodies. I. Phenomenology". In: *Physical Review* 169.5 (1968), p. 1014. DOI: <https://doi.org/10.1103/PhysRev.169.1014>.
- [36] Kip S Thorne and John J Dykla. "Black Holes in the Dicke-Brans Theory of Gravity". In: *The Astrophysical Journal* 166 (1971), p. L35. URL: https://ui.adsabs.harvard.edu/link_gateway/1971ApJ...166L..35T/doi:10.1086/180734.
- [37] Paulo CC Freire et al. "The relativistic pulsar–white dwarf binary PSR J1738+0333–II. The most stringent test of scalar–tensor gravity". In: *Monthly Notices of the Royal Astronomical Society* 423.4 (2012), pp. 3328–3343. DOI: <https://doi.org/10.1111/j.1365-2966.2012.21253.x>.
- [38] ND Ramesh Bhat, Matthew Bailes, and Joris PW Verbiest. "Gravitational-radiation losses from the pulsar–white-dwarf binary PSR J1141–6545". In: *Physical Review D* 77.12 (2008), p. 124017. DOI: <https://doi.org/10.48550/arXiv.0804.0956>.
- [39] Benjamin P Abbott et al. "Tests of general relativity with GW170817". In: *Physical review letters* 123.1 (2019), p. 011102. DOI: <https://doi.org/10.1103/PhysRevLett.123.011102>.
- [40] Keith Riles. "Recent searches for continuous gravitational waves". In: *Modern Physics Letters A* 32.39 (2017), p. 1730035. DOI: <https://doi.org/10.1142/S021773231730035X>.
- [41] Junaid Aasi et al. "Advanced ligo". In: *Classical and quantum gravity* 32.7 (2015), p. 074001. DOI: [10.1088/0264-9381/32/7/074001](https://doi.org/10.1088/0264-9381/32/7/074001).
- [42] Fet al Acernese et al. "Advanced Virgo: a second-generation interferometric gravitational wave detector". In: *Classical and Quantum Gravity* 32.2 (2014), p. 024001. DOI: [10.1088/0264-9381/32/2/024001](https://doi.org/10.1088/0264-9381/32/2/024001). URL: <https://doi.org/10.1088/0264-9381/32/2/024001>.
- [43] T Akutsu et al. "Overview of KAGRA: Detector design and construction history". In: *Progress of Theoretical and Experimental Physics* 2021.5 (2021), 05A101. DOI: <https://doi.org/10.1093/ptep/ptaa125>.

- [44] Benjamin P Abbott et al. “First search for nontensorial gravitational waves from known pulsars”. In: *Physical review letters* 120.3 (2018), p. 031104. DOI: <https://doi.org/10.1103/physrevlett.120.031104>.
- [45] P. A. M. Dirac. “A New Basis for Cosmology”. In: *Proceedings of the Royal Society of London Series A* 165.921 (Apr. 1938), pp. 199–208. DOI: [10.1098/rspa.1938.0053](https://doi.org/10.1098/rspa.1938.0053).
- [46] Piotr Jaranowski and Andrzej Królak. *Analysis of gravitational-wave data*. Vol. 29. Cambridge University Press, 2009. DOI: <https://doi.org/10.1017/CB09780511605482>.
- [47] Piotr Jaranowski, Andrzej Krolak, and Bernard F Schutz. “Data analysis of gravitational-wave signals from spinning neutron stars: The signal and its detection”. In: *Physical Review D* 58.6 (1998), p. 063001. DOI: <https://doi.org/10.1103/PhysRevD.58.063001>.
- [48] R Abbott et al. “Gravitational-wave constraints on the equatorial ellipticity of millisecond pulsars”. In: *The Astrophysical Journal Letters* 902.1 (2020), p. L21. DOI: [10.3847/2041-8213/abb655](https://doi.org/10.3847/2041-8213/abb655). URL: <https://doi.org/10.3847/2041-8213/abb655>.
- [49] Benjamin P Abbott et al. “Narrow-band search for gravitational waves from known pulsars using the second LIGO observing run”. In: *Physical Review D* 99.12 (2019), p. 122002. DOI: <https://doi.org/10.1103/PhysRevD.99.122002>.
- [50] Benjamin P Abbott et al. “First search for gravitational waves from known pulsars with Advanced LIGO”. In: *The Astrophysical Journal* 839.1 (2017), p. 12. DOI: <https://doi.org/10.1103/PhysRevD.99.122002>.
- [51] Matthew Pitkin et al. “A nested sampling code for targeted searches for continuous gravitational waves from pulsars”. In: *arXiv preprint arXiv:1705.08978* (2017). DOI: <https://doi.org/10.48550/arXiv.1705.08978>.
- [52] P Astone et al. “Coherent search of continuous gravitational wave signals: extension of the 5-vectors method to a network of detectors”. In: *Journal of Physics: Conference Series* 363 (June 2012), p. 012038. DOI: [10.1088/1742-6596/363/1/012038](https://doi.org/10.1088/1742-6596/363/1/012038). URL: <https://doi.org/10.1088/1742-6596/363/1/012038>.
- [53] Piotr Jaranowski and Andrzej Królak. “Searching for gravitational waves from known pulsars using the \mathcal{F} - and \mathcal{G} - statistics”. In: *Classical and Quantum Gravity* 27.19 (Sept. 2010), p. 194015. DOI: [10.1088/0264-9381/27/19/194015](https://doi.org/10.1088/0264-9381/27/19/194015). URL: <https://doi.org/10.1088/0264-9381/27/19/194015>.
- [54] Paritosh Verma. “Probing Gravitational Waves from Pulsars in Brans-Dicke Theory”. In: *Universe* 7.7 (2021). ISSN: 2218-1997. DOI: [10.3390/universe7070235](https://doi.org/10.3390/universe7070235). URL: <https://www.mdpi.com/2218-1997/7/7/235>.
- [55] The LIGO Scientific Collaboration et al. *Searches for Gravitational Waves from Known Pulsars at Two Harmonics in the Second and Third LIGO-Virgo Observing Runs*. 2021. DOI: [10.48550/ARXIV.2111.13106](https://doi.org/10.48550/ARXIV.2111.13106). URL: <https://arxiv.org/abs/2111.13106>.
- [56] D. I. Jones. “Gravitational wave emission from rotating superfluid neutron stars”. In: *Monthly Notices of the Royal Astronomical Society* 402.4 (Mar. 2010), pp. 2503–2519. ISSN: 0035-8711. DOI: [10.1111/j.1365-2966.2009.16059.x](https://doi.org/10.1111/j.1365-2966.2009.16059.x). eprint: <https://academic.oup.com/mnras/article-pdf/402/4/2503/4899081/mnras0402-2503.pdf>. URL: <https://doi.org/10.1111/j.1365-2966.2009.16059.x>.

- [57] M. Pitkin et al. “First results and future prospects for dual-harmonic searches for gravitational waves from spinning neutron stars”. In: *Monthly Notices of the Royal Astronomical Society* 453.4 (Sept. 2015), pp. 4399–4420. ISSN: 0035-8711. DOI: [10.1093/mnras/stv1931](https://doi.org/10.1093/mnras/stv1931). eprint: <https://academic.oup.com/mnras/article-pdf/453/4/4399/8035169/stv1931.pdf>. URL: <https://doi.org/10.1093/mnras/stv1931>.
- [58] J Aasi et al. “Gravitational waves from known pulsars: results from the initial detector era”. In: *The Astrophysical Journal* 785.2 (2014), p. 119. DOI: [10.1088/0004-637x/785/2/119](https://doi.org/10.1088/0004-637x/785/2/119). URL: <https://doi.org/10.1088/0004-637x/785/2/119>.
- [59] Benjamin J. Owen. “Maximum Elastic Deformations of Compact Stars with Exotic Equations of State”. In: *Phys. Rev. Lett.* 95 (21 Nov. 2005), p. 211101. DOI: [10.1103/PhysRevLett.95.211101](https://doi.org/10.1103/PhysRevLett.95.211101). URL: <https://link.aps.org/doi/10.1103/PhysRevLett.95.211101>.
- [60] Fabian Gittins and Nils Andersson. “Modelling neutron star mountains in relativity”. In: *Monthly Notices of the Royal Astronomical Society* 507.1 (July 2021), pp. 116–128. ISSN: 0035-8711. DOI: [10.1093/mnras/stab2048](https://doi.org/10.1093/mnras/stab2048). eprint: <https://academic.oup.com/mnras/article-pdf/507/1/116/39770291/stab2048.pdf>. URL: <https://doi.org/10.1093/mnras/stab2048>.
- [61] J. Neyman and E. S. Pearson. “On the Problem of the Most Efficient Tests of Statistical Hypotheses”. In: *Philosophical Transactions of the Royal Society of London. Series A, Containing Papers of a Mathematical or Physical Character* 231 (1933), pp. 289–337. ISSN: 02643952. URL: <http://www.jstor.org/stable/91247> (visited on 06/13/2022).
- [62] Harald Cramér. *Mathematical methods of statistics*. Vol. 43. Princeton university press, 1999. URL: <https://www.springer.com/journal/12004>.
- [63] C. M. Will. “Gravitational radiation from binary systems in alternative metric theories of gravity: dipole radiation and the binary pulsar.” In: 214 (June 1977), pp. 826–839. DOI: [10.1086/155313](https://doi.org/10.1086/155313).
- [64] Paritosh Verma. “A Swinging Rod in Brans-Dicke Theory”. In: *Annalen der Physik* n/a.n/a (), p. 2100600. DOI: <https://doi.org/10.1002/andp.202100600>.